STUDIES IN NANOMAGNETISM: CO/NI MULTILAYERS IN MAGNETIC TUNNEL JUNCTIONS, NANOMAGNETS IN SUPERCONDUCTING MICROWAVE CAVITIES, AND MAGNETIC MULTILAYER NANOWIRES

A Thesis

Presented to the Faculty of the Graduate School

of Cornell University

in Partial Fulfillment of the Requirements for the Degree of

Master of Science

by

Theodore John Gudmundsen

January 2014

TABLE OF CONTENTS

ABSTRACT

Three experiments in nanomagnetism were performed. In the first, we reduced the switching current of a magnetic tunnel junction by incorporating Co/Ni films possessing perpendicular magnetic anisotropy (PMA). We characterized Co/Ni films with vibrating sample magnetometry and ferromagnetic resonance and measured a PMA of 0.22-0.26 mJ/m^2. By combining Co/Ni films with FeCoB in the electrodes, we reduced the demagnetization field of the free layer from 13000 Oe to 2000 Oe, while maintaining a low damping of only .015. These [Co/Ni]/FeCoB devices had 106% TMR at maximum, and 38% in a device with resistance below 10 Ω-um^2 that was spin-torque switchable. We demonstrated spin-torque switching in magnetic tunnel junctions of this kind, and saw some reduction of the switching current compared to similar devices in the literature. In the second project, I endeavored to design a niobium superconducting microwave cavity that I could strongly couple to a nanomagnet for a variety of scientific and technological applications. Towards that end, I successfully designed, fabricated, and packaged a 50 ohm superconducting cavity in the coplanar waveguide geometry with an unprecedently thin center line of 476 nm. Under cryogenic conditions, the cavity showed a quality factor of 566 at 5.9 GHz. In the third project, I designed an electrically-switchable three-terminal device for injecting spin currents into semiconductors. The device consists of a multilayer magnetic nanowire with a domain wall that can be moved by spin-torque transfer. I designed a fabrication recipe to make that device, and made significant progress towards fabricating a complete device, including the demonstration of the lithography for all four layers.

ACKNOWLEDGEMENTS

The author gratefully acknowledges support from the NSF through the IGERT Graduate Traineeship in Nanoscale Control of Surfaces and Interfaces (DGE-0654193), and the Graduate Research Fellowship Program.

This work was partially supported by the Cornell Center for Nanoscale Systems, and the ONR and ARO through grants N00014-06-1-0428 and W911NF-08-2-0032. This work made use of the facilities of the Cornell Center for Materials Research (CCMR) with support from the National Science Foundation Materials Research Science and Engineering Centers (MRSEC) program (DMR 1120296). This work was performed in part at the Cornell NanoScale Facility, a member of the National Nanotechnology Infrastructure Network, which is supported by the National Science Foundation (Grant ECS-0335765).

Some of the work presented in this thesis owes partial authorship credit to Takahiro Moriyama, Pinshane Huang, Yongtao Cui, Aaron Swander, Greg Stiehl, and Dan Ralph. A debt of gratitude is also owed to Alex Mellnik, Colin Heikes, Lin Xue, Chen Wang, Wan Li, Eugenia Tam, Josh Parks, Sufei Shi, Kiran Thadani, Steve Kriske, and Jon Shu for their instruction and help in the lab. I received printed circuit boards and advice about resonators from members of the Schwab group, Matt Shaw, Tristan Rocheleau, and Tchefor Ndukum. Many thanks to Mohamed Zaghoo and Dorothy Sands for their help with this document. I am grateful to the staff of the CNF, especially Noah Clay, for their help with all nanofabrication procedures. I am indebted to my advisor, Dan Ralph, for his assistance in brainstorming research directions, securing funding, and steering this research. Thanks also to Bob Buhrman and Tomas Arias for advising me as members of my committee.

CHAPTER 1

INTRODUCTION

Nanomagnetism, the study of ferromagnets that have been manufactured to nanoscale dimensions, is a growing field with open questions in fundamental physics and great promise for novel technologies. In the 20th century, researchers probed a number of the characteristics of bulk magnetic materials. As thin film technology progressed, much of the physics research in magnetics turned to magnetic thin films and the devices that could be made from them. This trend was productive on both the fundamental and applied physics fronts. In 1986, researchers realized that two thin magnetic films separated by a thin metal layer had a lower resistance when the films were aligned than when they were anti-aligned[1][2]. This effect, giant magnetoresistance, was the subject of the 2007 Nobel Prize in physics. The fundamental mechanism behind giant magnetoresistance is that ferromagnets cause currents running through them to become spin-polarized, and that spin-polarization affects scattering in magnets. This idea has led to the discovery of many other useful physical phenomena. A notable example was Slonczewski's 1996 prediction that a spin-polarized current could be used to reverse the magnetization of a nanomagnet[3], which has blossomed into the field of spin-torque physics. Tunneling magnetoresistance[4], current-driven domain wall motion[5], non-local spin currents[6], spin-injection into semiconductors[7][8], and the giant spin Hall effect[9] have also grown out of the study of spin-polarized currents in nanomagnets.

These new ideas have already found tremendous applications in digital memory in the last ten years, and numerous other applications have been proposed. Giant magnetoresistance has revolutionized the hard drive industry, enabling magnetic read-heads that are smaller and more sensitive, which has in turn led to an

increase in data storage densities. Magnetic random access memory (MRAM), which uses spin-torque to write the bits of a memory, is also now commercially available. Spintronic transistors[10], race track memory[11], and three-terminal magnetic memory[9][12] are all promising technological ideas based on nanomagnetics that are still being researched. Nanomagnets lend themselves naturally to information storage because they are non-volatile: they don't need power to retain their state. For this reason, they will likely continue to find applications in computing for years to come.

In the following three chapters, I will discuss three research projects in nanomagnetics. In chapter 2, we will use Co/Ni superlattices, a material that exhibits perpendicular magnetic anisotropy, to try to improve the properties of an MRAM bit. We successfully incorporated Co/Ni films into such a bit and studied how that changed the bit's properties. In the next two projects, I'll describe efforts to couple nanomagnets to other kinds of experimental apparatus. In chapter 3, I will propose coupling nanomagnets to a superconducting microwave cavity in order to study tiny magnets with more sensitivity, and for various other microwave and quantum applications. I'll describe how we fabricated and characterized a superconducting cavity with the thinnest center line on record. In chapter 4, I'll discuss how we designed an electrically-switchable multilayer magnetic nanowire to inject spin-polarized currents into semiconductors. A switchable spin-injector of this form might find applications in spintronics, photonics, or fundamental science. I'll describe the fabrication process we developed and tested to make such a device.

Taken together, these three projects span a range of scientific motivations, from the fundamental scientific desire to improve the sensitivity with which we can probe materials (cavity FMR), to the early-stage engineering demonstration of a new kind of device (a switchable spin-injector), to the very applied idea of

using a new material to improve an existing technology (Co/Ni superlattices in MRAM bits). Although the approaches and applications are disparate, the three projects are unified by a desire to explore nanomagnets and their applications.

CHAPTER 2

CO/NI MULTILAYERS IN MAGNETIC TUNNEL JUNCTIONS

2.1 Introduction and Motivation

Magnetic Random Access Memory (MRAM) is an emerging technology that offers to combine the advantages of both hard drives and dynamic random access memory (DRAM). Hard drives, which store information in magnets, are useful because they use little power when idle. But the seek time on a hard drive is on the order of milliseconds, many orders of magnitude too slow for random access memory. In contrast, DRAM, where each bit is the charge on a capacitor, is fast and cheap, but it leaks power quickly and has to be refreshed constantly. A kind of memory that stored information in magnets, like a hard drive, but read and wrote bits quickly, like DRAM, would be of significant technological interest.

The barrier to such a device is the method of writing in today's hard drives. Today's hard drives seek slowly because they have moving parts—the disk spins underneath a read/write head in order to access a given bit. This geometry is necessary because the magnets on the disk's surface are switched by the magnetic field from a coil of wire, as shown in figure 2.1. This coil of wire is very large relative to the bits, and thus has to be spun into position above the bit before writing can occur.

Spin transfer torque[3], the concept of using the angular momentum from a spin-polarized current to move a magnet, can be used to write magnetic bits without the bulky coil of wire[13]. As shown in figure 2.2, a pulse of current becomes spin-polarized in the fixed layer, and then the angular momentum of those spins is transferred to the free layer, causing the free layer to change orientations. The diagram shows antiparallel-to-parallel switching (AP→P), but if a current is passed

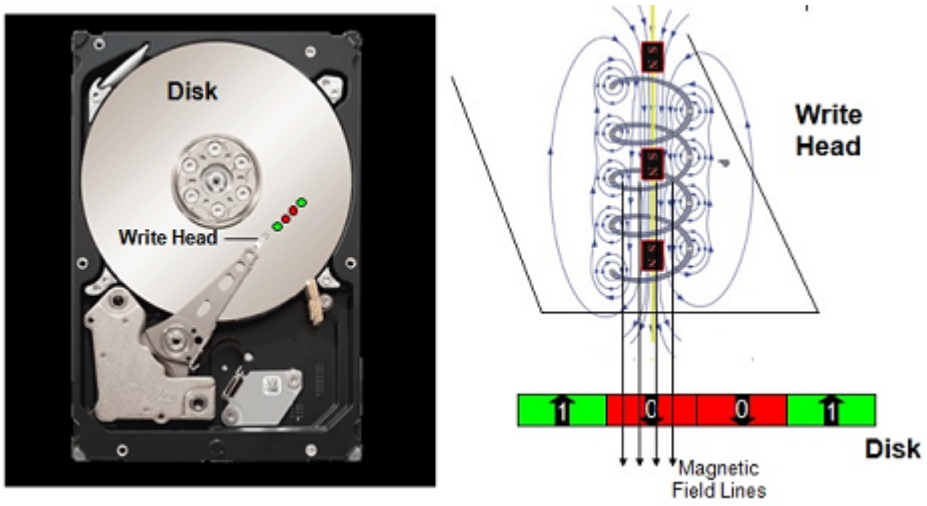

Figure 2.1: A top and cross-sectional view of a modern hard drive. When current passes through a coil of wire in the write head, the resulting field can switch the magnets on the disk.

in the opposite direction, it happens that the electrons reflecting off the MgO are spin-polarized in the opposite direction. When these reflected electrons return to the free layer, they can switch the free layer from the right to the left. This is called parallel-to-antiparallel (P→AP) switching.

Of course, this picture of spin-transfer torque contains a number of simplifications. For example, we assume that the magnets involved have only a single domain. For the magnet sizes in this study and in industrial applications, this is a good approximation, although we will consider the limits of that approximation below. We have assumed a semi-classical picture of switching; one gets both a more satisfying explanation of the physics and more quantitative predictions of how much spin current is transmitted, reflected, and absorbed from a basic quantum mechanical model[14], although the conclusions are largely the same. Another approximation is that the spins only apply a torque that attempts to align the magnet with the spins. Recent work[15] has shown that there is a significant spin torque component normal to both the direction of the spins in the spin current and the magnetic moment of the free layer. This surprising result is not completely

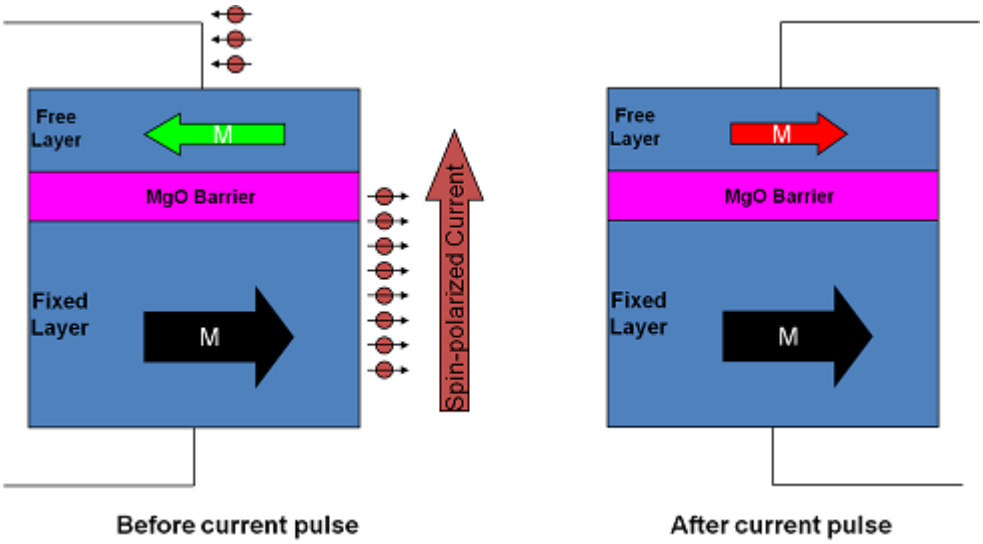

Figure 2.2: A schematic of a single MRAM bit. The direction of the free layer is the state of the bit. A pulse of electrons up through the stack causes the free layer to move from left-pointing to right-pointing.

understood, but as the perpendicular component of the spin torque is generally smaller than the in-plane component, we can afford to ignore it for the remainder of this discussion.

Even with these simplifications, the dynamics of the magnetization as it switches under the influence of the spin-transfer torque are non-trivial and important. These dynamics are caused by the demagnetizing fields, the closing field lines of the magnetization. We can write the demag fields as $\mathbf{H_{eff}} = [-N_x M_x, -N_y M_y, -N_z M_z]$, where $\mathbf{N}$ represents the demagnetization coefficients, which depend only on the shape of the magnet[16]. Because of the demag fields, a thin-film magnet pointing out of plane of the film is in a much higher energy state than when it points in the plane of the film. Similarly, the easy axis of an elliptical thin film magnet is in the direction of the major axis of the ellipse. I will denote the energy barrier between the easy axis and the hard in-plane axis as E_u, and the energy barrier between the easy axis and the hard out-of-plane axis as $E_\perp$, as shown in figure 2.3a.

These demagnetizing fields have a non-intuitive effect on the motion of the

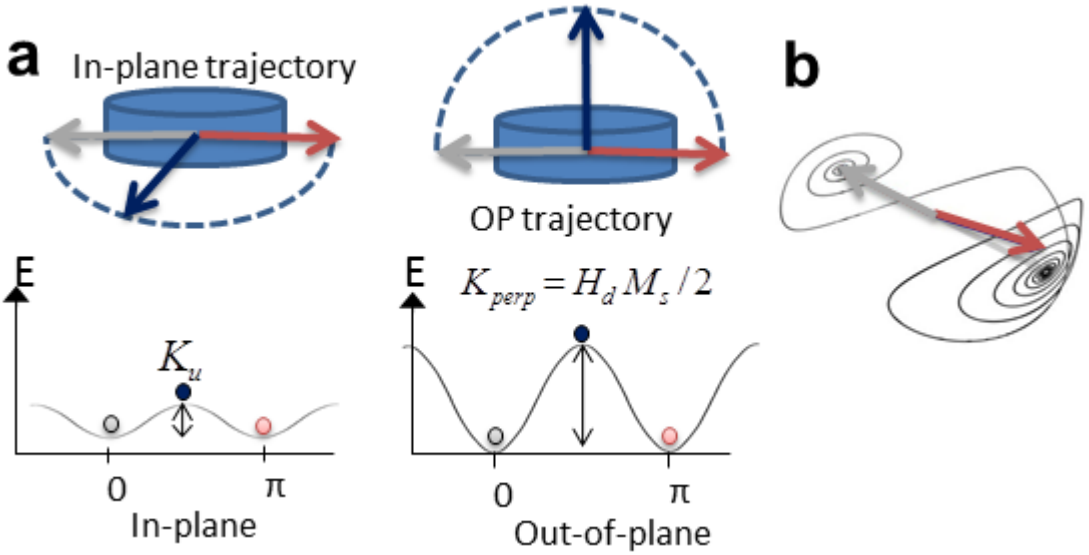

Figure 2.3: (a) A nanomagnet, here pictured as the blue ellipse, has an easy axis (horizontal) with two low-energy equilibrium states, shown as the red and gray arrows. The other two axes are harder, with the out of plane axis being much harder than the in-plane axis. The left diagram shows an energy profile of various in-plane states, the right diagram shows an energy profile of various out of plane states. Typical dimensions for such a nanomagnet in this field are 100 nm x 50 nm x 3 nm. (b) The dynamics of switching from one equilibrium state (the red arrow) towards the other equilibrium state (the gray arrow). Because of the anisotropic energy landscape, a magnet under the influence of spin torque pushing it in the direction of the gray arrow will actually follow a path outlined by the black line, precessing around the effective demagnetization field.

magnetization. When the spin-polarized current is turned on, the motion of the magnetization as it switches from one axis to the other is given by the Landau-Lifshitz-Gilbert-Slonczewski equation:

$$\dot{\mathbf{M}} = -\gamma_0 \mathbf{M} \times \mathbf{H_{eff}} + \frac{\alpha}{M_s} \mathbf{M} \times \dot{\mathbf{M}} - \tau(V) \gamma_0 \mathbf{M} \times (\mathbf{M} \times \hat{\mathbf{P}}) \tag{2.1}$$

where H_{eff} is the combination of external fields and demagnetizing fields, γ_0 is the gyromagnetic ratio, α is a unitless phenomenological damping term, $\tau(V)$ is the dimensionless spin torque strength as a function of the voltage across the stack, and $\mathbf{P}$ is the direction of the polarizer/fixed layer. Simulating this equation with reasonable parameters gives a path like that shown in figure 2.3b. We see that when the magnetization begins to rotate away from the easy axis under the influence of the spin torque, the magnetization will actually precess around the easy axis, passing through all three dimensions. (For intuition on why this occurs, one can simply imagine that a large magnetic field points along the easy axis in the direction of $\mathbf{M}$, which is not a bad approximation of the energy situation if both hard axes are much higher in energy than the easy axis. Then the magnetization, once moved away from equilibrium, will precess around that field.)

This switching path is important because one of the major impediments to commercial implementation of MRAM is the large amount of current needed to switch the free layer[17]. Switching will only occur when the current pulse exceeds some critical value given in this case by

$$I_c = \frac{2e}{\hbar} \frac{\alpha}{\eta} (E_u + E_\perp) \tag{2.2}$$

where η is a unitless measure of the spin torque efficiency. This expression comes from balancing the angular momentum lost due to damping with the spin torque at small angles, which is a reasonable approximation because the highest current is needed at the beginning of the precession process[18]. (For a more detailed

discussion of the origin of this equation, see appendix A.) As expected, we see that both E_u and $E_\perp$ contribute to increasing I_c. This makes sense in the context of the 3-D path shown in figure 2.3b.

To decrease this critical current, it is desirable to reduce the energy barrier $E_\perp$. Some anisotropy in the magnetic energy landscape is desirable, because we need some energy barrier to maintain thermal stability. But during a thermal fluctuation, it is the lower energy barrier, E_u, that will be crossed. The higher energy barrier does nothing to promote thermal stability. So we wish to reduce $E_\perp$ until it is on par with E_u and roughly equal to $40k_BT$[19][20], an industrially accepted level of thermal stability for bits. Considering only shape anisotropy as we have so far, a 100 nm x 50 nm x 3 nm elliptic cylinder of permalloy ($Ni_{81}Fe_{19}$) would have $E_\perp = 79 \times 10^{-19}$ J, while the thermal stability barrier at room temperature is only 1.7×10^{-19} J. So there is considerable room for improvement.

When we talk about this energy "barrier", what we really mean is that the energy of the ferromagnet depends on the direction of the magnetization, and that the energy is higher in certain magnetization directions than in others. In other words, the magnetic energy landscape is anisotropic. Since this energy depends on magnetic field direction, much like the energy of a ferromagnet in an external field, it is more common in the literature to state these energy barriers in units of magnetic field,

$$H_d \equiv \frac{E_\perp}{\frac{1}{2}\mu_0 M_s V} \tag{2.3}$$

The factor of 1/2 is typical of self-energy terms, and is explained in more detail in [21]. We speak of wanting to decrease H_d, the demag field. This is slightly misleading, as the demag field is a geometric quantity, and whatever other tricks we play merely offset the demag field to reduce the total energy of magnetization in the perpendicular direction. But generally H_d is used as a measure of the energy

barrier. In the case of a thin film magnet like ours, $H_d \approx M_s \approx 9200$ Oe, since nearly all of the field lines close through the magnet when the magnetization points out of the plane of the magnet. The desired energy barrier for thermal stability, $40k_BT \approx 200$ Oe. The goal of this project is to reduce the switching current of an MRAM bit by reducing H_d.

Good work has already been done towards reducing H_d [22] [23] [24] [25] [26]. Some devices have had a positive H_d as discussed[23]; some have had a negative H_d[24] [25], resulting in magnets that point perpendicular to the plane of the film in equilibrium. Although equation 2.2 is slightly different for perpendicular magnetization, as long as $|H_d|$, is low, the switching current will be small regardless of the sign of H_d.

Low H_d alone is not sufficient to make a good MRAM bit. To keep the switching current low, the damping, α, must be small (as shown in equation 2.2). Even more importantly, to make sure that the bit can be read clearly, the bit's magnetoresistance must be large. Magnetoresistance is defined as

$$\mathrm{MR} = \frac{R_{AP} - R_P}{R_P} \tag{2.4}$$

where the parallel (P) and antiparallel (AP) states refer to a system like the one shown in figure 2.2. Dramatic increases in magnetoresistance have been driving corresponding order-of-magnitude improvements in the hard drive industry over the last several decades. Most recently, giant magnetoresistance (GMR)[2][1], which won its discoverers the 2007 Nobel Prize in Physics, yielded to tunneling magnetoresistance (TMR)[27][28]. GMR devices have a metal (often Cu or Cr) spacer between the magnetic layers, and can expect room temperature MRs on the order of 1% to 10%, whereas TMR devices are defined by an insulating barrier, often MgO, and often have room temperature MRs in the range of 100% to 600%[29]. As of the time of this project, several groups had made GMR devices with reduced

H_d, but none had been able to combine all of the elements: reduced H_d, small α, and high TMR. We hoped to put all of these elements together. As will be described below, the materials science of this endeavor is not trivial. If we were able to create a materials stack with reduced H_d, small α, and high TMR, we then planned to create a prototype MRAM bit at the nanometer scale that could be written with spin torque current, and read out with TMR. While reducing H_d is a good intermediate goal, the ultimate figure of merit in this field is the amount of current needed for writing. We sought to minimize I_c while maintaining high TMR.

In this chapter, I will describe how we achieved each of these goals in turn. First, we characterized Co/Ni multilayer films to reduce H_d. Then, we incorporated those multilayers into MgO devices and tested their TMR. Finally, we built a nanometer-scale prototype bit, and demonstrated current switching with a reduced critical current. I will discuss these results and their significance in the larger field of MRAM development in the sections below.

2.2 Different Kinds of Magnetic Anisotropy and Material Combinations

To try to reduce H_d, we consider other forms of magnetic anisotropy beyond shape anisotropy. To offset the shape anisotropy, we will use surface anisotropy. At a metal surface, there is a broken symmetry, which leads to non-symmetric, unbalanced electron orbitals. When these unbalanced orbitals are combined with spin-orbit coupling, it can lead to a significant magnetic anisotropy. Depending on the material and crystalline lattice, this anisotropy can lower the energy of the magnetic state pointing perpendicular to the plane of the magnet; for this reason,

we can also describe this kind of energy term as perpendicular magnetic anisotropy (PMA). This effect was first suggested by Néel as early as 1954[30], and was advanced by Gay and Richter's 1986 calculation of surface magnetic anisotropy[31] using self-consistent local-orbital theory. An excellent summary of the subject can be found in O'Handley's textbook[21]. In order for surface anisotropy to be a significant effect, the material in question needs to have the right electron structure, sufficient spin-orbit coupling, and very little thickness. Surface anisotropy has been demonstrated in a number of materials systems, but this effect is strong and well-studied in repeated thin films ("superlattices") of $(111)_{fcc}$-oriented Co/X, where X is Ni [32][33][34][35][36] [23], Pd [37], Pt [22][38], Au [39], or Ir [40].

Although several choices could have worked, we chose to use Co/Ni. Other than Co/Ni, Co/Pt is the most frequent other choice, but it shows evidence of having a high damping coefficient ($\alpha \approx 0.04+$ at Co=2Å)[41], which would increase the switching current (see equation 2.2). Co/Ni, however, seems to have a relatively low damping coefficient ($\alpha \approx$ 0.02-0.03 at Co=2Å)[42]. Specifically, we chose to use Co/Ni in a 1:2 atomic ratio. Daalderop [32] suggests that the presence of non-symmetric electron orbitals necessary for PMA is highly dependent on the number of valence electrons. Therefore, a cobalt-rich system will behave differently from a nickel-rich system. His calculations suggest that 1:2 Co:Ni ratio will have the largest PMA of all possible ratios.

Another possible system that has received extensive attention in the literature is $L1_0$ ordered alloys, which are binary systems crystallized in fcc, but with the two different species occupying adjacent (001) planes instead of intermixing randomly[43]. The most common two species for making $L1_0$ ordered alloys are cobalt and platinum[44], although other materials are possible[45] [46]. These materials have excellent magnetic properties, but since they're difficult to fabricate

and usually require high anneal temperatures[47] that would ultimately ruin other parts of the MRAM bit, we decided against them.

Another PMA option is an alloy of rare earth metals and magnetic transition metals. In such alloys, the interplay between the magnetic moments of the sublattices can cause perpendicular magnetic anisotropy[48]. Because of this mechanism, TbCoFe electrodes have been incorporated into magnetic tunnel junctions in the past[26]. However, doing so greatly increases α, by a factor of 3 or more[49], and therefore isn't a good path to reducing the critical current. After considering all of these options, we decided to try to use $(111)_{fcc}$-oriented Co/Ni multilayers.

2.3 Characterizing Co/Ni Multilayers I: Vibrating Sample Magnetometry

Having decided on materials to use, we sought to characterize the materials' properties in order to decide exactly what ratio of materials, growth conditions, substrates, etc. would give the desired magnetic properties. There are three kinds of anisotropy energy that will change the system's energy as the magnetization direction varies: shape anisotropy, surface anisotropy, and crystalline anisotropy. Given a stack of the form [Co t_{Co}/Ni t_{Ni}]x N, where t is the thickness of the layer and N is the number of layers, we can write down a general expression for the energy of the system as follows:

$$E = -\frac{\mu_0 V}{2}\mathbf{M}\cdot(-\mathbf{N}\mathbf{M}) - A(2N+1)\sum_n K_n^{SO}(\hat{\mathbf{M}}\cdot\hat{\mathbf{n}})^{2n} + V\sum_n K_{un}\sin^{2n}\theta \quad (2.5)$$

where $\hat{n}$ is the direction perpendicular to the plane of the film, A is the surface area of the sample, V is the volume, $V = AN(t_{Co} + t_{Ni})$, and θ is the angle between the magnetization and the c-axis of the Co/Ni crystal. The first term is the shape

anisotropy energy from the closing field lines. Note that **NM** is not a dot product, but instead implies $\mathbf{NM} = N_x M_x \hat{x} + N_y M_y \hat{y} + N_z M_z \hat{z}$.

The second term is a perfectly general power series expression for the surface anisotropy, which comes from the spin orbit energy discussed above. We don't know any of the coefficients K_n^{SO}. Note that I will define the term $E_S = \sum_n K_n^{SO}$, and in the ferromagnetic resonance section below, I will write this surface anisotropy energy as $-E_S A(2N+1)(\hat{\mathbf{M}} \cdot \hat{\mathbf{n}})^2$, neglecting the higher order nature of some of the energy terms. A more careful study would try to tease out the contribution of the higher order terms, but that is beyond the scope of this work. Note also that we are assuming that the outside surfaces of the Co/Ni stack contribute to the PMA in equal measure to the interior Co/Ni interfaces. We will discuss the limitations of this assumption in section 2.5.4 below.

The third term of equation 2.5 is the crystalline anisotropy energy. The magnetic materials used in our study—iron, cobalt, and nickel—all display uniaxial anisotropy, meaning that there is an energy term that depends on the angle between the magnetization and the c-axis of the crystal. This energy term is well characterized in the literature: K_{u1} and K_{u2} can be found in textbooks[21], and the $n \geq 3$ terms are generally negligible. For the particular material combinations we will consider in this study, FeCoB (60/20/20 atomic %) and Co/Ni multilayer stacks (generally 1:2 by volume), the maximum uniaxial anisotropy should be around 850 Oe for FeCoB and 2300 Oe for Co/Ni, which could be significant. (Note: these numbers are just linear combinations of published coefficients for the pure metals. Although adding coefficients linearly may not be very accurate, it's probably reasonable for an order of magnitude estimate.) But the samples are generally amorphous as deposited. After annealing, the samples become "textured," aligned along the vertical axis but polycrystalline with respect to the other axes,

which could add a crystaline component. However, Co/Ni thin films generally texture with the (111) axis aligned in the perpendicular direction, but the c-axis direction varying from grain to grain. This will generally preclude the uniaxial crystalline anisotropy from playing an important role, and we will neglect it going forward. Note that both the second and third terms of equation 2.5 can only have even powered terms in M because ferromagnetism is a second order phase transition, and one can only have even-powered terms of the order parameter in the free energy expression of a second order phase transition.

We can simplify equation 2.5 for the case when the magnetization is pointing perpendicular to the plane of the film. In that case,

$$E_{\perp} = \frac{\mu_0}{2} AN(t_{Co} + t_{Ni}) M_{tot}^2 - E_S A(2N + 1) \tag{2.6}$$

where M_{tot} is the saturation magnetization of the multilayer,

$$M_{tot} \equiv (M_{Co} t_{Co} + M_{Ni} t_{Ni})/(t_{Co} + t_{Ni})$$

Here M_{Co} and M_{Ni} are the saturation magnetizations of bulk cobalt and nickel from the literature[21]. The first term is the demagnetization energy, $\frac{1}{2}\mu_0 M_{tot} V H_{demag}$, and we have assumed that $H_{demag} \approx M_{tot}$, which is an approximation good to within a few percent for our devices. The second term in equation 2.6 is the surface anisotropy energy, controlled by the unknown coefficient, E_S, the anisotropy energy at each surface in units of [energy]/[length]^2. Note that when $E_{\perp}$ is positive, the equilibrium magnetization position is in the plane of the film, and when it is negative, the equilibrium magnetization is out of the plane of the film. We wanted to empirically determine a value for E_S.

Multiple papers have calculated values for E_S in the literature, and the most common method is vibrating sample magnetometry (VSM)[32] [33]. In a VSM, the sample is placed on a stage between two large electromagnets that can apply

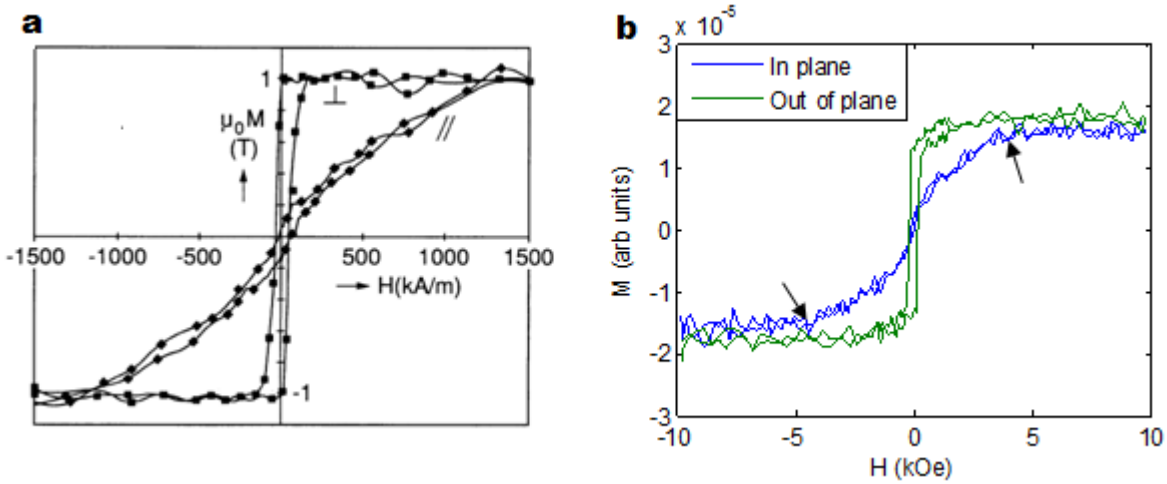

Figure 2.4: (a) A VSM measurement of [Co 2Å/Ni 4Å]x20 from the literature [32]. The horizontal axis is the applied field, and the vertical axis is the magnetization of the sample in the direction of the applied field, calculated from the response in the pick-up coils. The two curves represent two measurements of the same sample, one with the applied field parallel to plane of the film, and the other with the applied field perpendicular to the plane of the film. The saturation magnetization is clearly about 1T, and the hard axis saturation field is relatively well defined at about 1400 kA/m. (b) A VSM measurement of [Co 3Å/Ni 6Å]x8 on standard non-magnetic smoothing layers. A linear background has been subtracted. Two arrows indicate my estimation of the hard axis saturation point at around 4000 Oe, but the transition is not at all sharp, leaving a large uncertainty in this estimate.

a variable field. At the center of each magnet is a pick-up coil oriented along the same axis. The external magnetic field from the coils is varied, and the response from the sample is measured. The sample vibrates perpendicular to the axis of the pick up coils, in and out of their range, and the resulting signal is mixed through a lock-in amplifier to reduce noise. An average VSM curve looks like the one shown in figure 2.4a. The perpendicular magnetic anisotropy is calculated from the hard axis saturation field—the amount of field needed to fully saturate the magnet in its higher energy direction. This quantity is H_d, as we previously defined it, so that $E_\perp = (1/2)\mu_0 M_S H_d$. An example of a VSM curve for one of our samples is shown in figure 2.4b. One can see that the point of saturation isn't very clear, leaving a large uncertainty. This is an average curve—for many curves, H_d is even less clear or even indistinguishable from the linear background. Note that for this sample, the equilibrium magnetization direction is out of plane, so we record $H_d = -4000$ Oe.

From this data alone we could extract a value for E_S, but to improve the quality of our estimate, we measure many samples in the same way. In figure 2.5, we see H_d extracted from VSM measurements of several samples, including the one shown in figure 2.4b. The hard axis saturation values shown should obey the linear relationship

$$H_d = M_{tot} - \frac{2E_S}{\mu_0 M_{tot}} \frac{(2N+1)}{t} \tag{2.7}$$

where t is the total thickness of the stack. We have arrived at this relationship simply by combining equations 2.3 and 2.6 above. The y-intercept, 11200 Oe, is the saturation magnetization, which is close to the expected value of 10300 Oe. The slope gives $E_S = 0.26$ mJ/m^2, although the uncertainty is significant, around 25%. This is comparable to values in the literature. Daalderop [32] gives $E_S = 0.31$ mJ/m^2, and Bloemen [33] gives $E_S = 0.18 \pm 0.04$ mJ/m^2.

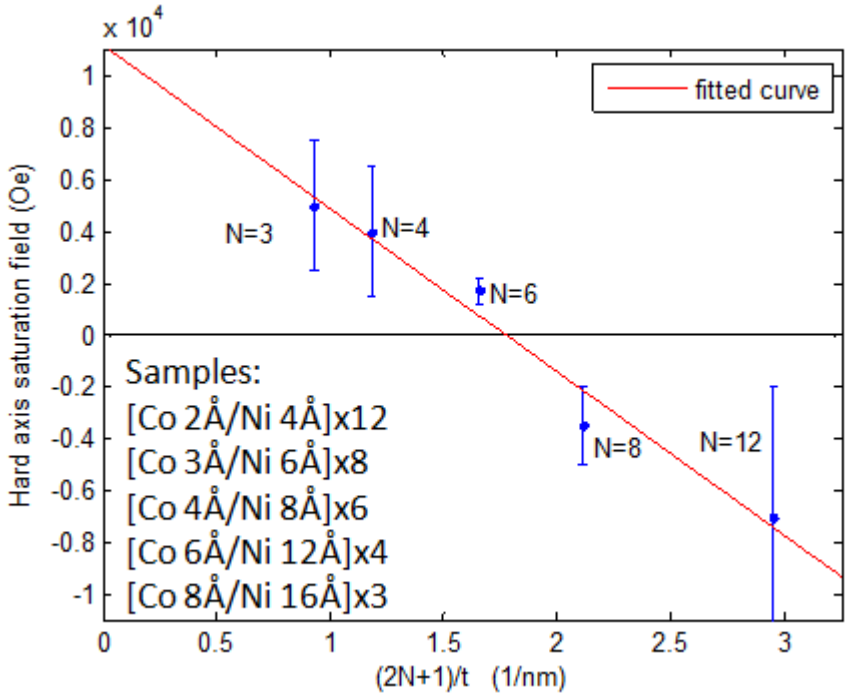

Figure 2.5: Hard axis saturation field, H_d for a series of Co/Ni multilayers with varying structures as shown. Each point is extracted from a VSM curve, and the error bars are my estimate at the uncertainty in where, exactly, the hard axis saturates. Note that the nominal thicknesses listed differ from the actual thicknesses by as much as 0.6 Å. This discrepancy is due to lag in the shutter opening and closing routine. The actual thicknesses were used in the calculation.

Besides the high uncertainty, there is another reason to be careful with this result. The samples measured here are actually significantly thicker than anything that could be used in an MRAM bit. In an MRAM bit, switching current scales with volume, so it is necessary to keep the number of layers low. However, in figure 2.5, all of the samples have a nominal magnetic thickness of 7.2 nm, at least 3 times larger than anything that would be commercially viable. It was necessary to measure slightly thicker films because, in the VSM, signal scales with volume, so it's difficult to distinguish H_d for very thin samples. (It should be possible to measure thinner samples with more careful work, but for the 40 VSM samples measured in this study, we couldn't find a clear hard axis saturation point in almost any of the thinner samples.) This extra thickness wouldn't matter if the film at the top of a 7.2 nm stack is the same as the film at the top of a 2 nm stack. But there are indications in the literature [33] that this may not be true: E_S should be very sensitive to the structure underneath it. Therefore, the E_S calculated from [Co 2Å/Ni 4Å]x12 may be different from the E_S of [Co 2Å/Ni 4Å]x2, since the top layers may have different properties from the bottom layers. One mechanism for this sensitivity could be the magnetoelastic energy term, which is non-negligible. If the strain in the Cobalt films changes by 1%, that corresponds to a change in H_d of 2200 Oe, using bulk values for the magnetoelastic coefficient B_1 and saturation magnetization from the literature [21]. Roughness is another mechanism by which differences in underlayers could cause variations in E_S. A sample with nominally 2 Å of Co deposited by magnetron sputtering can not possibly be uniform at the monolayer level—instead, it is a heterogeneous mix of islands of cobalt. We should expect that this heterogeneity would change the surface anisotropy energy significantly for very thin films, and that roughness could significantly affect the nature and size of these islands.

2.4 Characterizing Co/Ni Multilayers II: Ferromagnetic Resonance

In addition to VSM, we also characterized the magnetic properties of our films with ferromagnetic resonance (FMR), although with less success. The basic techniques of FMR are quite old[50], although recently the Ralph group gave FMR a new twist by using spin torque to drive magnetic motion, a technique called ST-FMR[51]. We used both conventional, "flip-chip" FMR and ST-FMR to study Co/Ni films, although only the flip-chip FMR will be described here. The ST-FMR work never led to any clear conclusions, and it was performed almost exclusively by my colleague, so I will not present it in this document. In this section, we will use conventional FMR to determine two important magnetic properties of thin films, the perpendicular magnetic anisotropy (PMA) and the damping of the film. Of course, we determined PMA with VSM in the previous section, so the FMR measurement of PMA is just a check or verification of a value that we already know. However, magnetic damping can not be determined from VSM, and as damping is a crucial parameter for us, it was primarily this parameter that we hoped to determine from this measurement. I will present measurements of both PMA and damping in the paragraphs to follow.

Flip-chip FMR involves putting a magnetic thin film into very near proximity to a microwave waveguide, as shown in figure 2.6. Practically, this means fabricating a magnetic thin film on top of a wafer, cutting out a small chip of that wafer, and then flipping that chip to sit face-down, in physical contact, on top of the waveguide—hence the name. (Surface oxide prevents the chip from shorting out the waveguide, but doesn't interfere with the magnetic interaction.) As shown, there are two magnetic fields that affect the sample. The static field, H_{ext}, is much larger, and sets the equilibrium direction of the magnetic sample. The smaller

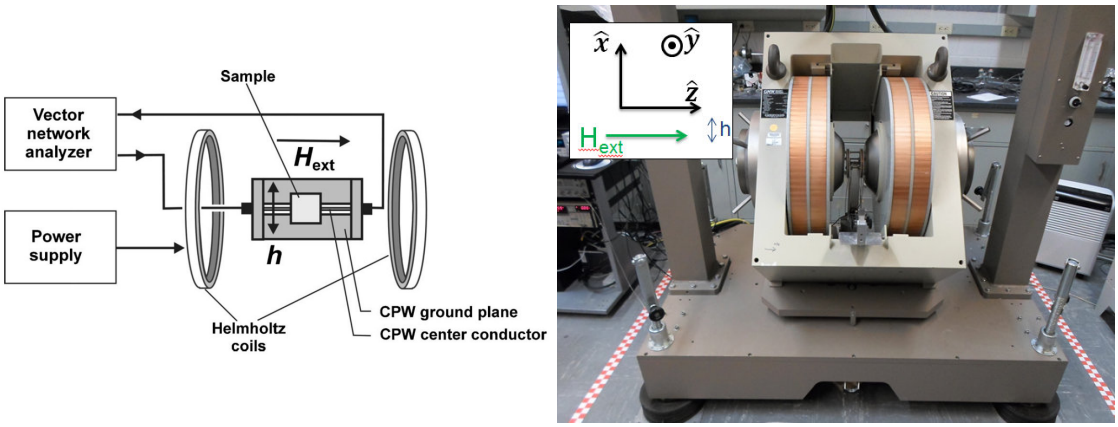

Figure 2.6: (Left) A schematic diagram of our FMR setup. A large pair of electromagnets produces a large static field, H_{ext}. The network analyzer sends a gigahertz-frequency signal down the coplanar waveguide (CPW). This causes current to flow in alternating directions along the center line, which results in an oscillating magnetic field pointing along the surface of the chip and perpendicular to the direction of the center line, h. The transmission or reflection from this setup is then read back in by the network analyzer. Diagram is reproduced from Kalarickal et. al. [52]. (Right) A photo of our FMR setup. Primarily we see the large electromagnets that produce H_{ext}. The sample was mounted vertically in between the two large plates shown. The magnets could be rotated around the sample to change the orientation of H_{ext} relative to the sample. The electromagnet was controlled by a computer and a large power supply, not shown. Four wires attached to the magnet itself served as a primitive hall probe, which we calibrated using an external gaussmeter, and then monitored continuously to measure H_{ext}.

oscillating field from the waveguide, h, perturbs the equilibrium magnetic position of the magnetic thin film. We think of this field as linear in the area of interest, but of course it is an elliptical field that goes all the way around the center line of the CPW. (The CPW guide must be wide enough so that most of the magnetic field is linear in character. In practice, a 100um center line easily satisfies this constraint.)

When a ferromagnet is perturbed as shown, it will begin to precess around its equilibrium position, as discussed in the previous sections. If the driving field from the waveguide oscillates with the same frequency as the ferromagnetic precession, the oscillating field will reinforce the motion of the ferromagnet, creating "ferromagnetic resonance". The properties of this resonance can be derived from the Landau-Lifshitz-Gilbert (LLG) equation as follows.

2.4.1 Theory of Ferromagnetic Resonance in the Presence of Surface Anisotropy Energy

The theory of FMR is well established, and others have done the algebra to show what a ferromagnetic resonance curve should look like[53]. I wanted to add surface anisotropy energy to the model. I will outline the calculation below, and ultimately show numerical results from the theoretical closed form that I derive. I will then use this model to fit observed ferromagnetic resonance peaks in the next section.

We set the coordinate axes as shown in figure 2.6, such that $\hat{z}$ is the direction of the applied magnetic field and $\hat{x}$ is the direction of the oscillating magnetic field. The external field H_{ext} will cause the magnetization to point primarily $\hat{z}$ direction, and the oscillating field from the CPW, h, will cause the magnetization to precess slightly in the x-y plane. We assume a first order perturbation, that is,

$m, h << M, H_{ext}$. So the magnetization, in $[\hat{x}, \hat{y}, \hat{z}]$ notation, is

$$\mathbf{M} = \left[m_x e^{i\omega t}, m_y e^{i\omega t}, M_S\right] \tag{2.8}$$

where m_x and m_y are complex, unknown coefficients. The magnetic fields are $\mathbf{H} = \mathbf{H_{ext}} + \mathbf{h} - \mathbf{H_d}$. Here I will write $\mathbf{H_d} = \mathbf{NM} - \mathbf{N_{SO}M}$. The term $\mathbf{N_{SO}}$ expresses the surface anisotropy energy and has the following form:

$$\mathbf{N_{SO}} = \frac{E_S}{\frac{1}{2}\mu_0 M_S^2 t}(2N+1)\hat{\mathbf{n}} \tag{2.9}$$

In general, this form of the surface anisotropy is not the same as the surface anisotropy we previously defined: this form leads to an anisotropy energy $\propto \mathbf{M} \cdot (\hat{\mathbf{n}}\mathbf{M})$, which has a subtly different angular dependence than the usual surface anisotropy energy $\propto (\hat{\mathbf{M}} \cdot \hat{\mathbf{n}})^2$. (As above, I am using the notation $\hat{\mathbf{n}}\mathbf{M} = n_x M_x \hat{x} + n_y M_y \hat{y} + n_z M_z \hat{z}$.) But in this case, we're only interested in small angles, where $\mathbf{M}$ varies by a small perturbation from an equilibrium position that is either parallel or perpendicular to $\hat{\mathbf{n}}$. In this regime, the two formulations are equivalent. For ease of calculation, we introduce a new term that encapsulates the shape and surface demag factors: $\mathbf{N'} \equiv \mathbf{N} - \mathbf{N_{SO}}$. Now we can write down the full expression for H.

$$\mathbf{H} = \left[he^{i\omega t} - N_x' m_x e^{i\omega t}, -N_y' m_y e^{i\omega t}, H_{ext} - N_z' M_S\right] \tag{2.10}$$

We can substitute these expressions into the LLG equation, which is

$$\dot{\mathbf{M}} = -\gamma_0 \mathbf{M} \times \mathbf{H_{eff}} + \frac{\alpha}{M_s}\mathbf{M} \times \dot{\mathbf{M}} \tag{2.11}$$

The real and imaginary parts of the LLG equation in $\hat{x}$ and $\hat{y}$ give four linear equations which I solved to find the real and imaginary parts of m_x and m_y. These are long and messy, so I won't write them out in full, but I'll use them in just a moment.

When doing our FMR measurements, we measure the transmission scattering coefficient, S_{21}, through the coplanar waveguide. We see a dip in transmission—a peak in absorption—at certain frequencies. We wish to relate the magnetic

response described by m_x and m_y to the absorption that we measure. The energy of a magnetic system with volume V is $E = -V(\mathbf{M} \cdot \mathbf{H})$, so

$$\frac{dE}{dt} = -V(\mathbf{M} \cdot \frac{d\mathbf{H}}{dt} - V\frac{d\mathbf{M}}{dt} \cdot \mathbf{H}) \tag{2.12}$$

Of course, the total energy change of the magnetic system is zero–we haven't modeled any decay of the precession, we've modeled steady state motion. That just implies that the two terms in equation 2.12 cancel one another out, which is another way of saying that we're replacing the energy lost to damping with energy from the applied microwaves in the coplanar waveguide. The absorption that we're actually measuring is one of those two terms, the amount of energy we have to put into the system to compensate for the energy lost to damping. Using the expressions for $\mathbf{H}$ and $\mathbf{M}$ in equations 2.8 and 2.10 above, average absorption over a period of rotation is

$$< dE/dt >= \frac{V}{2\pi/\omega}\int_0^{2\pi/\omega} \frac{d\mathrm{Re}[\mathbf{M}]}{dt} \cdot \mathrm{Re}[\mathbf{H}]dt = \frac{1}{2}h\omega\,\mathrm{Im}(m_x) \tag{2.13}$$

Using the result for m_x derived from solving the LLG equation:

$$< dE/dt >= \frac{\frac{1}{2}Vh^2M_S\gamma_0\alpha\omega^2(\omega^2(1+\alpha^2)+\gamma_0^2\tilde{H_y}^2)}{(\omega^2-\omega_0^2)^2+\alpha^2\omega^2(\omega^2(2+\alpha^2)+\gamma_0^2(\tilde{H_x}^2+\tilde{H_y}^2))} \tag{2.14}$$

where $\tilde{H_x} \equiv H_{ext}-(N_z'-N_x')M_S$ and $\tilde{H_y} \equiv H_{ext}-(N_z'-N_y')M_S$ and $\omega_0^2 \equiv \gamma_0^2\tilde{H_x}\tilde{H_y}$. To go from $< dE/dt >$ to energy lost, ΔE, we should integrate over some time that will depend on the length of the sample and the speed of the microwave in the waveguide, and we should estimate h from the geometry of the waveguide and the input power. However, I'm not interested in the absolute height of the absorption curve at this time, only it's shape and position, so I'll let $h \to 1$ and just use expression 2.14 for energy lost. S_{21} is actually defined as $S_{21} \equiv |V_{out}|/|V_{in}|$, so technically $S_{21} \propto c-(\Delta E)^{1/2}$, where c is the background loss from the experimental apparatus. From this theoretical expression, the S_{21} that we might expect for typical experimental conditions is shown in figure 2.7a.

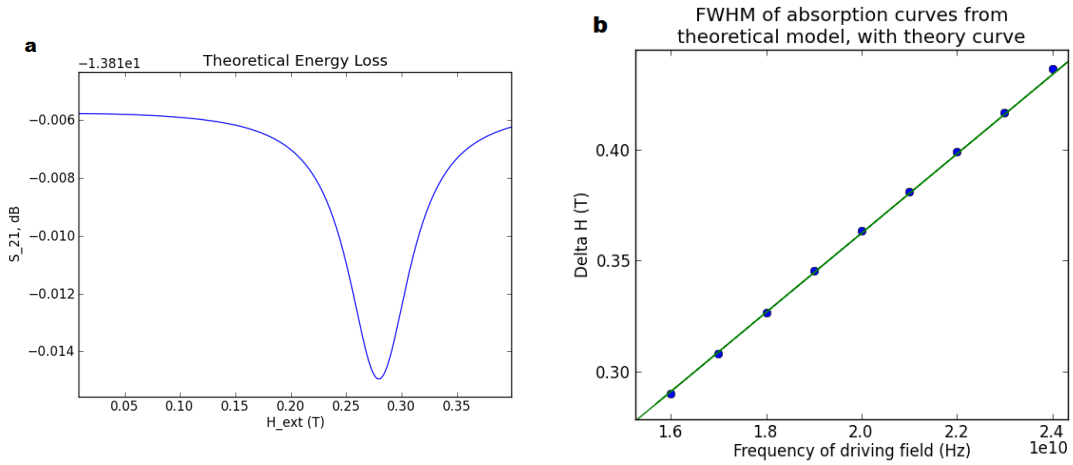

Figure 2.7: (a) Theoretical prediction of transmission amplitude, S_{21} from equation 2.14. The physical parameters have been chosen to match the sample shown in figure 2.8 as closely as possible: $f = 8$ GHz, $\alpha = 0.12$, $N_{SO} = 0.99$, $M_S = 1.25$, and in-plane geometry ($N_y = 1$). (b) Theoretical prediction of ΔH as various frequencies. Each point is the FWHM of a simulated transmission curve like the one shown in blue in figure (a). The geometry and physical parameters of this theoretical "sample" have been chosen to match the sample shown in figure 2.10a below: $\alpha = 0.25$, $N_{SO} = 1.382$, $M_S = 1.033$, and out of plane geometry ($N_z = 1$). The fitting line comes from equation 2.16, and shows that the predicted slope matches the model nearly exactly.

The first notable aspect of this plot is the x-axis. When thinking about finding the resonant frequency of a harmonic oscillator, it is most natural to think about changing the frequency of the driving force off of resonance. But in this case, the resonant frequency depends on external magnetic field, H_{ext}, so we can either vary the frequency while holding the magnetic field fixed, or vary the magnetic field strength while holding the frequency fixed. It is more common in the literature to detune field, and this is what we have done here.

The minimum value of the curve shown in figure 2.7a tells us about the magnetic anisotropy. The peak position can be found theoretically by solving $d\Delta E/dH = 0$. Doing so gives an expression for H_{min} as a function of known experiment inputs including ω, and N_{SO}, the value that we would like to calculate. However, this expression is messy. The Kittel approximation[54], assuming that $\alpha \to 0$, immediately gives the much cleaner result that absorption is maximized when $\omega_0(H_{ext}, N_{SO}) = \omega$. Expanding that equation out for the present, in-plane case ($\hat{n} = \hat{y}$, $N_x = N_z = 0$, $N_y = 1$) means

$$f^2 = \left(\frac{\gamma_0}{2\pi}\right)^2 H_{min}(H_{min} + M_S(1 - N_{SO})) \tag{2.15}$$

Putting the absorption peak position from figure 2.7a into this equation as H_{min} gives N_{SO} of .990, which is exactly the value used to generate the curve. So going forward, we'll just use the Kittel approximation, $\omega_0(H_{ext}, N_{SO}) = \omega$, to derive N_{SO} from the peak position. (The purpose of this exercise was to generate a theoretical prediction curve which we could compare to actual data, and to verify that the Kittel approximation gives reasonable values for H_{min} using a more exact numerical simulation. But since we've simulated real data, it's interesting to note that in this sample, we seem to have chosen Co and Ni thicknesses such that the surface anisotropy nearly exactly cancels the shape anisotropy–this is the physical meaning of $N_{SO} = 0.990$. The VSM data for this particular sample supports

this idea—both in-plane and out-of-plane measurements show some hysteresis in roughly equal amount.)

The width of the curve is controlled by the damping parameter, α. Further algebraic manipulation of equation 2.14, which I have not reproduced but which can be found in the literature[53], shows that the full width at half-maximum (FWHM) of the curve, ΔH, is given by

$$\Delta H = \frac{4\pi\alpha f}{|\gamma_0|} \tag{2.16}$$

From this expression, one determines the damping, α, since one measures ΔH and the other values are known. As a sanity check, I verified that my expression for absorption given in equation 2.14 does give the correct value for the linewidth by simulating many curves like the one shown in figure 2.7a, extracting the FWHM of each, and showing that the resulting points fall on a line with the predicted slope. This result is shown in figure 2.7b. Interestingly, in the experimental literature, when people make the same kind of curve with real data, they observe that there is some additional term added to the right hand side of equation 2.16, ΔH_0, referred to as the inhomogeneous broadening[52][42]. This constant has been observed consistently in amorphous or textured magnetic materials, and seems to depend strongly on the materials used and the thermal history (i.e. annealing) of the sample [55].

We have finished demonstrating what one expects from FMR measurements, how one can use those measurements to derive E_S and α in theory, and how the appropriate equations are derived. As an aside, it's worth noting that this problem is similar to the damped, driven, simple harmonic oscillator of freshman physics. The α term is the damping, the h term is the driving force, and the resulting position oscillates. Like the simple harmonic oscillator, we see a resonance peak that is roughly Lorentzian in shape.

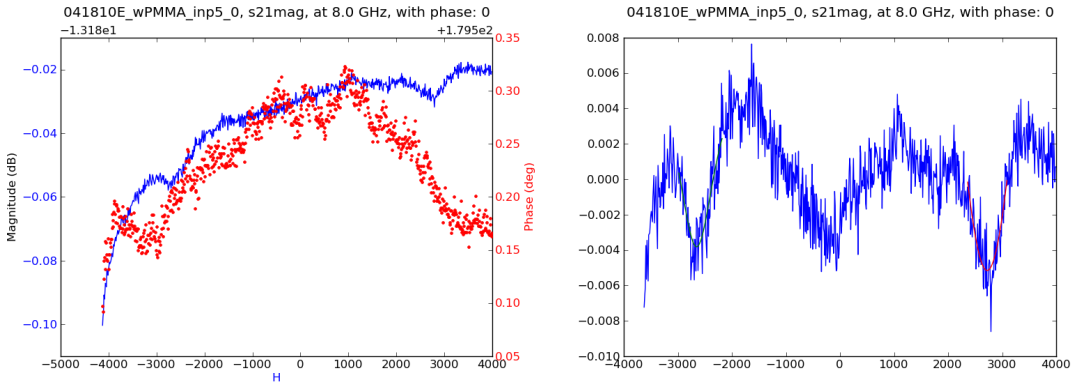

Figure 2.8: (a) Raw FMR data from the network analyzer as we apply a 8.0 GHz CW signal to a [Co (4.1 Å)/Ni (3.5 Å)]x8 sample and vary the applied external field. The blue curve is transmission amplitude down the microwave waveguide, S_{21}, measured in dB relative to the input signal. It shows absorption peaks at $\pm$2700 Oe. The red dots are the phase of S_{21} relative to the output signal. (b) The same amplitude data with the range slightly restricted and a linear background subtracted off. Here one can see the Lorentzian absorption peaks that have been fit by my automatic peak-fitting algorithm shown in green and red. The FWHM of this curve, ΔH, is $\approx$ 680 Oe.

2.4.2 FMR Measurements of Co/Ni Films

An example of a measured FMR spectrum is shown in figure 2.8. The first task is to measure the peak position, and use it to calculate E_S. We can do this for a single transmission vs H curve, but to make the measurement more accurate, we vary frequency and measure many peaks of this kind. Combining the peak position of each measurement gives the curve shown in figure 2.9. Fitting a line of the form specified by equation 2.15 gives N_{SO} of 0.99, which translates to E_S of 0.22 mJ/m^2, a value that is similar to what we found with VSM.

We also measured samples with the external field applied perpendicular to the sample. In order to keep the external fields necessary for resonance low enough that we could reach them experimentally, it was usually necessary to measure the sample with the applied field in the equilibrium direction of the magnetization. In other words, samples with out-of-plane equilibrium magnetization needed to be measured

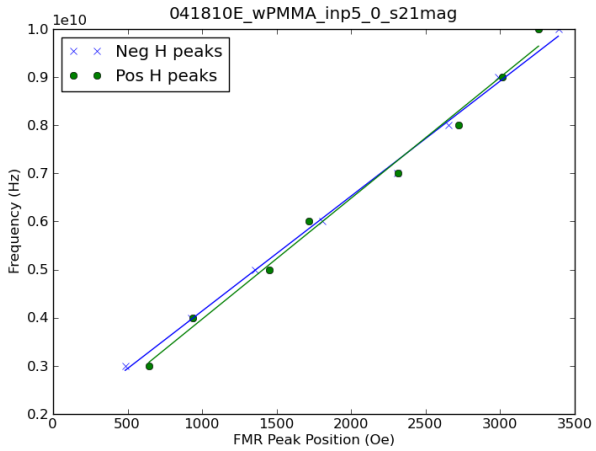

Figure 2.9: Composite FMR data for the [Co (4.1 Å)/Ni (3.5 Å)]x8 sample. Each point is generated from a plot like the one shown in figure 2.8, but with the input signal from the network analyzer applied at a different frequency. The blue 'x's show the position of the left hand peak, for negative H_{ext}, and the green dots show the position of the right hand peak, for positive H_{ext}.

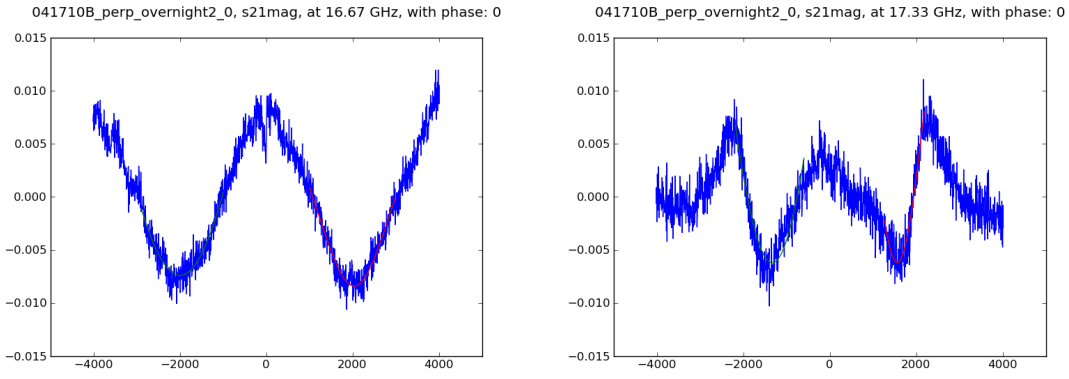

Figure 2.10: Two examples of raw data of a sample measured in the perpendicular orientation. The x-axis is the external field in Oe, while the y-axis is the log of the transmission power, S_{21}, in dB. In both cases, a linear background has been subtracted off so that the curve is centered around 0 in y. This sample [Co(3.6 Å)/Ni(8.5 Å)]x8.

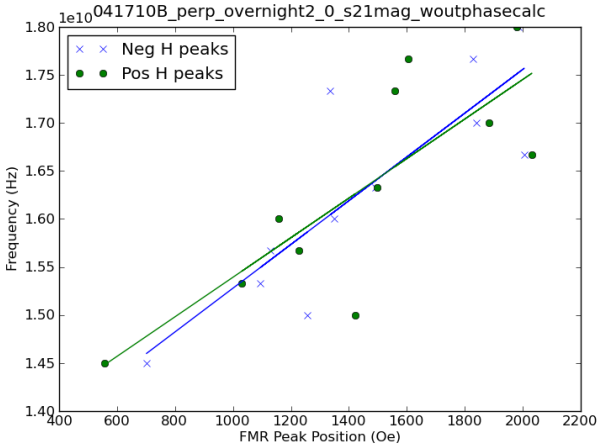

Figure 2.11: Composite peak position data for the [Co(3.6 Å)/Ni(8.5 Å)]x8 sample. Each point is generated from an absorption vs field plot like the ones shown in figure 2.10, but with the input signal from the network analyzer applied at a different frequency. The blue 'x's show the position of the left hand peak, for negative H_{ext}, and the green dots show the position of the right hand peak, for positive H_{ext}.

with a perpendicular field. Example data for this geometry is shown in figure 2.10. By combining many resonance peaks like that one taken at various frequencies, I constructed the curve shown in figure 2.11, which we again fit to $\omega = \omega_0(H_{ext}, N_{SO})$. In this case, $\hat{n} = \hat{z}$, $N_x = N_y = 0$, $N_z = 1$, so $\omega = \gamma_0(H_{ext} - M_S(1 - N_{SO}))$, and we find $E_S = 0.32$ Oe. Again, we are reasonably close to the value determined by FMR, although there is clearly some difference from sample to sample.

Now let us consider the width of these curves and discuss the damping parameter, α. Unfortunately, the data for peak width is so noisy, it's impossible to construct a line like the one shown in figure 2.7b. Without such a curve, it's impossible to determine ΔH_0, the inhomogeneous broadening. If one neglects ΔH_0, then the [Co (4.1 Å)/Ni (3.5 Å)]x8 sample at 16.67 GHz shown in figure 2.10a has a damping value of $\alpha = .25$, and the linewidth of the [Co (4.1 Å)/Ni (3.5 Å)]x8 sample at 8.0 GHz shown in figure 2.8b gives $\alpha = .12$. Recall that we expect $\alpha = .02$[42], so these values are larger than expected by an order of magnitude. If we compare our linewidths to what was observed in the literature, the inho-

mogeneous broadening is not enough to explain this discrepancy. Beaujour[42] measured $\Delta H_0 \approx 200$ Oe ± 100 Oe, depending on the sample. Using his values for ΔH_0 would only bring our linewidths down by a factor of $\frac{1}{3}$ at best. Beaujour did observe that perpendicular measurements ($\hat{n} = \hat{z}$) seem to have larger inhomogeneous broadening than in-plane measurements ($\hat{n} = \hat{y}$), a trend that was very evident in our data as well. But in either orientation, our linewidths seemed much too large for the material in question.

It is tempting to try to blame inhomogeneities in the samples themselves, for if the effective surface anisotropy varied slightly from one small region of the chip to the next, that would result in line broadening. However, there is reason to believe that these anomalously large linewidths are a function of the measurement setup, not the samples. When John Reed at NIST measured one of our films, [Co (4 Å)/Ni (8Å)]x2/FeCoB(11 Å), he found damping of $.015 \pm .005$[56]. It is possible that John Read's sample was treated in some way that the samples shown here were not, but it is more likely that our measurement setup was at fault. For example, if the microwave pulse itself was broadened in some way, that would result in a broader linewidth, regardless of sample.

One way or another, our measurements were very inconsistent, especially the out-of-plane measurements. Comparing figures 2.10a and 2.10b, if we try to force a Lorentzian dip onto the data, we get very different peak widths. The line shapes of these two curves are quite different, even though these measurements come from the same sample, and differ only in the frequency of the applied microwaves. Figure 2.10b looks more like a Fano resonance than a Lorentzian dip, and actually, calculating the expected peak position from 2.11, an anti-symmetric curve would make the center position more in line with the rest of the data. (S_{21} phase for the figure 2.10b data set, not shown, also changes most strongly at 2000 Oe, not at the

minimum at 1400, which further supports this idea that this curve's true center is at the zero-point of an anti-symmetric curve.) All of the curves from this sample appeared to be various combinations of symmetric and antisymmetric curves in various ratios. Several possible physical explanations for this seem possible. One possible theory is that the sample itself, sitting directly above the waveguide, is capacitively coupled to the waveguide and acts as a second transmission line. In the waveguide, the phase of the wave increases at a constant rate, but in the sample, the phase doesn't change significantly. When the two waves recombine, they are offset in phase and constructively and destructively interfere in some way. Another theory is that we're seeing multiple modes of the coplanar waveguide. Coplanar waveguide has an even mode, the "slot" mode, in addition to the usual symmetric "odd" mode. These various modes would excite different dynamics in the magnetic material. We could also be seeing the results of some sort of reflection at the joint between the pins and the coplanar waveguide–multiple reflections might recombine slightly out of phase.

One is tempted to try to fit some sort of Fano lineshape to these curves, but they're simply too noisy to give a reliable line width in that case. As one can see from the raw data shown in figure 2.8a, the background noise in these measurements was considerable. We analyzed reflection data, S_{11}, and phase data, but both were noisier than transmission. Without reducing the noise, it was impossible to calculate α or do further analysis of what could be wrong with our setup. In order to do more careful science, we concluded that we had to find a way to make the setup less noisy.

Figure 2.12: The waveguide onto which we placed our samples for FMR measurements. On the right, we see the aluminum plate which was mounted vertically between the large electromagnets shown in the figure 2.6. At the top of this plate we see the two microwave connectors which were screwed into flexible coaxial lines and connected to the input and output of the network analyzer. These two connectors sit on top of two rigid copper coaxial lines which connect with the center line of the coplanar waveguide chip, which is the gold square in the center of the apparatus in the photo on the left. That connection is covered in the photo on the right, but it takes place under the four set screws shown (in a horizontal line, two on each side). The coplanar waveguide itself is a barely-visible slit in the center of the gold square. The sample sits on top of this slit.

2.4.3 Improving the Experimental Setup for FMR measurement

Our FMR measurement setup is shown in figures 2.6 and 2.12. This apparatus worked well enough to take the data shown above, but it had some limitations. The noise changed rapidly with the magnetic field, so it seems likely that there was some magnetic response of either the cables or connectors that comprised the system. The coplanar waveguide itself was also quite crude, and not at all mechanically secure. The connection between the rigid copper coaxial lines and the coplanar waveguide chip was a particular weakness. That connection is covered in the photo shown, but basically consists of a pin from the coaxial cable pressed onto the waveguide. While push fittings of this type can be quite secure, this one was not. The flexible lines which connected the waveguide to the network analyzer across the room rested with their weight on the two rigid copper lines shown. When they swung or moved, this changed the force on these two rigid copper lines, which directly changed the force holding the pin onto the coplanar waveguide (CPW). The connection between the chip itself and the sample was also insecure. In general, we used heat sink paste to glue the sample facedown on top of the center line of the CPW. The magnetic sample would then be subjected to magnetic fields potentially as large as a Tesla with only the weak paste to hold it in place. When finished with a sample, we would easily pull the sample off with tweezers. We would then spray the CPW with acetone and IPA to clean it, and mount the next sample. This cleaning process was not very effective, and likely left a significant residue of heat sink paste in the cavity.

In an effort to make the connections more solid, the sample mounting more secure, and remove the paste, we set out to replace the coplanar waveguide and the surrounding connections. I designed a sample box, shown in figure 2.13 out of

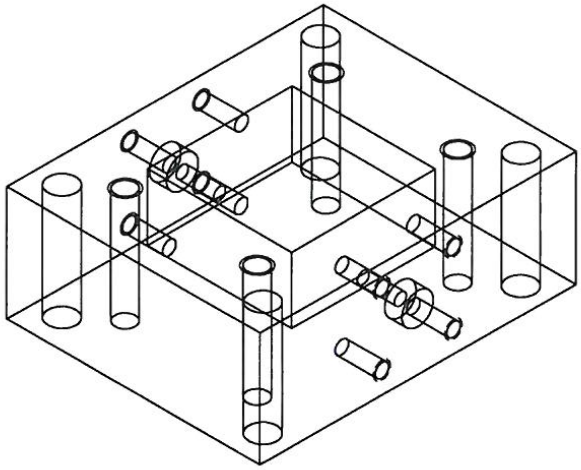

Figure 2.13: A schematic of the sample box used for FMR measurements.

brass, and installed non-magnetic SMA female connectors for each side. The center pin of those connectors was press-fit onto a sapphire chip which had a coplanar waveguide on top. The sample was designed to sit in the center of this box. A spring-loaded delrin plunger which extended down into the center of the box was attached to the lid, so that when the lid of the box was screwed on, the plunger was in contact with the back of the wafer, holding it securely in place.

A coplanar waveguide was chosen for the center line because of its ability to maintain 50 ohm impedance at different scales. At each end, the center line was 500 microns wide, with side gaps of 296.1 microns. This tapered down to a center line that was 5 microns wide with side gaps of 2.8 microns after 1 mm. (Actually, the taper of the side gaps wasn't quite linear–there was one intermediate point near the halfway point of the taper with a center line width of 250 um and side gap width of 132.6 um.) These values were chosen by calculating the impedance of the CPW from the basic formulas in [57] and trying to keep the impedance at $50 \pm .5$ ohms at every point along the taper. Using the Heidelberg laser mask writer in the CNF, I wrote a mask of this description called "FMR_AL2O3_CPW".

Actually, small offsets were added to the center line size to account for the process bias measured during a dose test. These offsets were 0.2 μm for the narrowest center line, 1 μm for the wider points.

The chip was microfabricated in the Cornell Nanofabrication Facility according to the following recipe:

- Dice 500u thick sapphire into exactly half inch chips.
- Clean the chips by sonication for a minute each in acetone and IPA.
- Spin HMDS and then a standard g-line photoresist (like Shipley 1813) at 3 seconds for 3500 (ramp 3K) then for 60 seconds @ 3K. The faster-then-slower spin reduces the size of the edge bead.
- Bake 60 seconds at 115 C.
- Using the appropriate mask, expose the resist on a g-line stepper. (I used the 5x). Make sure the stepper is in "transparent substrate" mode.
- In an image reversal oven, like the YES, pump the chip to vacuum and then expose to 600mTorr NH3 for 45 minutes. This renders the exposed resist insoluble to developer.
- Flood expose on a contact aligner. (I used 67 seconds on the ABM.)
- Develop 90 seconds in 0.210 normal TMAH, such as MF321. This procedure effectively reverses the exposed pattern. Importantly, this creates a negative profile for the resist.
- Evaporate 500nm of Cu at 0.5 Å/s and liftoff in acetone.

When this chip was installed, there was some problem getting connection between the pin and the CPW–the pin would scratch the copper off the surface instead of making secure contact. Initial attempts to solder the copper center line

to the pin were unsuccessful; coating or replacing the copper line with another metal that is easier to solder may be necessary. This issue was never resolved, and this box was never tested in the FMR setup.

2.5 Fabrication and Characterization of Micron-Sized Co/Ni Magnetic Tunnel Junctions

Ultimately, our goal was to show that we could incorporate Co/Ni multilayers into a successful MRAM bit, and to characterize such a bit. To do this, we needed not only Co/Ni multilayers, but an MgO barrier with a top and bottom electrode—a free layer and a fixed layer. We call any such device a magnetic tunnel junction, or MTJ. We needed to characterize the MgO quality of our stack to ensure that the tunneling magnetoresistance (TMR) of our bit would be high. As will be discussed, there were reasons to believe that the introduction of Co/Ni layers into our stack would reduce TMR.

We then needed to fabricate a nanoscopic sample of this stack so that we had a single domain during the switching process. Experience showed that we would have multiple magnetic domains in the sample above a diameter of about 100 nm. However, the fabrication of a nanopillar, as we call these nanoscopic multilayer stacks, takes about 3 weeks of full time fabrication work. It's time intensive. So our plan was to first lay down the appropriate multilayer stack and make micron-sized junctions. Junctions at the micron size are achievable with photolithography only, and only take a few days to fabricate. We can still use these larger junctions to characterize the MgO quality by measuring the TMR of the device. Once we had high quality MgO and a good TMR, we would make a nanopillar of the same material stack demonstrate spin torque switching. We'll describe these experiments

below.

2.5.1 Sputtering Metal Stacks for MTJs

The first step in making micron-sized MTJs is laying down the appropriate stack of materials. We did this with magnetron sputtering. We used two different sputtering systems over the course of this experiment, a 7-gun AJA ATC series with 2" targets and a typical base pressure in the high 10^{-9} Torr range, and a 6-gun Kurt J. Lesker sputtering system with 3" targets and a typical base pressure in the low 10^{-9} Torr range. All MgO deposition was done with RF sputtering, while all metal deposition was done with DC sputtering. Our devices were made on Si/SiO2 wafers with 500nm of thermal oxide grown on a silicon wafer of 10-20 ohm-cm resistivity. To make a stack of materials of given thicknesses, we generally began by characterizing the deposition rate of each material individually. On a dummy wafer, we would photolithographically pattern resist into a basic grating pattern, deposit at least 250 Å of a given material, and then put the chip in acetone to lift-off the resist. We would then use a surface profilometer (a Tencor P10) to make at least 10 measurements of the step height and average those measurements. We calculated a deposition rate from these numbers, and deposited off the clock for all future depositions.[1] There was no crystal monitor in the chamber. We believe that this calibration method was reliable to better than 5%, although it is sensitive to resist residue, systemic errors in the profilometer, spatial non-uniformities in the deposition itself, and changing conditions over the course of the 2-3 weeks of depositions we would do between calibrations.

[1] A note to any future users of the Lesker deposition system: we found that there was a 3.7 second delay between the moment that the shutter opened and when the software began counting the deposition time. This 3.7 seconds translates to 4-6 Å of Co or Ni, and is therefore somewhat significant when laying down very thin layers. I have compensated for that delay in all reported data, but anyone trying to reproduce these results on the Lesker system should do so with care.

Unless otherwise noted, all layers were deposited at an argon pressure of 2 mTorr, with the exception of the platinum, which was often deposited at 3.5 mTorr. Some of the later samples that were deposited on the Lesker were run at 1 mTorr for all the metal layers, although the MgO gun was always run at 2 mTorr to ensure plasma stability. All samples were rotated during sputtering, to ensure more uniform thickness. Samples were sputtered in the presence of a magnetic field pointing along the plane of the wafer that was about 50 G in strength[2] in order to align the magnetic domains during sputtering.

Although we deposited metal stacks in many variations over the course of this project, one stack that we would go on to process and measure extensively was Ta(30)/ $[CuN(200)/Ta(30)]_2$ / Cu(20)/ $[Co(4)/ Ni(8)]_2$/ $Fe_{60}Co_{20}B_{20}(11)$/ MgO(11)/ $Fe_{60}Co_{20}B_{20}(200)$/ Ta(80)/Pt(300), where all thicknesses are in Å. In general, those materials were sputtered from stoichiometric targets of the same composition. The exception was the CuN which was formed from a copper target sputtered in the presence of N_2 gas. In general, we deposited most of the metals between 40-100W, although we deposited the Co and Ni as slowly as possible, at 20W. The MgO went down at 300W. Of course, these powers are system specific and are not of general interest, but might be of use to any future student trying to reproduce these results. We should also note that the we always sputtered the MgO with the tantalum gun lit to act as a getter for some of the O2, as a number of groups in the field report doing. Even with this trick, the MgO we deposited may not have been stoichiometric, although it was sputtered from a stoichiometric MgO target. MgO sputtering is a PhD topic of its own[58], and different groups have different techniques, including the sputtering of a combination of Mg and MgO, and reactive sputtering of pure Mg in the presence of a partial pressure of

[2]At least the field was 50 G on the Lesker—the AJA field strength was unknown, but was thought to be comparable.

O_2. I didn't do much experimentation on the MgO barrier itself, but I did find that the manufacturer of the MgO target made a large difference. For unknown reasons, I had the best luck with MgO targets from Angstrom Sciences.

The first 6 layers mentioned here, Ta(30)/[CuN(200)/Ta(30)]$_2$/Cu(20), are a smoothing layer. This is a legacy Buhrman group recipe that was characterized most closely by John Read[58]. Some metal is necessary under the bottom magnetic layer as a buffer for overetching when defining the junction, but this particular form of repeating Ta and CuN was used because John found it to be particularly smooth as measured by atomic force microscopy (AFM). I only studied these smoothing layers a little, but I did find that slower deposition led to smoother films on the AFM.

The top layer, the platinum, was added because it doesn't oxidize and therefore makes good electrical contact with a probe. The thickness of the Pt is not sensitive– it just needs to be thick enough to prevent a sharp probe tip from punching through it. The Ta was a legacy recipe that may not have been necessary here. We will discuss the electrodes and MgO barrier in more detail below.

After deposition, it was necessary to anneal the sample in order to crystallize the electrodes[59]. Of course, during anneal, the various metal species also began to interdiffuse, and both the literature and our own experience suggest that too much annealing reduces the device TMR. (Actually, boron diffusion can improve TMR[58], but Ta diffusion degrades performance[29].) Annealing also affects the stress and crystal structure of the MgO, and has other effects which turn on at different temperatures. We did not study these mechanisms closely. Instead, we quickly scanned through different anneal times and temperatures, and found that annealing for 3 minutes at 375 ^{o}C before patterning led to the best TMR. This anneal was done in a nitrogen glove box (or, later, in a vacuum tube) to prevent

oxidation of the magnetic metals. The anneal was also done in the presence of an in-plane magnetic field, similar in orientation to the field applied during sputtering.

2.5.2 Fabricating Micron-Sized Co/Ni Tunnel Junctions

Once the metal was deposited, the next step was to define a micron-sized junction. This was done with a 3 mask fabrication process at the CNF. The mask design is shown in figure 2.14. The fabrication recipe is as follows:

- Define the bottom electrode. Spin a thick g-line novolac photoresist, such as Shipley 1827 (30" @ 2K), and step the "Micron MTJ #1" mask across the wafer on a stepper (1.5" exposures on the 5x). Develop in TMAH developer, such as 300 MIF, for 1.5' or until clear.
- Ion mill through all of the metal layers. Over etch by about 2'. I used "Praveen's Ion Mill", a Veeco with a RGA end point detector, milling at 135° and 50 mA for about 12' but really until the metal signals receded in the RGA. Note that on this tool, 180° is milling straight down, perpendicular to the wafer.
- Remove the resist in acetone, with sonication if necessary.
- Define the micron pillar with the same resist recipe and the mask "Micron MTJ #2".
- Ion mill into the smoothing layer, through the first Ta peak on the RGA. I used 6' @ 160°, 50 mA. After milling, clean the sidewalls of redeposited material for 1:30 @ 115°.
- Deposit 1.5 times as much SiO_2 as the amount of milling just completed. We usually did this on the "old IBD", an ion beam deposition system acquired

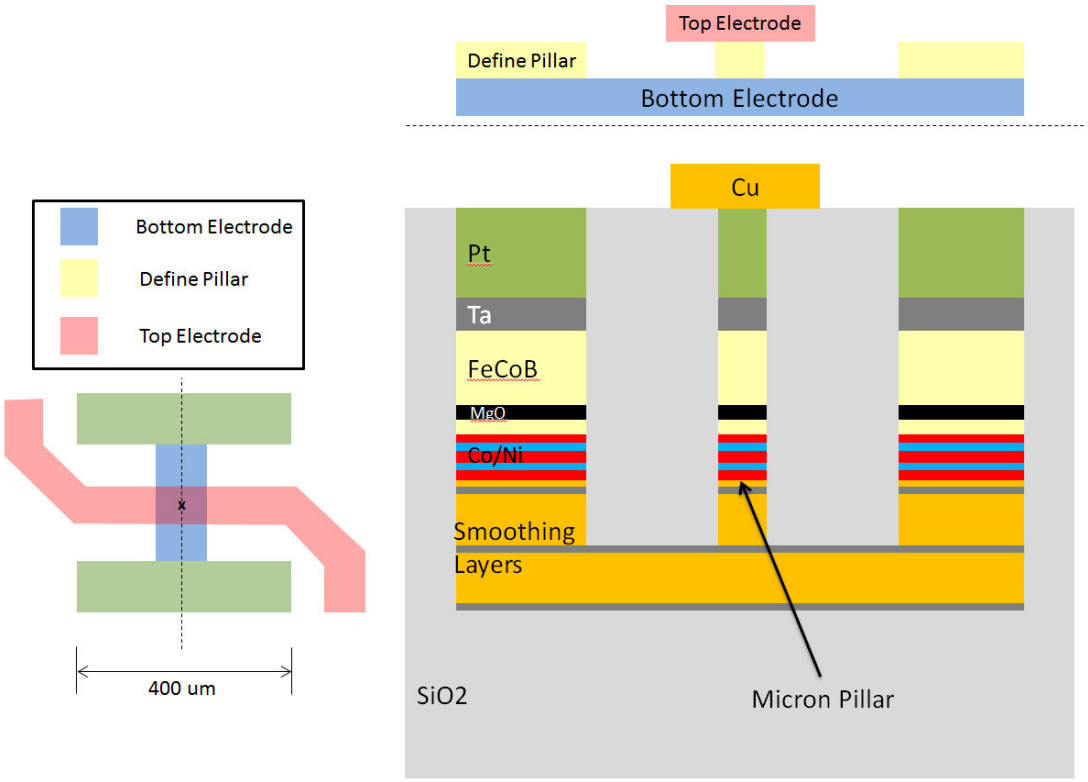

Figure 2.14: Schematics of the micron junction devices. On the left, a top view of these devices, with each of the three masks shown. Note that green region is an overlap of "Bottom Electrode" and "Define Pillar". The 'x' shows where the micron-sized pillar is, although at scale it is too small to be seen. The micron pillars we made were ellipses ranging in size from 10x10 μm^2 to 3x5 μm^2, and with a range of eccentricities from round to 3x9 μm^2. The diagram on the right shows a cross section of the device taken along the dotted line shown on the left. This diagram is not to scale. The rectangles above the dotted line on the left show where the three masks line up on this diagram, and are not representative of metal layers.

from IBM's TJ Watson Research Center, but any evaporator or sputterer should also work.

- Lift off the resist in acetone overnight. Sonicate 1' in the morning. Repeat if necessary.
- Define the top electrode. Coat the wafer with HMDS, then spin a normal g-line photoresist, such as Shipley 1813 (30" @ 2K), and step the "Micron MTJ #3" mask on a stepper (1" exposure on the 5x). Develop in TMAH developer, such as 300 MIF, for 1' or until clear.
- Deposit a thick copper electrode. We usually deposited 300 nm on the old IBD, although evaporation also works.
- Lift off the resist in acetone.

Interestingly, the "bottom electrode" mask step isn't strictly necessary–the devices work equally well with an extended bottom layer that extends over the whole wafer. This layer is isolated from the top layer by the oxide. However, when probing the top electrode, we found that the sharp pins sometimes punched through the top electrode and oxide layer and made contact with the bottom layer accidentally. It was easier to measure the devices if there was nothing under the top electrode.

2.5.3 Electrical Measurements of Micron-Sized Tunnel Junctions

When we measured the resistance of the micron junctions fabricated in this way as a function of applied magnetic field, we got curves like the one shown in figure 2.15(a). When taking these measurements, we start with a very high field and slowly reduce it. Initially, both free layer and fixed layer have magnetizations

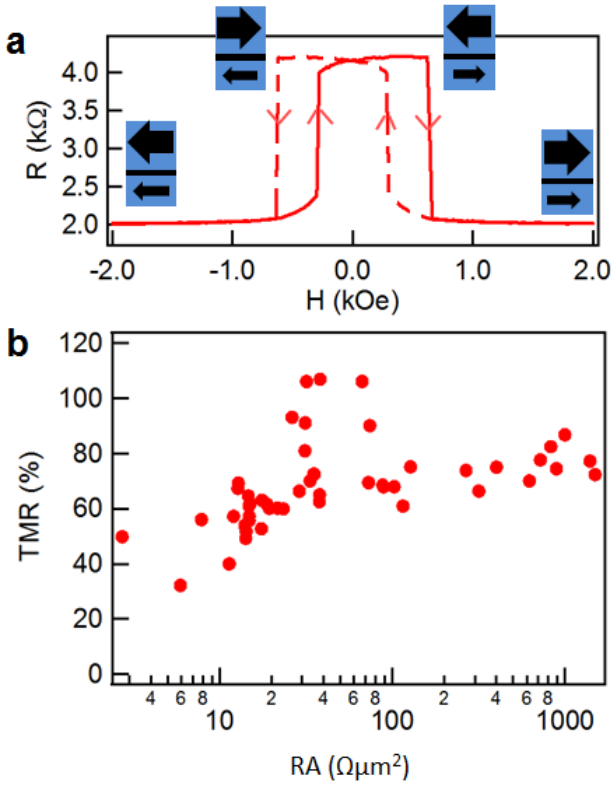

Figure 2.15: Magnetoresistance data from a wafer of 3x5 micron junctions patterned from the stack Ta(30)/[CuN(200)/Ta(30)]$_2$/Cu(20)/[Co(4)/Ni(8)]$_2$/$Fe_{60}Co_{20}B_{20}$(11)/MgO(t)/$Fe_{60}Co_{20}B_{20}$(200)/ Ta(80)/Pt(300), where t varies across the wafer. (a) Resistance as a function of applied in-plane field for a device for which t=11-12Å. First a large negative field is applied, and that is slowly swept to zero and then to a large positive field (solid line). At maximum, the field is then swept in the opposite direction, from positive to negative (dashed line). The resulting curves are marked with red arrows that show the sweep direction. At large fields, positive or negative, the free layer and the fixed layer have parallel magnetization in the direction of the applied field. At small fields, the free layer is anti-parallel to the fixed layer, leading to a higher magnetoresistance. These configurations are shown with the blue arrows—the fixed layer is the thick arrow, and the free layer is the thin arrow. The difference in resistance between the parallel and antiparallel states gives a magnetoresistance of 106%. (b) A compilation of the magnetoresistances of many devices with different t. We can't measure t directly, but infer it from the resistance of the junction. In this figure, we plot the TMR of various devices against the product of their resistance times their patterned area. A is assumed to be $15\mu m^2$, while R and TMR are measured. RA is shown on a log scale, since the resistance across an insulating barrier scales exponentially with barrier thickness.

pointing in the direction of the applied field. As the applied field is slowly lessened, the first switching event occurs when the free layer reverses from parallel to anti-parallel. The second switching event occurs when the fixed layer also reverses. The location of these switching events tells us about the magnetic properties of our device: the strength of the closing field lines from one layer at the location of the other layer, which we denote H_{dipole}, and the coercivity of each layer, H_c. (Notationally, we define the strength of the closing field lines from the fixed layer at the location of the free layer to be H_{dipole}^{fixed} and vice versa.) Broadly, in magnetoresistance diagrams like this one, the applied field works to keep the two layers parallel, the dipole field tries to align the two layers anti-parallel, and the coercive field tries to maintain the status quo. Note that the coercive field isn't a true field, but rather an energy barrier between two opposite magnetization configurations. To be more mathematical, the first switching event occurs at $H_{dipole}^{fixed} - H_c^{free}$, as the applied field becomes smaller than the dipole field, and the second event occurs at $-H_{dipole}^{free} - H_c^{fixed}$, as the applied field again overwhelms the dipole field. In this case, we are not trying to measure H_{dipole} or H_c, but are primarily concerned with the resistances in the parallel and anti-parallel states. Substituting those resistances into the formula given in equation 2.4 gives the tunneling magnetoresistance (TMR) of the sample.

Initially, we weren't sure exactly how much MgO to deposit. From the literature, we knew that it should be about 1nm, but this value is very sensitive. If the MgO is just a little too thin, the TMR falls off quickly. (The mechanism behind the thickness dependence of the TMR is not well understood, although it is commonly observed. There is an excellent discussion of this phenomenon in [60].) On the other hand, the amount of voltage one must apply to reach the critical current increases sharply with the barrier thickness. High

voltage reduces TMR, and high enough voltage will break down the oxide barrier. So getting this balance exactly right is important. To find the optimal point, we needed to measure TMR for barriers of varying thicknesses. To do this, we fabricated a wafer with the stack Ta(30)/[CuN(200)/Ta(30)]$_2$/Cu(20)/ [Co(4)/Ni(8)]$_2$/$Fe_{60}Co_{20}B_{20}$(11)/MgO(t) / $Fe_{60}Co_{20}B_{20}$(200)/ Ta(80)/Pt(300), where t is a variable thickness across the wafer. We accomplished this by simply turning off the wafer rotation before depositing the MgO. Because the MgO gun is off center in the AJA sputter system, this created a "wedge" of MgO, where the edge thicknesses differed by about $\pm$40% from the center thickness. Then, we patterned this wafer into micron-sized devices; by measuring devices across the wafer, we could measure the TMR across a range of MgO thicknesses. The results of this measurement are shown in figure 2.15(b). In this particular sample, the TMR seems to peak and then decrease as we use more MgO. This is not what one expects: one expects TMR to increase monotonically with MgO thickness and then level off[60][28], and monotonic increase is what we observe with most wafers. So although we can't explain why the TMR decreases here, we suspect that it is not physically significant. For example, there could be some deposition non-uniformity across the wafer which is causing the devices in the wafer center to behave better than those at the edges. The more important result from this graph is that we have a maximum TMR of 106%, which compares favorably to the literature, and that it occurs at an RA value of 30 $\Omega\mu m^2$. Comparing this resistance value to other samples with known amounts of MgO, we infer that this sample corresponds to 11-12 Å of MgO.

2.5.4 Crystallographic and Magnetic Characterization of Co/Ni Free Layers

The measurement of 106% TMR shown in figure 2.15 was a significant accomplishment for us for another reason as well. One of the main questions of this project was whether it would be possible to get a large TMR in a device stack that incorporates Co/Ni multilayers. Previous work had shown that one could incorporate Co/Ni into spin valves to reduce the demag field [23] [25]. But going from a spin valve (a device with a copper spacer between the two magnetic layers) to a tunnel junction (a device with an MgO barrier between the two magnetic layers) introduces unique crystalline matching problems. Specifically, high TMR junctions in the literature have free and fixed layers that are made Fe or FeCoB crystallized in a bcc geometry with the (001) in the normal direction [27][28], sandwiching an MgO layer that is also (001) oriented in the normal direction. At the interface, the [110] direction of the bcc-electrode corresponds with the [100] direction of the MgO. This provides good band matching with the MgO[61][62]. But Co/Ni films, in order to have high perpendicular magnetic anisotropy, need to be fcc with (111) orientation. Given this completely different crystalline structure, we weren't sure if or how we could have both good Co/Ni films and high TMR in the same device.

Initial attempts to put MgO directly on top of Co/Ni films, which is the easiest thing to do, did not give high TMR, as expected. However, by introducing a bit of FeCoB on top of the Co/Ni, we hoped to create a transition area where the crystallization could switch from fcc-(111) to bcc-(001). (Note that when a single crystal direction is listed, it is the axis normal to the film.) To assess how this was working, we measured the crystalline structure of our films with scanning transmission electron microscopy (STEM), electron energy loss spectroscopy (EELS), and x-ray diffraction (XRD). The STEM image, shown in figure 2.16 shows how

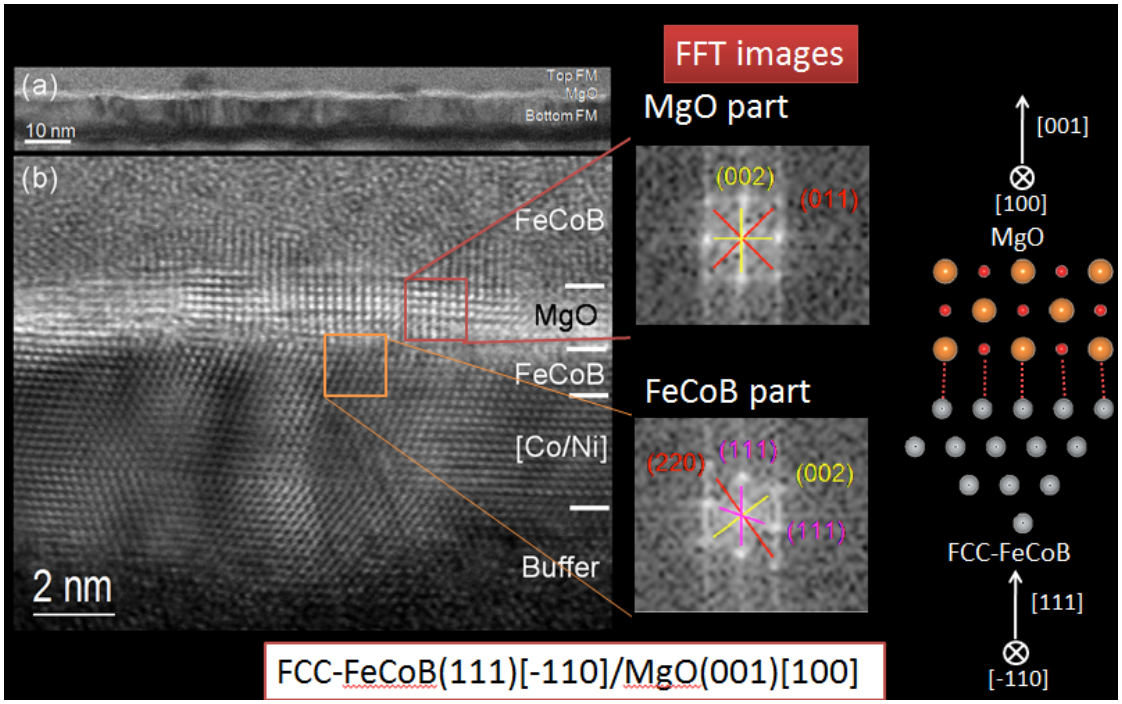

Figure 2.16: Scanning transmission electron microscope image of the same sample measured in figure 2.15 above. Diffraction images (labeled FFT), also taken in the TEM, are shown on the right. These images, which essentially show the Fourier transform of the crystal structure, give the crystal orientation and spacing from the position and distance of the peaks from the center. Both atom-resolution image and the diffraction pattern show that the vertical axes of the bottom FeCoB and the MgO are fcc-(111) and (001) respectively, at least in the center of the sample. The crystalline model that best fits the data shown is one in which the [100] axis of the MgO lines up with the [-110] axis of the fcc-FeCoB, and that these axes are oriented out of the page. This model is shown on the far right. Thanks to Pinshane Huang for these TEM images.

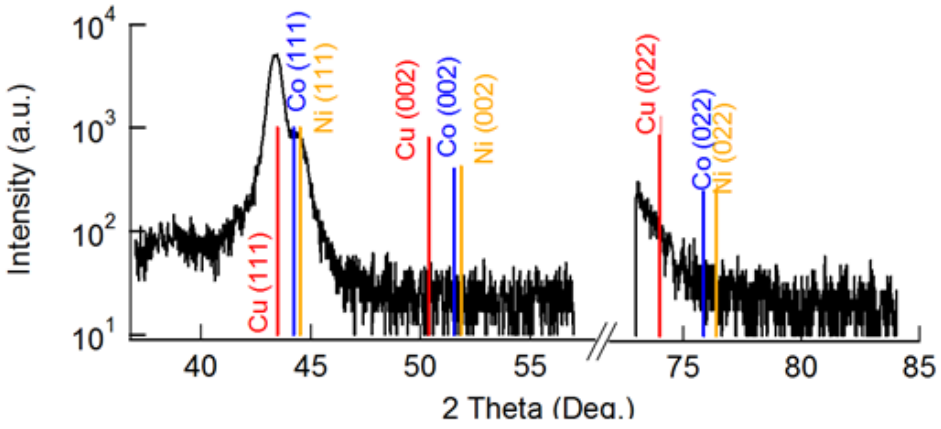

Figure 2.17: X-ray diffraction image of Ta(30)/[CuN(200)/Ta(30)]$_2$/Cu(20)/[Co(4)/Ni(8)]$_2$/$Fe_{60}Co_{20}B_{20}$(11)/Cu(300). The horizontal axis of the graph shows the angle difference between the incoming x-rays and the x-ray detector, and the y-axis is the scattered intensity. Various crystalline peaks are marked. Thanks to Takahiro Moriyama and Jonathan Shu for this image.

this worked out. Although the crystallization is uneven, at the center of the image, we clearly see fcc-(111) crystallization in the Co/Ni, and this seems to extend upward into the FeCoB. The MgO is (001) crystallized, with dislocations evident at the interface. The [100] axis of the MgO, which normally matches with the [110] axis of the bcc-FeCoB here seems to have aligned with the [-110] axis of the fcc-FeCoB. By measuring the peak spacing in the Fourier transform, we calculate that the MgO is about 3% compressed in the (001) direction. This is slightly higher than the 2% compression reported by Parkin[27], but slightly lower than the 5% compression reported by Yuasa[28]. There is some evidence that less compressed films give better TMR[29], but we are at least in the same regime as other authors, despite the introduction of Co/Ni. The top electrode, while mostly amorphous, does seem to have crystallized to the usual bcc (001) orientation for at least a few layers, enough for band matching with the MgO barrier[63].

We did an x-ray diffraction measurement of the free layer structure on the smoothing layer, without MgO or a top electrode. That data is shown in figure

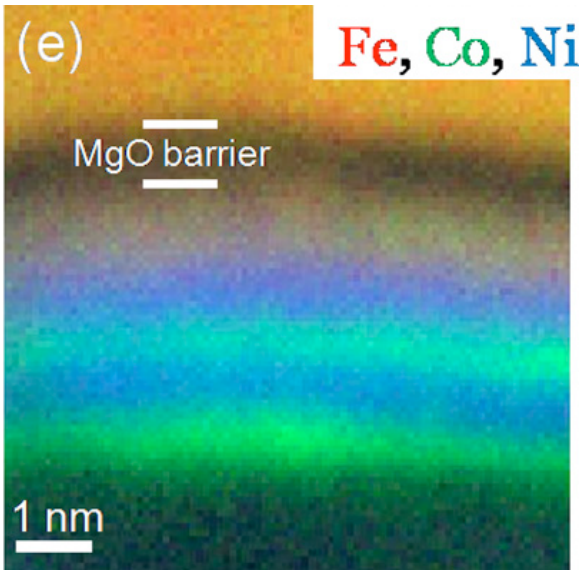

Figure 2.18: An EELS image of the TEM sample shown in figure 2.16. The colors shown correspond to different atomic composition. Thanks to Pinshane Huang for this image.

2.17. Although the signal of interest is a small rider on the Cu(111) signal, it seems that the Co and Ni are (111) oriented. They show no evidence of (001) orientation. This reinforces the conclusion from the TEM image, that the free layer is (111) oriented.

From these data points, we conclude that we have been mostly successful in fabricating a device with the crystal orientation we wanted. We do have both (001) MgO and fcc-(111) Co/Ni, and they coexist in the same stack, which is most important. We do not have a bcc-(001) FeCoB bottom electrode, as most other authors do, instead we have fcc-(111) FeCoB electrode. This might contribute to low TMR, as we do not have the expected band matching, but we still measure a TMR of 106%, which is a reasonably strong signal.

During the TEM measurement, we also did electron energy loss spectroscopy (EELS)[64]. This technique is used to determine the atomic composition of the sample. This works as follows: when the high energy electrons from the beam strike the sample, they can knock out one of the inner shell electrons of an atom

in the sample. The amount of energy lost during this collision can be used to determine the kind of atom in the sample. This technique gave the map shown in figure 2.18. This is of interest because it shows clearly that the Co and Ni films, despite being only a few atomic layers thick, are quite distinct. One could argue that the films are so thin that we effectively have a Co/Ni alloy, and that especially during anneal, the films mix completely. But this image shows that this is not the case, as we can clearly distinguish the Co and Ni films from one another.

Concerns about crystal matching drove us to combine FeCoB with Co/Ni in the free layer, as discussed above, but we haven't yet discussed the exact design parameters of the electrodes. The top FeCoB needed to be significantly thicker than the bottom electrode thickness in order to increase its coercivity, but there was likely a large tolerance in this value. The bottom FeCoB thickness was chosen much more carefully. We made micron junctions out of some wafers of the form [smoothing]/ $[Co(4)/Ni(8)]_2$/FeCoB(t)/MgO(11)/ FeCoB(200)/ Ta(80)/Pt(300), where the bottom FeCoB was a wedge of varying thickness over the wafer, and we found that the minimum amount of FeCoB we could have without reducing the TMR significantly was about 11Å. We wanted to stay close to this minimum level because shape anisotropy (which opposes the perpendicular magnetic anisotropy) scales linearly with electrode thickness.

The Co/Ni layer stack was chosen to partially cancel the demag field but leave the sample with in-plane equilibrium magnetization. As shown in figure 2.19, this worked very well. We reduced the demagnetization field from $M_S \approx 13000$ Oe to $M_S \approx 2000$ Oe. It would be nice if we could say that we carefully dialed in this exact demagnetization energy from the surface anisotropy energy value that we derived by VSM and FMR. In reality, the model we have is far too simple to explain this layer stack. This stack, [smoothing layers ending in Cu]/

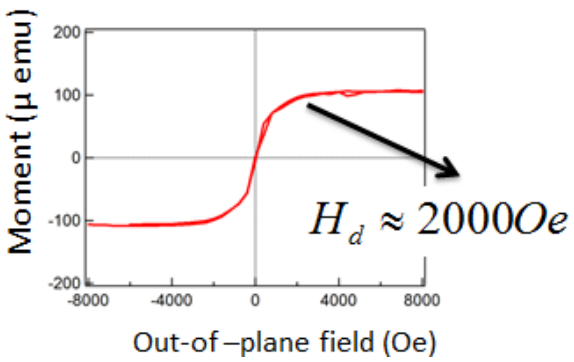

Figure 2.19: SQUID measurements of the magnetization of the free layer stack,[smoothing]/[Co(4)/Ni(8)]$_2$/FeCoB(11)/Cu(30) as a function of applied field. Although this measurement was taken with SQUID instead of VSM, the interpretation of the data is basically the same: the hard axis saturation point is equal to the demagnetization field for the sample. Measurements were taken in a Quantum Design MPMS-XL SQUID at 300K. Image courtesy of Takahiro Moriyama.

[Co(4)/Ni(8)]$_2$/FeCoB(11)/Cu(30), has 1 Cu-Co interface, 3 Co-Ni interfaces, 1 Ni-FeCoB interface, and 1 FeCoB-Cu interface. If we assume that all of them have surface anisotropy of 0.26 mJ/m^2, the value derived for Co/Ni interfaces from VSM, we expect demag field to be 4400 Oe. This is not near the measured value of 2000 Oe. This means that the simplest assumptions are not acceptable.

The literature suggests several possible explanations for this discrepancy. First, assuming that all the interfaces have the same anisotropy is probably not a good assumption. In particular, it seems that the perpendicular magnetic anisotropy of ferromagnet(FM)/nonmagnetic metal(M) interfaces is higher than that of FM/FM interfaces. This makes some intuitive sense in the context of the Néel model[30] of surface anisotropy, which calculates the anisotropy as a sum of non-symmetric pairs of atoms on the surface: FM-M pairs are even more non-symmetric than mismatched FM-FM pairs. The surface anisotropy of some FM/NM interfaces, from the literature, are as follows: for Fe, $E_S = 0.9$ mJ/m^2[31]; for Co, $E_S = 0.65$ mJ/m^2[65]; for Ni, $E_S = 0.8$ mJ/m^2[21]. In a more recent example (published after our work was done), Ohno's group[66] made an FeCoB layer with a FeCoB-

MgO interface and a FeCoB-Ta interface, and found a combined value of $E_S = 1.3$ mJ/m^2 for these two interfaces. All of these values are considerably higher than the $E_S = 0.26$ mJ/m^2 we calculated for Co/Ni. Second, I assumed that the saturation magnetization values for each material come from the bulk values. (I estimated the M_S for FeCoB to be about 2T.) There is evidence to suggest that M_S is suppressed in thin films [[21] p639]. This effect could be up to 20%, which seems like it wouldn't explain our discrepancy, but one has to remember that we're subtracting two large values (shape demagnetization field $\approx$ 13000 Oe and PMA $\approx$ 11000 Oe, see equation 2.6) to get the small H_d, so even a 12% error in M_{tot} could explain the entire discrepency. Finally, this stack will have a magnetoelastic anisotropy energy for which I haven't accounted. When magnetic films are strained, there is an energy term which depends on both the amount of strain and the direction of magnetization, a strain-induced perpendicular magnetic anisotropy. This term is significant in magntiude for both Co and Ni. In Co it is equivalent to a -2200 Oe change in demag field for a 1% strain. In Ni, the demag field is augmented by 2600 Oe for a 1% strain. (These values come from bulk measurements in the literature[21]. There is evidence that the magnetoelastic constants for thin films[67] might be significantly different from the bulk, which just further complicates the picture.) We did not measure the strain of our films. We would need to tease out each of these factors more carefully before we could truly dial in a desired PMA. Nonetheless, by trial and error we were able to find a Co/Ni/FeCoB combination that significantly reduced the demag field and still had good TMR, which was the goal of this line of experimentation.

2.6 Fabrication and Measurement of Nanometer-Sized Co/Ni Magnetic Tunnel Junctions

With the material stack decided and characterized, we next moved to fabricate a single MRAM bit, more colloquially referred to as a nanopillar. While we were able to get TMR from micron junctions, we can only switch micron junctions with field. To use spin torque current to switch a structure, we have to take it down to the nanometer level. As this project was motivated by MRAM applications and the prospect of reducing the critical current for spin torque switching, demonstrating spin torque switching was the crucial final step in our project.

Going forward we will exclusively discuss a nanopillar made from the stack Ta(30)/[CuN(200)/Ta(30)]$_2$/Cu(20)/ [Co(4)/Ni(8)]$_2$/FeCoB(11)/MgO(t) / FeCoB(200)/ Ta(80)/Pt(300). This was the stack characterized above. Of course, this presentation is shaped by the desire to tell a cogent story in retrospect, and does not reflect the full range of samples fabricated and measured. Dozens of wafers with a variety of electrode compositions were fabricated at the micron level, including some with zero, one, or two perpendicularly magnetized electrodes. Many hundreds of magnetoresistance curves like that shown in 2.15 were gathered. Some of these devices were even patterned into nanopillars and measured. These other samples will not be presented here, as the nanopillars made from them were generally less able to be switched consistently with a low critical current. We will discuss our most successful devices below.

2.6.1 Fabrication of Nanopillars

We made elliptical nanopillars of various sizes and eccentricities, ranging from 100x100 nm^2 to 70x220 nm^2. Fabrication of the nanopillar followed the work of

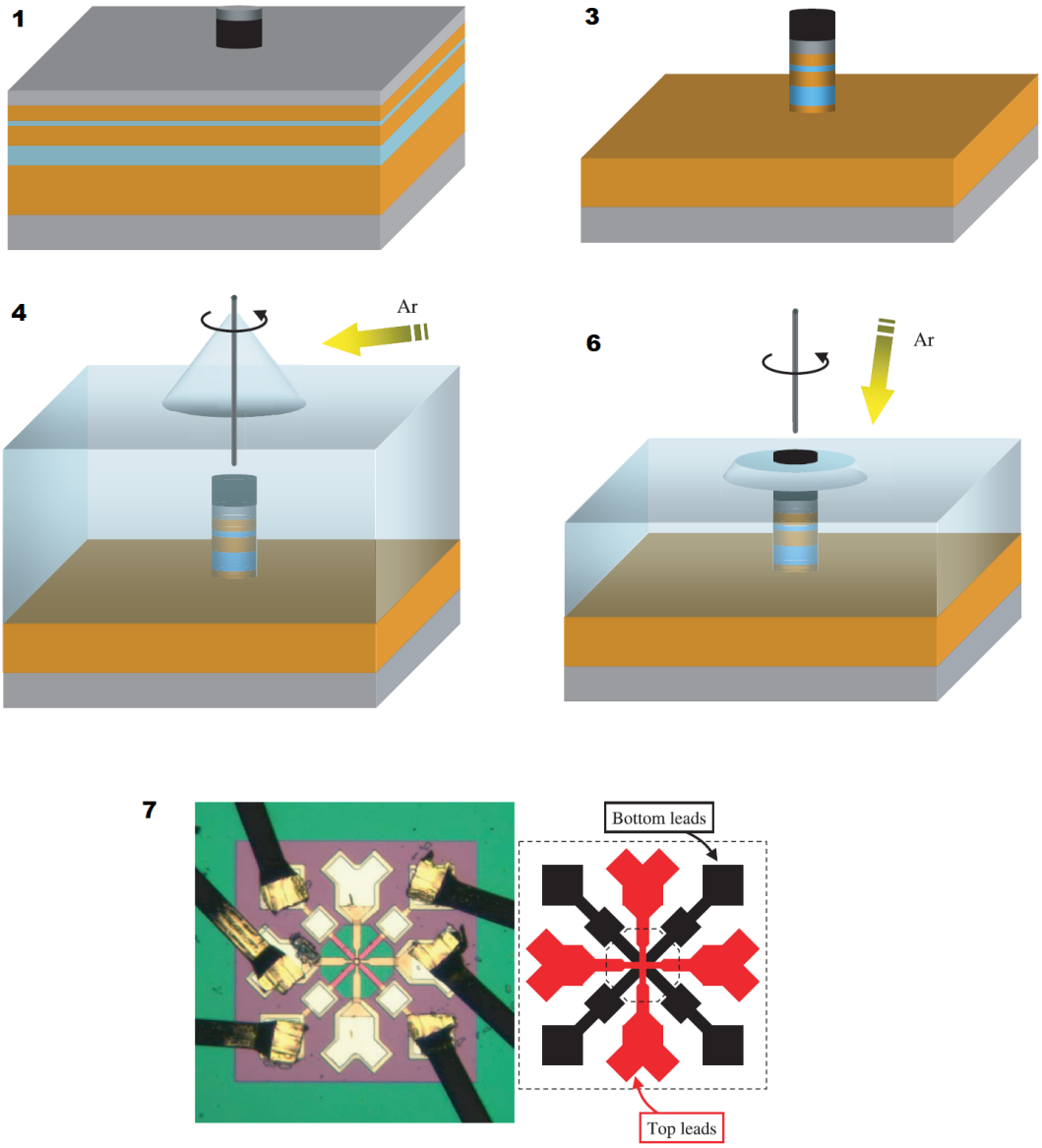

Figure 2.20: A cartoon overview of the nanopillar fabrication process, with numbers corresponding to the steps described in section 2.6. 1. A chrome-on-carbon mask is defined by e-beam lithography, lift-off, and oxygen plasma. 2. Not shown. 3. Nanopillar defined by ion milling. 4. PECVD oxide deposited and planarized. 5. Not shown. 6. The carbon cap is exposed by ion milling. 7. A finished device using this procedure and mask set. All pictures taken from [68].

previous Ralph and Buhrman group members completely, using their masks and their recipes in nearly every way. Nathan Emley's thesis is the best resource for this fabrication process[68]. His pictorial overview in chapter 3 is especially clear. The only thing that we did differently from Dr. Emley in fabricating our nanopillars was to use the newer tools available to us, especially the newer ion mill with a mass spectrometer on the exhaust port for end point detection; otherwise, the process was the same. For the sake of completeness, I will describe the steps we used broadly, in words below and pictorially in figure 2.20, with the understanding that an interested reader can refer to Dr. Emley's more thorough document. After sputter deposition of a multilayer stack, nanopillar fabrication followed these basic steps:

1. Pattern the nanopillar with e-beam lithography. We use a PMMA bilayer lift-off process to define the pillar in chrome. Chrome lifts off well but doesn't provide good ion mill resistance, so we put down carbon first and transfer the chrome pattern to carbon with oxygen plasma.
2. Define the bottom leads and pads with photolithography mask 1, and then ion mill away all of the unprotected material.
3. Protect the pads with photolithography mask 2, and then ion mill down to the smoothing layer. The carbon mask from step 1 protects the nanopillar, so this step defines the pillar.
4. Cover the nanopillar in protective oxide, planarize that oxide with a low-angle ion mill, and use photolithography mask 3 and HF to remove the oxide above the pads.
5. Add additional oxide in the area around the nanopillar (defined by mask 4), where the top leads will pass over the bottom leads, nominally to prevent possible shorts. This step was a legacy from when the process included a

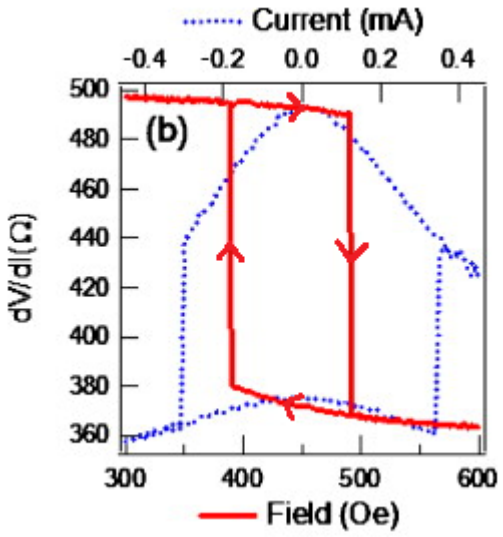

Figure 2.21: Differential resistance of a 220nm x 70nm nanopillar. The red curve shows resistance from two field sweeps, first decreasing from high field towards zero, and then increasing again, following the red arrows. The TMR, measured from the height of the switching event, is 38%. The blue curve shows resistance from current sweeps. Current measurements are taken with an applied external field of 460 Oe to cancel the dipole field from the fixed layer. The switching current for the AP $\rightarrow$ P is -0.31 mA, and switching current for P $\rightarrow$ AP is 0.35.

CMP thinning of the oxide, and was a response to shorts caused by the CMP[69]. It probably isn't necessary.

6. Protect everything but the nanopillar with photoresist (mask 5), and then expose the carbon mask that is still on top of the nanopillar by ion milling away the oxide above it.

7. Remove that carbon with oxygen plasma, and then connect the top of the nanopillar to the top contacts. This connection is made by defining the top leads with photolithography mask 6, depositing a thick layer of copper, and performing lift-off.

2.6.2 Current and Field Switching of Nanopillars

After fabrication, we measured the TMR of a number of devices. Measurements of the best device are shown in figure 2.21. First we swept field and measured magnetoresistance, shown as the red curve. This figure is similar to figure 2.15a, although we have zoomed in on a small section of the field range, and in this case, there is no fixed layer switching, only free layer switching. The switching events occur at $H_{dipole}^{fixed} \pm H_c^{free}$, so the dipole field from the fixed layer is 460 Oe, and the coercive field on the free layer is 52 Oe. We measure a TMR of 38%. This particular device was chosen from a wafer with a wedge of MgO, and this device was from a thinner section: here the resistance was 4.3 $\Omega\mu\text{m}^2$. We found it necessary to use a device with thinner MgO in order to achieve consistent spin-torque current switching, despite the reduction in TMR. Given this thickness of MgO, this TMR is consistent with what we measured with micron junctions.

Figure 2.21 is also a successful demonstration of spin-torque switching of the nanopillar. We clearly see two switching events, and the high and low resistance states seem similar to field switching. Interestingly, the shape of the current diagram is different from the field diagram. Under the macrospin model of switching, one would not expect this–one would expect a more rectangular graph. However, this is a very common feature of this kind of device. Many authors have observed that the TMR is somewhat suppressed as voltage increases. Sun and Ralph have an excellent discussion of the various mechanisms proposed to explain this phenomenon[60], including defect states in the insulating barrier, voltage dependence of the electronic properties of the electrodes, and increased magnon excitation at higher bias; however, the exact cause is not known.

In figure 2.21, we measure critical switching currents of 0.31 and 0.35 mA for AP $\rightarrow$ P and P $\rightarrow$ AP switching respectively. These values are actually critical

currents for thermally assisted switching. Switching occurs when the spin-torque from the critical current is enough to overcome the energy barrier, as described in equation 2.2. Thermal fluctuations can help get the magnetization up over this barrier even if the energy from the spin torque is slightly below the barrier height. To isolate the impact of thermal fluctuations from that of spin transfer torque, we calculate the "zero thermal fluctuation" switching current, that is, the amount of current it would take to switch the free layer without the thermal assist. Note that despite the name, all measurements here are occurring at room temperature. To measure this "zero thermal fluctuation" critical current, I_{c0}, we apply current pulses of various lengths. The longer the applied current pulse, the more likely a bit is to catch a large thermal fluctuation and make it over the energy barrier. Or, to look at the same physics slightly differently, the longer the pulse, the less current one needs to apply in order to make it over the barrier a fixed percentage of the time.

Thermally assisted switching as a function of pulse length is shown in figure 2.22a. In order to fit a line to this data, we derive a very simple theoretical model as follows. Define a given time interval, τ, as the time scale for which a thermal fluctuation of size ΔE will happen with a probability $e^{-\Delta E/k_B T}$. Note that we always assume T=300K. There could be local heating from the spin current itself, but we expect that effect to be small. We want to know the size of the energy barrier we can cross reliably in time t. By reliably, we mean with probability of success $1-e^{-f}$, where f is on the order of 5. So the reliable switching criterion can be written

$$\left(1-e^{-\Delta E/k_B T}\right)^{t/\tau} = e^{-f} \tag{2.17}$$

Now defining $\tau_0 = f\tau$ and assuming that τ_0/t is small, we can solve for ΔE as

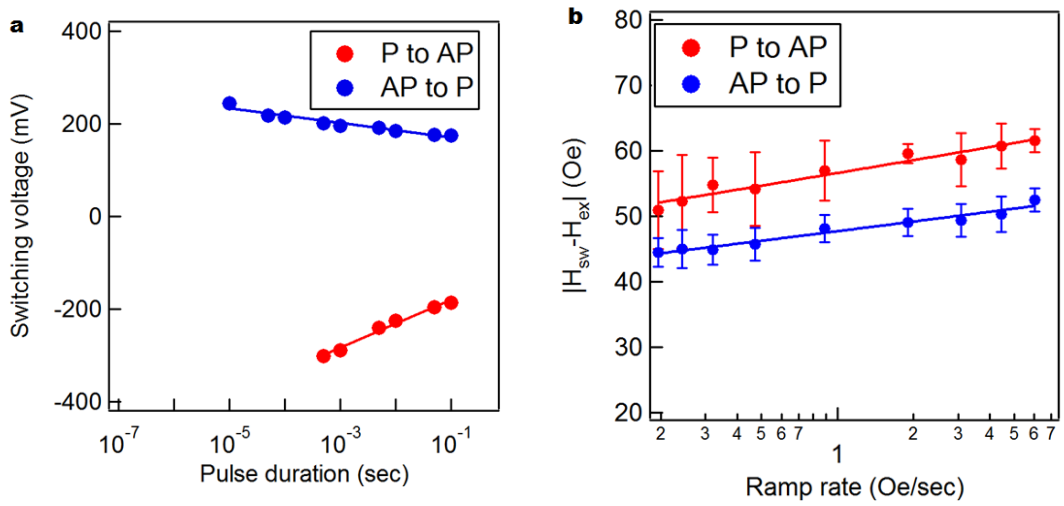

Figure 2.22: (a) Switching voltage for the 220 nm x 70 nm nanopillar as a function of the length of the applied pulse. Here, voltage was applied and measured, although we refer to this value in text as the switching current. Dividing through by the resistance (before switching) converts one to the other. Before applying the current pulse, a 460 Oersted external field was applied to cancel the dipole field from the fixed layer measured in figure 2.21. To find these points, numerous pulses of various voltages were applied, and the transition point above which switching occurred is highlighted. No statistics were taken to determine the probability of switching. (b) Switching field as a function of ramp rate. Note that the switching field measured is on top of the 460 Oe external field necessary to cancel the dipole field from the fixed layer. As in (a), no statistics were taken: these points mark the switching transition in a single field sweep. Uncertainty bars reflect intermediate resistance states for which it is unclear if switching has occurred. In both cases, switching was determined by magnetoresistance. Image courtesy of Takahiro Moriyama.

follows:

$$\Delta E = k_B T \ln(t/\tau_0) \tag{2.18}$$

Now let us consider the effect of spin-torque current. Spin torque will reduce the height of the barrier, as every electron gives the magnetization a small kick towards switching. (Imagine a volleyball that has to go over a net of a fixed height. Increasing the frequency with which you give it small bumps on the bottom will cause the ball to sit, on average, higher in the air, and reduce the remaining distance the ball has to go to get over the net.) Note that this theoretical model, that is treating the spin torque as a reduction of the barrier height, was not initially well accepted[70], but seems to now be accepted in the theory literature[71][72]. In this case, we can write $\Delta E = E_a(1 - I_c/I_{c0})$, where E_a is the height of the full energy barrier, I_c is the current applied, and I_{c0} is the applied current necessary to go over E_a, that is, without help from thermal fluctuations. So the measured critical current is given theoretically by

$$I_c = I_{c0}\left(1 - \frac{k_B T}{E_a}\ln(t/\tau_0)\right) \tag{2.19}$$

In the literature, it is common to assume that $\tau_0 = 1$ ns [73][66][17], on the grounds that this is roughly the inverse of the ferromagnetic resonance frequency, but this justification seems weak to me, and I consider this value to be arbitrary. However, it turns out that E_a and I_{c0} are not very sensitive to changes in τ_0: an order of magnitude change in τ_0 causes a 5% increase in I_{c0} and a 5% decrease in E_a. Using this value for τ_0, the data in figure 2.22a fit to this model gives the values shown in table 2.1.

We will analyze these results further, but before we do, suppose that in addition to measuring the "zero thermal fluctuation" switching current, we want to make a similar measurement of the switching field. The switching field measured in figure 2.21 is also assisted by thermal energy. (Note that "switching field" is the

	P → AP		AP → P	
	Current pulse	Field ramp	Current pulse	Field ramp
I_{c0} (mA)/H_{c0} (Oe)	$1.60 \pm .06$	107 ± 8	$0.60 \pm .02$	92 ± 5
E_a (eV)	$0.68 \pm .02$	$1.13 \pm .11$	$1.12 \pm .07$	$1.12 \pm .09$

Table 2.1: Calculated parameters describing the switching events shown in figure 2.22. Uncertainties shown come from the measurements and fits.

same as coercive field—I wrote it as H_c^{free} above.) To measure the "zero thermal fluctuation" switching field, we need to apply the field in a time dependent way. It is harder experimentally to send the field as a short pulse, but it is not difficult to ramp up the field at various rates, as we have done in figure 2.22b. Lowering the energy barrier at a steady rate over time instead of in a pulse changes equation 2.17 to become

$$\prod_{t_0=1}^{t/\tau} \left(1 - e^{-\Delta E(t_0)/k_B T}\right) = e^{-f} \tag{2.20}$$

where $\Delta E(t) = E_a(1 - R_H t/H_{c0})$, with R_H as the ramp rate of the field and H_{c0} the "zero thermal fluctuation" field in analog to I_{c0} above. t is the time over which the field ramps up before the field will switch with probability $1 - e^{-f}$, so the "switching field" is given by $H_c = R_H t$. Taking the log of both sides of equation 2.20, approximating $\ln(1 - e^{-x}) \approx -e^{-x}$, converting the sum to an integral, and assuming $\exp(\frac{E_a}{k_B T}\frac{H_c}{H_{c0}}) \gg 1$ (true for the relevant numbers), allows us to solve for H_c:

$$H_c = H_0 \ln R_H + H_{c0} + H_0 \ln \tau_0 - H_0 \ln H_0 \tag{2.21}$$

where $H_0 \equiv H_{c0} k_B T / E_a$.[3] From the lines fit to the data in figure 2.22b, this equation gives the values for H_{c0} and E_a shown in table 2.1.

We should note that in addition to the measurement error listed and the potentially significant error introduced by the arbitrary value of τ_0, there is also

[3]Note that it is typical in the literature[25][26][56] to use a different model to find H_{c0}. That model[74] was originally intended to describe a collection of iron oxide particles in recording media, and it doesn't fit the single-domain case as well, in my opinion.

potential for systematic error in the 460 Oe field applied to cancel the dipole field from the fixed layer. If the field from the fixed layer is not exactly 460 Oe, and is perhaps off by 5 Oe because of bad measurement, miscalculation, or uneven coercivitiy between P→AP and AP→P switching, this could affect the critical currents significantly. It might also explain the discrepancy between H_{c0} for P→AP and AP→P, which we nominally expect to be the same.

2.6.3 Analysis of Switching Measurements of Nanopillars

To analyze the measured values of critical current, switching field, and energy barrier, we can compare the measured values to what we expect from theory. First I will relate E_a and H_{c0} to one another. Then I will show what values we expect be from first principles. Finally, I will discuss the critical current in some detail.

In the macrospin model, all of the values in table 2.1 can be predicted from theory very simply: the theoretical relationships between these variables are summarized in the appendix in table A.1. What we have been calling the energy barrier, E_a, should be the same as the in-plane anisotropy energy defined earlier, E_u. So we expect that the energy barrier and the switching field should be related by the expression $E_a = (1/2)\mu_0 H_{c0} M_S V$. If we average the P→AP and AP→P values to get $H_{c0} = 100$ Oe, we calculate that $E_a = 1.4$ eV,[4] which is relatively close to the measured E_a of 1.1 eV. Recall that E_a depends on the made-up τ_0, which introduces an error on the order of 10s of %. This discrepancy could also suggest some supression in M_S, which seems likely, as discussed in section 2.5.4 above. The volume is also somewhat uncertain, as I don't have exact measurements of this bit.

[4]In this section, I am assuming a 200 nm x 60 nm x 3.5 nm magnetic free layer to account for some process bias. I am using $M_S = 1.32$ T, a linear combination of the bulk M_S values for the materials in the stack.

Next, we compare E_a and H_{c0} to values calculated from first principles. The source of the energy barrier we've measured is the shape anisotropy, so we expect $H_{c0} = M_s(N_y - N_x)$ and $E_u = (1/2)\mu_0 M_s^2 V(N_y - N_x)$. From [16], I calculate $N_y = .048$ and $N_x = .009$. These values are only accurate to within about 20%. The calculation is computationally intensive, and different approximation methods give slightly varying answers. Also, my estimate for the size of the pillar could be slightly wrong due to unknown etch bias and pillar taper. Using these demagnetization values, I calculate $H_{c0} = 510$ Oe and $E_u = 7.1$ eV. These values are a factor of 5 away from what we measured. Despite all the sources of error discussed, I expect a discrepancy on the order of 10s of %, not 100s of %. It's not immediately clear why there should be such a large discrepency here. It seems likely that some aspect of the simplest model is wrong; we theorize that the macrospin model doesn't apply.

To test this hypothesis, Dr. Moriyama did a micromagnetic simulation of our device with Object Oriented MicroMagnetic Framework (OOMMF) code from ITL/NIST[75]. He found that the switching events, far from following the macrospin model, were much more complicated. His simulation results are shown in figure 2.23. In the P→AP case, a domain wall seems to nucleate in the middle of the device and propagate outward, while in the AP→P case, the dynamics simply appear chaotic. With this more complicated switching mechanism, it seems reasonable that the relationships derived from the macrospin model do not apply.

Without the macrospin model, the expression for switching current given in equation 2.2 also can't be applied quantitatively to our device. Even if the macrospin model applied, the expression for critical current given in equation 2.2 depends on $\eta(\theta)$, which is an "efficiency" factor. $\eta(\theta)$ depends on the polarization of the switching current and the angle θ between the free and fixed layers. It is also

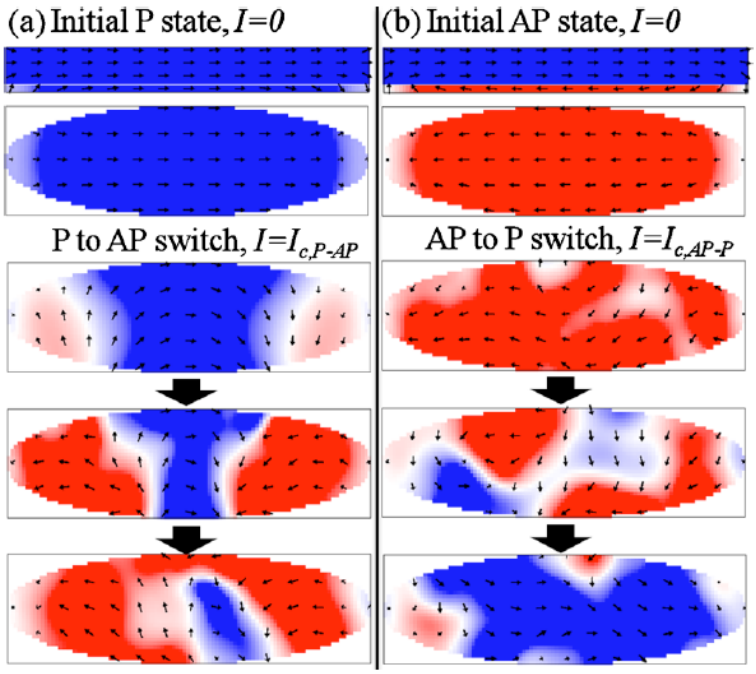

Figure 2.23: Individual spins in a 70x220 nm^2 nanopillar modeled with OOMMF during switching from P→AP (a) and AP→P (b). For both columns, the top two pictures are the initial state. The top picture is a side view of the nanomagnet, both the thicker fixed layer on top and the thiner free layer on the bottom. The second picture is a top view of the nanomagnet. The colors correspond to the degree of magnetization along the major axis of the ellipse. Canting is evident at the edges of both equilibrium states. Pictures 3 through 5 in each column correspond to snapshots taken during the dynamic switching process under a spin torque current. Both switching processes are clearly non-uniform. Image courtesy of Takahiro Moriyama.

highly dependent on the materials system. We could guess at η based on values from the literature, but given that we know that the macrospin model doesn't apply, it doesn't seem worthwhile. However, one aspect of our critical current measurement, the fact that $I_{c0}^{P\to AP} > I_{c0}^{AP\to P}$, is well explained by theory. Authors in the literature, both theory[60][76] and experiment[23], agree that $\eta(\theta)$ is larger for $\theta = 0^o$ than $\theta = 180^o$, although usually by less than a factor of two. The mechanism for this asymmetry mentioned by Stiles is the spin-dependent scattering from the bottom surface of the free layer when switching by reflection (P→AP) instead of transmission (AP→P). This is reassuring, although our asymmetry is significantly larger than what is typically observed. This could be a miscalibration of the dipole-canceling field, or it could be a symptom of the more complicated, non-uniform switching dynamics discussed above. I don't have an easy explanation for why $E_a^{P\to AP}$ is so low for the current pulse, but these two results may be related, as the calculation of I_c and E_a from the data are not independent.

One might ask, at this juncture, why we did not measure a smaller bit than the 220nm x 70nm bit presented here, given the breakdown of the macrospin model in switching. But, in fact, the 100nm round nanopillars that we measured were even more non-uniform. This bit at least shows clean switching: in figure 2.21, we see two distinct states with sharp switching between them. But in many other bits with less eccentricity, we saw a variety of intermediate resistance states indicating the nucleation of a domain wall and partial switching of the bit[77]. In theory, we could have made the bit smaller while maintaining high eccentricity, but we simply didn't take the time to optimize the e-beam process. This would be a productive avenue of further work. However, there is evidence that domain wall size is an order of magnitude smaller in thin films with high perpendicular magnetic anisotropy. (Compare, for example, the 10nm DWs in [78] with the 100+ nm DWs in [11].) So

intermediate states and non-uniform switching are likely to plague perpendicularly magnetized nanopillars even below 100nm sizes[77].

How can we assess whether we have reached our goal of reducing the critical current with the introduction of Co/Ni layers? Ideally, it would be nice to compare our device containing a $[Co(4)/Ni(8)]_2$/FeCoB(11) free layer with some sort of control, perhaps a similar device containing a [Co(8)/Ni(16)]/FeCoB(11) free layer [23]. In fact, we thought of doing this, and even sputtered the appropriate metal stacks, but due to the large amount of time for fabricating nanopillars, we never got that far. We must content ourselves, then, to simply compare our "zero thermal fluctuation" spin current to that of other devices in the literature. Actually, we will compare the critical current density, $J_{c0} = I_{c0}/A$, in order to fairly compare devices of different areas. We observed P→AP switching at 5.0×10^6 A/cm^2 and P→AP switching at 13×10^6 A/cm^2. Other results from the literature are shown in table 2.2. The best device for comparison might be one made by Ikeda et al.[17] with an FeCoB free layer of 4 nm. Ohno's group is arguably the world leader in making high quality, research grade TMR devices[29], and that particular device is chosen because the free layer thickness is similar to ours. Admittedly, the saturation magnetization of FeCoB is higher than that in our device, but only by a third. That device had critical current of 2.0×10^7 A/cm^2, which suggests that we have somewhat reduced the critical current with perpendicular magnetic anisotropy, as we hoped. However, looking at table 2.2 more broadly, we see that on average, our critical switching current is not significantly lower than others in the literature. Our value for P→AP switching is promising, but our value for AP→P is quite high.

Our large switching current probably comes at least partially from our large free layer thickness. We know from figure 2.19 that the Co/Ni multilayers reduced the

Author	TMR	Average J_{c0} ($A/cm^2 \times 10^6$)	Free Layer Material	Free Layer Thickness (nm)
Ikeda[17]	80%	7.6	FeCoB	2.2
Ikeda[17]	80%	20	FeCoB	4.0
Nakayama[26]	10%	4.7*	TbCoFe/FeCoB	4.0
Mangin[25]	GMR	14	Co/Ni	4.5
Liu[23]	GMR	2	Co/Ni	3.2
This work	38%	9	Co/Ni / FeCoB	3.5
Ikeda[66]	120%	3.9	FeCoB	1.0

Table 2.2: Comparison of figures of merit across a variety of devices in the literature. Every device has slightly different material stacks, of course, so direct comparisons should be made carefully. The first two entries should be considered references for solidly made TMR nanopillars with no attempt to cancel the demagnetization field. The other devices all involved some attempt at enhancing perpendicular magnetic anisotropy. This table includes two devices with Cu spacers instead of MgO spacers, marked "GMR". *Note that Nakayama's critical current was measured with a 100ns pulse, and is not a true J_{c0}.

demagnetization field, as we intended. That must have reduced the critical current somewhat. But we expect J_{c0} to scale with thickness of the free layer. (I_{c0} scales with volume. We have divided off the area in going from I_{c0} to J_{c0}, but not the thickness.) This is not just a quirk of the figure of merit that we have chosen, but a serious drawback of our devices. In order to solve the crystal matching problem, we combined Co/Ni multilayers with FeCoB, which worked well, but the resulting free layer is twice as thick as most others in the literature. With that said, we could have chosen a combination with thinner Co/Ni layers. The problem is that as the Co/Ni layers get thinner, the anisotropy goes up. So to hold the anisotropy constant, you need fewer layers, perhaps just one or two. Then the effect of the non-Co/Ni interfaces becomes larger than that of the Co/Ni interfaces, because there are so few Co/Ni interfaces.

The simplest solution is to do away with the Co/Ni altogether, as Ikeda and Ohno did in [66]. Ikeda and his colleagues simply used a very thin FeCoB layer, thinner than anyone else had made, so that the perpendicular anisotropy from the

top and bottom surfaces of the FeCoB layer dominate the shape anisotropy. Recall that the surface anisotropy from ferromagnet-nonmagnet interfaces is higher than that of ferromagnet-ferromagnet interfaces, so just these two surfaces were enough to reduce their demagnetization field from 15.8 kOe to 3.3 kOe. This solution is elegant. It's also difficult to do—in order to make a device that works well with such thin electrodes requires very clean, smooth devices. Note that Ikeda's paper was published after our work had been completed. When we read it, we immediately realized that they had accomplished all of our goals: they made a high TMR device that used surface perpendicular magnetic anisotropy to reduce the switching current while preserving low damping. What's more, their method was simpler and more elegant than ours. We rushed to publish whatever we had[56] and moved on to other projects.

2.7 Conclusions

In this study, we reached many of our goals. We characterized a variety of Co/Ni films with VSM, and a few films with FMR. We used that information to incorporate Co/Ni films into magnetic tunnel junctions. We found a way to combine Co/Ni films with FeCoB in order to preserve the high TMR from FeCoB/MgO/FeCoB junctions. We made devices with 106% TMR at maxiumum, and 38% at the sub-10 Ω um^2 resistance level necessary for spin torque switching. Incorporating Co/Ni into the free layer reduced the demagnetization field from 13000 Oe to 2000 Oe, while maintaining a low damping of only 0.015. As a consequence, we saw some reduction of the amount of current needed to switch a nanopillar compared to similar devices in the literature. Unfortunately, our device did not have a record-low critical current, likely due to the large volume of the free layer that resulted from combining Co/Ni multilayers with FeCoB.

If one were to continue to study Co/Ni films in the Ralph lab, one would want to begin by improving the material characterization. If one is to work with Co/Ni, one needs to be able to model the anisotropy well enough to confidently "dial-in" a given anisotropy from a particular material combination. To do this, one would need to start by improving the thin film characterization setups. Because of the noise in the VSM setup, we were never confident of the hard axis saturation point of the films we measured there, and thus never felt confident in our VSM measurements to better than about 25%. The FMR setup was also unacceptably noisy. Then one would need to characterize our Co/Ni films more carefully. Characterizing the exact saturation magnetization for each of our thin films, and how that M_S varies with layer thickness is important. Separating the effect of the outside surfaces, the FM/NM surfaces, from the interior FM/FM surfaces is also likely to make a big difference, and it wouldn't be hard to do. Strain and roughness are unknown wild cards: how strain and roughness vary across different recipes, from material to material, and how much they affect anisotropy and saturation magnetization are all crucial questions. One might dismiss these concerns as 10-20% effects, and therefore not terribly important. But one of the key problems with using Co/Ni thin films to tune anisotropy is that one must obtain a small value by subtracting two big values. In our device, we had a saturation magnetization of 13000 Oe and a total surface magnetic anisotropy of about 11000 Oe. We subtracted these two values to get H_d of 2000 Oe, which worked out well. But one can see the fundamental problem of trying to do precise engineering by subtracting two large numbers from one another—a small change in either number can lead to a big change in the final, net anisotropy.

One could also make changes on the device side. It seems likely that the device we tested was not switching in a uniform, macrospin way, which makes the

switching difficult to model. It would be nice to fabricate smaller devices, as these are more likely to have a single domain. This is not trivial, though. Edge effects—edge damage or oxidation, tapering, and spin canting—all become more important at smaller areas. The e-beam process would have to be tuned as well. Even with smaller devices, it seems possibly and even likely that domain wall switching will continue to be the dominant switching mechanism. In that case, crystalline defects and non-uniformities are even more important, as these sites pin domain walls and thereby increase the critical current necessary for switching. As figure 2.16 showed, our devices have a long way to go in expunging crystalline defects and improving uniformity. If one were going down this path, one could try to study the effects of growth and annealing on device quality more systematically.

On the measurement front, there were some mysteries that weren't resolved. The mismatch between P→AP and AP→P critical current and energy barrier were never fully understood. Was this a single device anomaly, a miscalibration of some kind, or a repeatable feature of this material system? If it was repeatable, what caused it? We also never came up with a satisfactory value for τ, and since the whole field uses the 1ns value, this could be an interesting line of experimentation.

However, for this application, my belief is that none of these efforts are worth the time. In retrospect, I think that Co/Ni films are not the best way to reduce the demagnetization field in MRAM bits. The crystalline matching problem will always be problematic. Our solution, a thin layer of CoFeB, was okay, but it may never be conducive to really good devices. From the point of view of maximizing TMR, the fcc-(111)[110] FeCoB we made worked reasonably well, but it doesn't seem to work as well as the usual bcc-(001)[-110] FeCoB. From the point of view of minimizing critical current, mashing together FeCoB and Co/Ni will always prevent us from having very thin electrodes. For these reasons, the thin FeCoB

devices demonstrated by Ikeda et al. seem to be the superior solution. These devices are not perfect, of course. Ikeda himself shows that damping increases as FeCoB thickness decreases, and the mechanism behind that is not well understood. Exploring that effect would be a productive course of research. Regardless, Ikeda's approach seems to be the most promising method of reducing critical current in MRAM devices in the future.

CHAPTER 3

COUPLING SUPERCONDUCTING MICROWAVE CAVITIES AND NANOMAGNETS

3.1 Introduction and Motivation

Nanomagnets, under usual conditions, have a resonant frequency in the gigahertz range. By applying oscillating magnetic fields at the same frequency, one can excite and study the nanomagnet dynamics. Microwave cavities with resonance frequencies in the gigahertz range are useful for amplifying microwave radiation signals. For that reason, ferromagnetic resonance (FMR) experiments have used microwave cavities for 50 years[80]. In this section, I propose to use a different type of microwave cavity, one made of superconductors, to interact with nanomagnets in various configurations. In all of the experiments proposed here, the cavity is made from coplanar waveguide, as shown conceptually in figure 3.1. The electric and magnetic fields propagate along the waveguide in the gap between the center signal line and the outer ground lines, and the breaks at the end of the waveguide act as "mirrors" which reflect photons back into the cavity. Recently, superconducting microwave cavities have been studied a great deal [81] [82] [83], not for use with ferromagnets, but for use as detectors in nanomechanical resonator studies[84][85] or for coupling to qubits based on Josephson junctions[86][79][87]. These cavities have a very large Q (up to $\approx 10^6$)[82], which makes it possible to use them to detect very small changes in systems. For this reason, studying the interaction of nanomagnets and superconducting microwave cavities seems like a promising avenue of research.

In this chapter, I will discuss a number of closely-related possible experiments that would combine superconducting microwave cavities (SMCs) with ferromag-

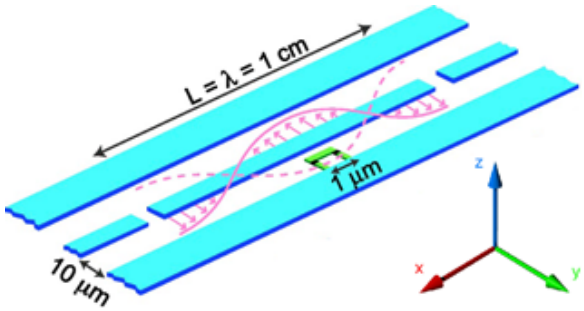

Figure 3.1: A cartoon of a microwave resonator of the coplanar waveguide variety, from [79]. A TEM wave propagates in the x direction. The gaps at the ends of the center stripline act like mirrors that reflect photons of the correct wavelength. The pink lines show the electric field. The magnetic field lines, not shown, circle around the stripline. This picture is a conceptual cartoon only; the exact lengths and geometry of our device are slightly different.

netic dynamics—a marriage that has never been explored, but offers a number of promising paths. In this introduction, I will propose several experiments that one might conduct with nanomagnets fabricated in SMCs to suggest that this is an interesting direction of study. Then in section 3.2, I will present some SMCs that I designed, fabricated, packaged, and measured. I believe that I fabricated the narrowest coplanar waveguide ever made. I never made it as far as integrating nanomagnets into the cavities. Finally, I will conclude with some thoughts on the promise and challenges of this project.

The first experiment that one might pursue with nanomagnets in SMCs is ferromagnetic resonance. In the previous chapter, FMR is detected by absorbance: the signal is (energy dissipated in nanomagnetic dynamics)/(energy dissipated in the cavity normally). The numerator is proportional to the volume of the nanomagnet, while the denominator is inversely proportional to the Q of the cavity. So a cavity with a higher Q can be used to study smaller magnets. Superconducting microwave cavities offer higher Q than traditional microwave cavities[80], which are in turn much more sensitive than the transmission lines used in flip-chip FMR experiments like the one used in the previous chapter. The advantage of a

transmission line is that it is broadband, while the cavity resonance is fixed by its geometry. But because the resonant frequency of the nanomagnet can be tuned by applying an external field, as we did in the previous chapter, this is not a significant limitation. Initial calculations suggested that FMR using a SMC would allow us to probe a magnet that has been patterned down to nanometer size—something impossible to imagine with either flip-chip FMR or traditional cavity FMR.[1] As discussed in chapter 2, FMR allows us to measure a magnet's magnetic anisotropy, damping, and saturation magnetization. As we discussed, these values may vary significantly from the bulk for thin films, and effects like edge-spin canting and antiferromagnetic edge oxides become more pronounced as one moves from extended films to patterned nanomagnets. Spin torque FMR is useful for studying these properties of nanomagnets when they are in stacks of other materials, but no method exists for studying them in isolation. This method is a very clean, simple, sensitive method of probing magnetic devices that have been patterned to nanometer sizes.

A second experiment one might pursue with this kind of device is making a microwave amplifier. To do so, one would replace the simple nanomagnet from the first experiment with a full tunnel junction, like those described in chapter 2. The input to such a device would be an AC voltage signal fed into the cavity. That AC signal would excite oscillations in the free layer. If we wire up both ends of the tunnel junction and put a DC current through the tunnel junction, those nanomagnetic oscillations will cause an AC response in the junction, $V_{AC} = I_{DC}\Delta R$. The

[1] In chapter 2, we measured magnetic resonance through cavity absorption, but this may not be the best detection method in this case. On resonance, the nanomagnet also changes the inductance of the cavity, which will shift the cavity's fundamental frequency. This may turn out to be the easier signal to detect. Using the axes of figure 2.6, the absorption signal depends on $\mathrm{Im}[m_x]$, while the inductance change depends on $\mathrm{Re}[m_y]$. $\mathrm{Im}[m_x]$ is about 15 times larger than $\mathrm{Re}[m_y]$ for appropriate parameters, since the magnetic oscillations are smaller out-of-plane than in-plane due to shape anisotropy. But the signal-to-noise ratio might be better for measuring changes in peak position than absorption. Initial measurement results, shown below, are not conclusive, so both detection methods are possible.

input signal would have to be at a single frequency, the resonant frequency of the nanomagnet, although low-frequency modulations of signal amplitude would be acceptable. Even if the input microwave signal is very small, it would be amplified by the high Q of the cavity, and can then be amplified further if I_{DC} is large.

There are several possible limitations to this method. First, because both ends of the nanomagnet need to be wired up, there will be a lot more normal metal in the cavity, and this metal will be lossy. This will decrease the Q of the cavity. Second, if I_{DC} is too large, it will create large Oersted fields that could cause the surrounding niobium to go normal. But this is manageable: if the leads pass within 30 nm of the niobium, one can have 30 mA of current, which is substantial. Third, depending on the thickness of the MgO tunnel barrier, the Joule heating could be quite large. This could cause problems, since the superconducting cavity have to be kept at low temperature. A tunnel junction with 1 kΩ resistance, a low but reasonable value, under 10 mA of current dissipates 100mW of power. If this exceeds the cooling power of the fridge, one could flow helium over the tunnel junction directly (in a dunker). Finally, and probably most importantly, this would be a single mode amplifier which had to operate at cryogenic temperatures, which limits potential applications. However, one could imagine applications in quantum information science where such an amplifier might find a use[88].

A third experiment is mode-locking nanomagnet oscillators. In the second experiment, we used the mode of the cavity to excite nanomagnetic oscillations. In this experiment, we propose to drive dynamics in the other direction—to use the oscillations of a nanomagnet to excite the resonant EM mode of the cavity. The nanomagnet would be the free layer of a MTJ, as in the previous example, and it could be excited to oscillate by an AC spin-torque current. These kinds of spin torque oscillators have been demonstrated in the literature [89], but they suffer

from phase slips and low quality factor. One could potentially use the narrow line width of the cavity to phase-lock the output signal from such a spin-torque-driven nanomagnet, thereby improving its Q. Alternatively, one could potentially fabricate a longer cavity with multiple magnetic antinodes, and couple multiple nanomagnets at the multiple antinodes of the cavity. MTJs have been used in the past as microwave signal generators, but they suffer from low output power. If multiple nanomagnets could be mode-locked in the same cavity, they could boost the overall signal.

A final experiment would be strongly coupling a magnet and a superconducting microwave cavity in the quantum mechanical sense. "Strong coupling" occurs between two quantum systems when the rate at which an excitation in either system will transfer to the other system, g, is much larger than the rate at which an excitation will decay in either system independently. This leads to a strong hybridization of the states of the two systems. Several groups have coupled large ensembles of paramagnetic spins to cavities[90][91], but at the time that this experiment was proposed, no one had hybridized the states of resonator with a ferromagnet. A theoretical proposal by Soykal and Flatté[92] suggested that this could be achieved. The system proposed in this section with a resonator and a nanomagnet probably couldn't reach the strong coupling limit: from the Dicke formalism[93], I estimate $g \approx 1$ MHz, while the ferromagnetic relaxation rate should be ≈ 30 MHz for a ferromagnet with damping of $\alpha = 0.01$ tuned to resonance at 3 GHz. However, it seemed likely that one could reach the strong coupling regime by using a much larger magnet, since the coupling depends on the percentage of the cavity mode that is filled with the magnet. This experiment was one of the motivations for this line of research. Interestingly, since this project was begun, the Goennenwein group[94] has done exactly this experiment, using a large yttrium iron garnet

sample on a very similar niobium CPW cavity. They measured $g/2\pi = 450$ MHz with a magnetic damping rate of $\gamma/2\pi = 50$ MHz and a resonator decay rate of $\kappa/2\pi = 3$ MHz, which shows strong coupling.

These experiments, taken together, suggest that there might be devices of interest that could be made by coupling nanomagnets with SMCs. With this goal in mind, I started designing an experiment to demonstrate the first, simplest goal: nanomagnet FMR in a superconducting microwave cavity.

3.2 Cavity and Package Design

For this project, I designed and fabricated a cavity made of niobium on a silicon chip. The chip is connected to a transmission line made of Arlon printed circuit board (PCB) in a small copper box. A photo of the whole package is shown in figure 3.2, and a schematic of the device is shown in figure 3.3. I will discuss the design of these components and the reasons behind those design decisions below.

The cavity is made of coplanar waveguide geometry: a center line with two ground planes on either side that sit in a single plane on top of a dielectric substrate. As Schuster[95] explains, there are a number of possible choices besides coplanar waveguide including microstrip (a center line without the two grounding lines), stripline (microstrip embedded in the center of a dielectric), and coplanar stripline (two grounded lines but no center line). These choices, while possible, are all unbalanced, and therefore require more complicated electronics to transfer the signal from the balanced coaxial lines. Coplanar waveguide is also advantageous because the impedance of the line depends only on the ratio of the center line width, s, and the gap width, w, and not on the absolute values. Thus the cavity can be enlarged in a proportional way by several orders of magnitude without ruining its properties.

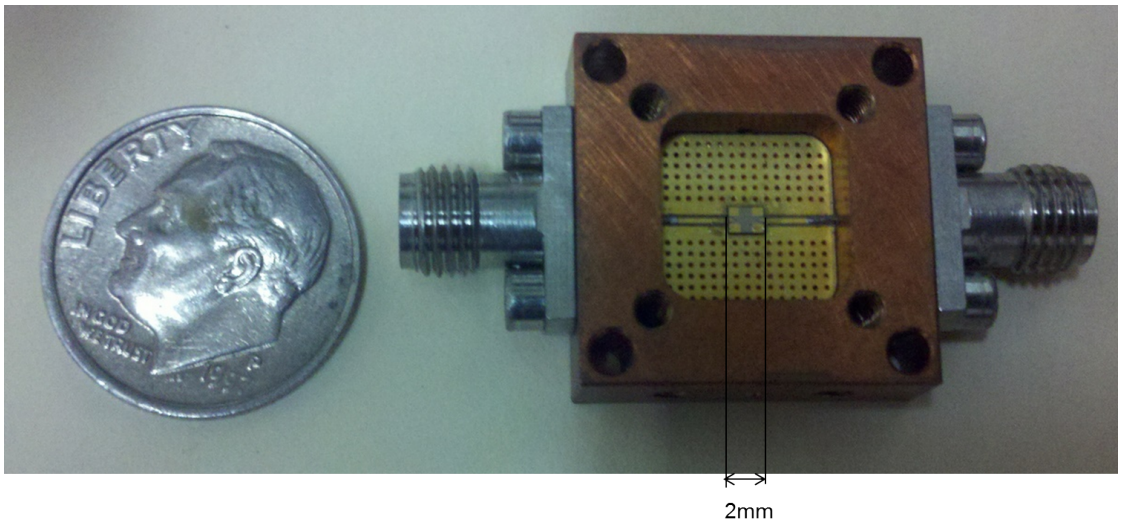

Figure 3.2: Chip and packaging for the superconducting microwave cavity. The copper sample box (brown) contains the perforated, gold-plated printed circuit board. The center line of the coplanar waveguide can be seen on the printed circuit board as a thin horizontal line, with the perforated ground planes above and below. In the center of the printed circuit board is the 2 mm x 1.5 mm silicon chip with the superconducting microwave cavity on it. (This particular chip had gold pads in each corner for easier bonding.) The two sets of holes on the box are for screwing down the copper, space-filling lid (not shown) and for mounting the box on the sample rod. The SMA connectors on either side of the box were off the shelf components ordered for this application from Southwest Microwave. Underneath the chip, not visible here, a size 00 through-hole was drilled in the bottom of the box so that damaged chips could be pushed out without removing the PCB. The dime is for size reference and is not an electrically significant component.

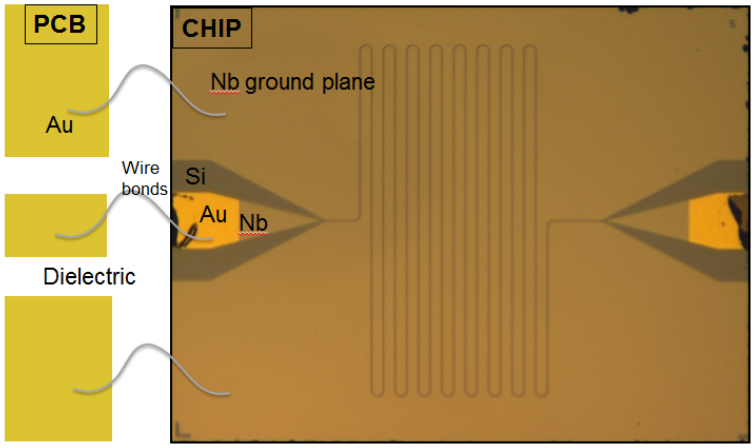

Figure 3.3: On the right, an optical microscope image of the chip with the cavity on it. On the left a schematic, cartoon representation of the printed circuit board and the wire bonds that connect the chip and the PCB. On chip, the coplanar waveguide widens at either end of the design for easier wire bonding, and tapers significantly in the middle. The cavity is folded vertically, with 40 micron spacing between successive folds, and 1.17 mm line length between semicircular endcaps. Note that this particular chip, an earlier generation, had gold pads at either end of the center line, which have partially de-adhered in dicing. These gold pads turned out to be unnecessary in the final version, as discussed below.

This enlargement is clearly visible at either end of the chip in figure 3.3. At either end of the chip, (s,w)=(200,106.4), stated in microns, with 200 μm chosen as the smallest size we could hit with the wirebonder to which we had access. In between, the CPW tapers linearly over 400 microns to the main part of the cavity, where (s,w)=(0.500,0.262). These values are chosen to maintain an impedance of 50 ± 0.2 ohms at every point along the waveguide, according to formulas given in a standard textbook on coplanar waveguide [57].

A veteran of the superconducting microwave cavity community will immediately notice that our center line is between one and two orders of magnitude narrower than the usual center lines seen in this field, which are typically around 10 microns wide [82]. For all experiments with nanomagnets, we want to increase the coupling between the nanomagnet and the CPW. That coupling is mediated by the magnetic field which surrounds the center line. Ampere's law states that

the magnetic field strength will go like the circumference of the center line, so we tried to minimize that circumference by making s as small as possible. We chose (0.500,0.262) for (s,w) because 250 nm is roughly the resolution limit of the CNF's photolithography tool. The risk of narrowing the center line is that one increases the electric field density between the center line and the ground plane, which will increase the strength of the interaction of the cavity with any two levels systems at the metal-substrate interface, and this might decrease the cavity Q. This is why the resonator/qubit field prefers wider resonators in general. However, in our case, the increase in magnetic field strength seemed worth the risk.

Our cavity was fabricated out of niobium. Niobium is chosen for its high critical temperature and resistance to applied magnetic field. Aluminum would produce cavities with higher Q, but would not be able to stand the applied fields necessary to tune whatever nanomagnet sat on top: its H_c is 105 Oe. Tantalum might also work for our application, although we did not explore it in depth. We chose a niobium film thickness of 120 nm. If the film is too thin, the kinetic inductance of the superconductor increases very quickly. But above twice the London penetration depth (78 nm at absolute zero), extra thickness is of questionable utility[95]. We chose 120nm to be safe. We deposited this niobium film on resistive, float-zone silicon ($\rho > 10$ kΩ-cm). To reduce high frequency losses, one wants to minimize the number of carriers in the substrate, which is why we chose high-ρ silicon. We tried to remove all possible oxide from the substrate, and had no oxide on top of the circuit, because oxides contain two-level systems which are thought to be the primary dissipation mechanism that limits cavity Q [96] [97]. For this reason, float-zone silicon[98] and sapphire [82] [99] are the most common substrates for this kind of experiment.

The length of the cavity is chosen to be 2 cm, and this is a balance between

maintaining low field on the nanomagnet and small chip size. The length of the cavity determines its resonant frequency, $f = v_{ph}/\lambda$, where $v_{ph} = c/\sqrt{\epsilon_{eff}}$. (The effective dielectric constant for the coplanar waveguide, ϵ_{eff}, can be looked up from a textbook[57]. In our case, $\epsilon_{eff} = 6.34$, so we expect a half-wavelength mode at 2.97 GHz.) From equation 2.15, we know that the resonant frequency of the magnet increases with field, so keeping the cavity long and the resonant frequency low minimizes the amount of field one will need to apply to the nanomagnet. This is desirable, because we don't want to exceed the critical field of the superconductor. On the other hand, we can not increase the length of the cavity indefinitely, because it has to fit on the chip, and we want to keep the total chip size low so that it will not support spurious modes. The other way to fit more length on a small chip is to use tighter turns, and that might well be possible, although at some point the turns will be so tight that they will act as reflectors. I chose this particular turn radius so that my design was proportional to a Schoelkopf group design [100].

The copper box and PCB were actually designed by the Schwab group, a neighboring group with deep experience in superconducting microwave cavities, and manufactured professionally. The PCB is made of Arlon, a proprietary high-permittivity, low-loss dielectric, and plated in gold. The gold on the printed circuit board was patterned into a simple 50 ohm coplanar waveguide with many through holes to connect the top and bottom planes and prevent standing waves. The entire PCB was less than a centimeter square, and the lid was designed to fill the space of the cavity as much as possible so as to eliminate spurious 3D cavity modes.

We used an interdigitated "folded fingers" capacitor design common in the literature for stronger (capacitive) coupling of the cavity to the external electronics, as shown in figure 3.4. Initially, we wanted to see how high we could push the Q of the cavity, so we wanted the coupling to be strong enough that we could detect the

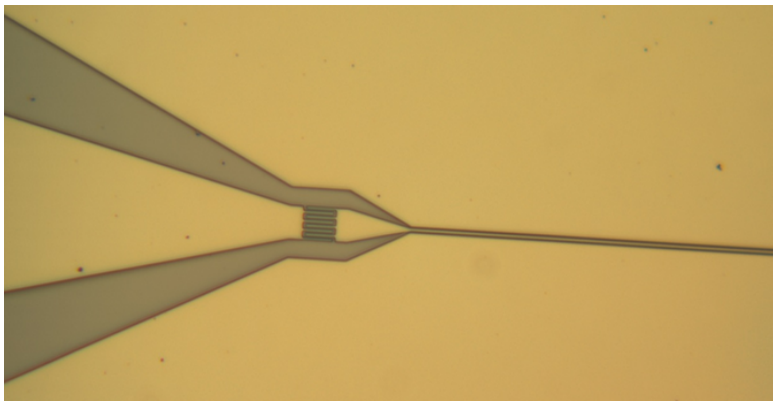

Figure 3.4: A microscope image of an interdigitated capacitor that I fabricated. The niobium is yellow, and the silicon is gray. The interdigitated capacitor interrupts the center line in the middle of its taper from center line width of 500 nm (on the right) up to its ultimate size of 200 μm.

cavity, but weak enough that photons entering the cavity would decay internally before escaping from the ends in most cases. The capacitive coupling is generally characterized by a coupling quality factor, Q_C, defined as the number of times on average a photon will reflect in the cavity before escaping. A circuit model [83] predicts that

$$Q_C = 2R_0 Z_0 \omega_0^2 C_C^2 \tag{3.1}$$

where R_0 is the impedance of the measurement circuit, here 50 ohms, Z_0 is the impedance of the cavity, which was designed to be 50 ohms, ω_0 is the resonant frequency $2\pi * 3$ GHz, and C_C is the coupling capacitance. To find C_C with a high degree of accuracy would require some modeling, but one can make a simple estimate with the most basic definition of capacitance:

$$C_C = \frac{(\frac{1}{2}\epsilon_r)\epsilon_0 n_f L t}{s} \tag{3.2}$$

where $n_f = 4$ is the number of fingers on each side, $L = 5$ μm is the length of those fingers, $t = .12$ μm is the thickness of the fingers, and $s = .292$ μm is the gap between fingers. (The fingers are 0.5 microns wide to maintain the Z_0 of 50.) $\frac{1}{2}\epsilon_r = 11.7/2$; I have divided the dielectric constant of undoped silicon by two since

there is only dielectric under the circuit and not above it. This gives C_C of 0.43 fF. Simons[57] gives examples of interdigitated capacitors of various geometries that have been modeled properly and verified from measurements in the literature. When I use this simple formula on his examples, I get values that are within a factor of two of the proper values, which gives confidence that this method is good enough for an order-of-magnitude estimate. Putting these numbers together gives Q_C on the order of 10^6.

3.3 Fabrication of Microwave Cavities

Cavities were fabricated using a combination of photolithography and RIE. The fabrication recipe is very simple. First, I cleaned a resistive float-zone silicon wafer ($\rho > 10000$) in BOE (1:30 for 30") to remove TLS-containing oxide. After quenching the etch in water, I blew it dry with nitrogen and moved it as quickly as possible into a plastic, airtight bag. Using a hand pump, I evacuated as much air as possible from this bag. I transported the wafer under this weak vacuum to the niobium deposition system, and then loaded it directly. In this way, I was able to keep the total exposure time to atmosphere after the dip to ≈ 1 minute.

Next, I sputtered 120 nm of niobium in the Lesker sputtering system described above at 100 W in 2 mTorr of argon. I characterized the critical temperature of this film by wirebonding an unpatterned sample to some leads and installing it in a vacuum can with a small heater. After calibrating the temperature sensor, I dunked the can in helium, and ramped the temperature back and forth past the critical temperature a few times. This gave a T_c of 8.95 K $\pm$ 0.1 K. Niobium has a bulk T_c of 9.3K, but one would expect a slightly different T_c for a thin film, so the measured value is in the range one would expect. I was pleased to measure T_c near the bulk value, despite the fact that the metal was deposited in a chamber

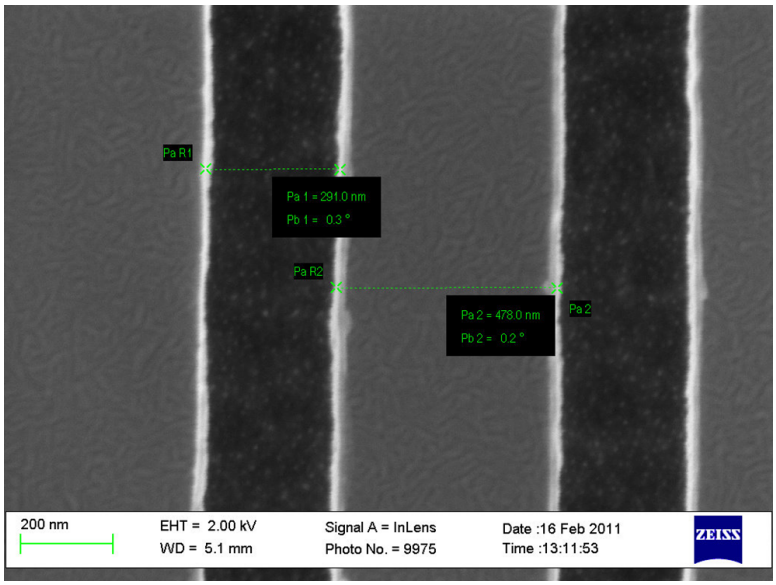

Figure 3.5: Scanning electron micrograph of niobium coplanar waveguide. The lighter gray is the niobium, and the darker gray shows the slots that have been cut through the niobium to the underlying silicon. We targeted $s = 500$ nm and $w = 262$ nm and achieved $s = 478$ nm and $w = 291$ nm. The niobium surface is quite clean, although there are occasional "tabs" of residue on the edges of the slots.

that saw magnetic materials.

To pattern the wafer, I spun ARC (AR3 @ 4K for 60", 4K ramp, 90" 205° bake) and a 248 nm resist (UV210-0.6 @ 3K for 30", 4K ramp, 60" 135° bake). I exposed the resist on the CNF's ASML 248 nm 4x stepper. Of course, I ran an energy-focus calibration grid to check the CDs before this exposure. I ended up with energy of 19 mJ/cm^2 and focus of 0.3. After a 135° 90" post-exposure bake, I developed the wafer in standard TMAH developer (726 MIF) on an automatic spray developer, double puddle recipe for 60 seconds.

I then etched the wafer in a standard parallel plate reactive ion etcher without ICP (at CNF, the Oxford 80-2). First I ran a very gentle oxygen plasma to remove the ARC from the exposed areas (70", 40W, 42.5 sccm Ar+7.5 sccm O2, 15 mTorr), and then, without venting, etched the niobium in fluorine (55", 250W, 15 sccm CF_4+15 sccm SF_6, 25 mTorr). This etch recipe was not the first thing I had tried.

Initially, I tried using an ion etch, but this doesn't work well. Niobium atoms are heavy and sticky; instead of flying off the wafer when struck with the argon ions, many of them simply redeposited on the sidewall of my resist, leaving terrible fencing that would not come off in any chemical or dry etch process. Fluorine-based RIE was much cleaner and easier[101]. After the etch, I found that the resist didn't come off cleanly in solvent, so I removed the resist with an oxygen asher (the CNF's YES Asher) for 6' @ 1000W, 100 sccm O2, at 80° C. The asher clearly removed the resist, but it left a lot of residue and particulates. Fortunately, those particles could be cleaned up with a short BOE dip, 30:1 for 3'. This recipe made consistent, clean lines at dimensions very close to what I designed, as shown in figure 3.5.

After coating the wafer in resist, dicing it into 1.5mm x 2mm chips, and stripping the dicing resist in acetone and IPA, I mounted my device in the microwave package. That package is shown in figure 3.2. To assemble, first the PCB was press fit into the box, and the chip was attached to the bottom of the box with silver paint. Then the chip was wire bonded to the PCB. At each end of the chip, the center line of the CPW measures 200 microns wide, and it was at this point that the CPW was wire bonded to the center line of the PCB. Many connections were made between the chip's ground plane and the ground plane of the PCB as well.

The wire bonding technique also turns out to be simple, although this step set me back three months. Round aluminum wire will bond directly to niobium without difficulty. However, I initially thought that it was necessary to use gold wire, which is much harder to bond. I worried that it might be difficult to bond gold directly to niobium, as niobium is hard and has a hard oxide, and I had heard from colleagues that bonding gold to gold is much easier. This led me to add gold pads to

my devices, but even after doing so, I had a great deal of difficulty with the bonding. I spent a long time fabricating wafers with different pad thicknesses, experimenting with different cleaning methods, and trying different bonder settings. Switching to aluminum wire helped. Still, the wire bonding was a very low-yield process for unknown reasons. Ultimately, the answer turned out to be the stage on which I was doing the bonding. I was using an adjustable stage to raise my sample up to the level of the bonding wedge, and it shook a little. When I replaced it with a solid piece of metal, the sample was more stable, and suddenly all of the bonding got easier. These two tricks, aluminum wire instead of gold, and a very sold stage on which to do the bonding, are hardly research breakthroughs, but I hope that they might save some future student the time that they cost me.

3.4 Measurement and Analysis of Microwave Cavities

Measurements were done in the same magnetic setup shown in figure 2.6, but with a helium dewar placed between the two large magnets. The sample box with the PCB and chip in it were placed at the base of the dewar, and the whole thing was immersed in a steady flow of liquid helium. A thermocouple ensured that the temperature was at 4.2K. I then attached the two ends of the package to the two ports of a vector network analyzer and swept the frequency of the input signal. The input power was relatively high, 100uW, and there was no filtering or attenuation. I then did the same thing with an external field of 2150 Gauss (above niobium's critical field of 1980 Gauss), to show that the peak does disappear when superconductivity is suppressed. The result is shown in figure 3.6.

To find the center frequency and Q of this feature, I cleaned up the data in two ways [82]. First, I removed a linear background from the phase. This linear background comes from the fact that the number of wavelengths that fit in the

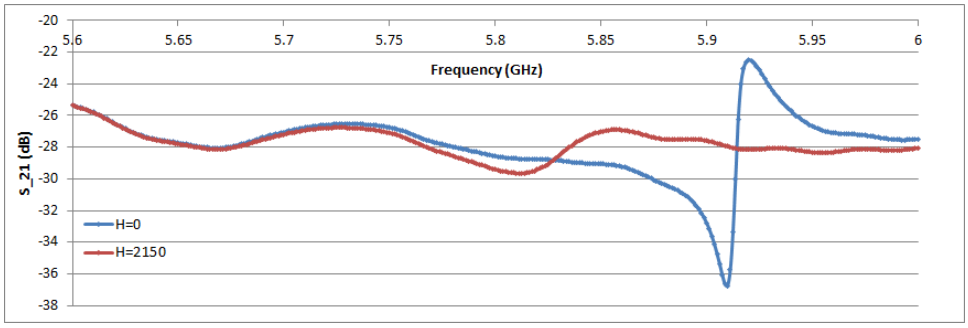

Figure 3.6: Measured transmission, S_{21}, for the device shown in figure 3.2, from a vector network analyzer. The y-axis is transmission in decibels. The two lines correspond to no applied field and applied field of 2150 Oe, above the critical field for niobium.

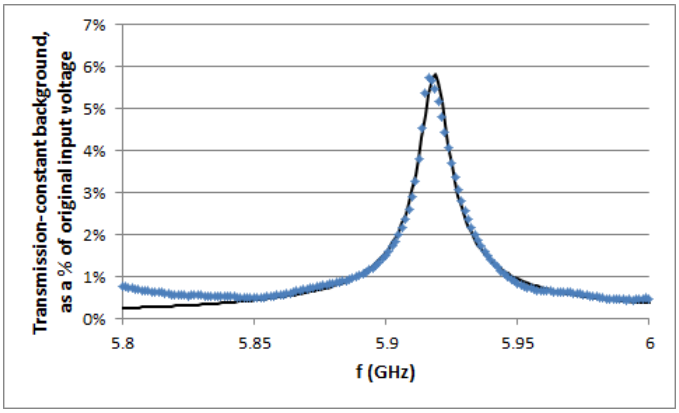

Figure 3.7: Measured transmission for the device shown in figure 3.2. In contrast to figure 3.6, the y-axis is not logarithmic here, and instead corresponds to voltage in/voltage out. A constant, complex background has been subtracted off so that away from resonance the signal is zero. The black line is a fit from equation 3.3 corresponding to Q_{tot} of 566.

cables changes continuously as the frequency increases. Second, I subtracted a constant, complex background from the signal so that the starting and ending points of the feature in question were zero in both real and imaginary space. Then I recombined the real and imaginary parts of the signal, as shown in figure 3.7. I fit the cleaned data with the expression

$$|S_{21}| \propto \frac{1}{1 + 2iQ_{tot}\frac{f-f_0}{f_0}} \tag{3.3}$$

This expression comes from a simple circuit model of the cavity[83]. The width of this peak corresponds to a Q of 566. Q_{tot} is a combination of internal losses in the cavity and the coupling of the cavity to the outside world by way of the interdigitated capacitors, according to the formula [95]

$$\frac{1}{Q_{tot}} = \frac{1}{Q_C} + \frac{1}{Q_{int}} \tag{3.4}$$

Note that it is possible in theory to calculate Q_C from the overall amplitude of the transmission, but doing so requires more careful background measurements and calculations. Given the calculation of Q_C from equation 3.1 above of $\approx 10^6$, it seems likely that Q_{tot} is dominated by Q_{int}, and that a careful measurement of Q_C isn't necessary for now. A Q_{int} of ≈ 600 is slightly smaller than expected, as it is common to measure Q of 10^3 [94] to more than 10^5 [99] [100]. The nature of these internal losses is not clear, although it's possible that the relatively high temperature and the presence of residual field from the ferromagnets could both contribute. Residue from the dicing resist is a possibility, as are material impurities or imperfections. The oxygen plasma step for cleaning the resist could be oxidizing a significant amount of niobium, and this oxide might be lossy. Also, it's possible that hydrogen is contaminating the lines during the etch, as this is a common problem in the literature [102]. A more careful tracking of the sheet resistance and critical current of the niobium before and after the etching and resist stripping

steps would help to clarify if there was material damage during processing. It's also possible, if unlikely, that the coupling Q is much smaller than I estimated. This could be confirmed by measuring devices (already fabricated) with different amounts of coupling.

The frequency of this peak is 5.92 GHz. Based on a cavity length of 2.00 cm and the calculated v=.40c, we expect a full wavelength mode of 5.95 GHz, which is extremely close. That's reassuring, although I didn't see a half-wavelength peak, which I would have expected at 2.97 GHz. To be fair, the data was quite noisy below 4 GHz. In total, there were peaks at 5.92, 7.35, 7.67, 9.38, 10.49, 12.27, 14.34, and 17 GHz. Depending on which peaks one decides are "real" and which are extraneous box modes, and to which half-wavelength multiples one assigns those peaks, one can make a somewhat compelling fit based on a half-wavelength of 2.73GHz or 2.21GHz. Neither of those fit theory well. It's not immediately clear what's going on, although one can surmise that any or all of the observed features are not true cavity modes but are instead package modes of some kind. In retrospect, designing my superconducting microwave cavity to be identical in length to the whole chip (2cm) probably wasn't a good idea. More samples of different lengths would allow more systematic conclusions.

3.5 Conclusions

I have made some progress towards the stated goal of coupling nanomagnets with microwave cavities. I have successfully designed and fabricated a high Q superconducting cavity on a chip, integrated that chip into an appropriate package, and characterized the cavity's high frequency properties at cryogenic temperatures. Before fabricating any nanomagnets, it would make sense to measure some additional resonators of various lengths in order to isolate the box modes from the

cavity modes. Decreasing the noise of the low-frequency scans so that the fundamental half-wavelength mode could be detected would give additional confidence that the measured resonance is the actual cavity mode.

Once one was more sure of which feature was the resonator mode, one could try to improve the quality factor of the cavity. Some of the highest claims for Q factor for niobium are not well-substantiated (10^6 from [100]) or come from sapphire wafers (10^5 from [99]). But a Q of 3000 was achieved in a very similar materials system ([94]), and this seems achievable. Going from Q of 567 to 3000 may be as simple as cooling the resonator to millikelvin, as there is evidence that this improves the Q value significantly [83]. Once one did this, one could claim a minor achievement: a high Q nanocavity of unprecedentedly small scale. As far as I know, the cavities I fabricated were the thinnest superconducting coplanar waveguide resonators ever made.

Then one would need to add a magnet on top of the cavity. The first experiment proposed, ferromagnetic resonance, would be very easy to do, as it would require only a single layer of lithography. The strong coupling experiment is also easy to do, although of course, in the three years since the experiment was proposed, it has been done. But this line of experimentation is still young, and other experimental realizations are still of value. The other experiments proposed involving magnetic tunnel junction oscillators are more difficult. Extensive fabrication would be needed. Of course, those fabrications recipes could build off of existing work, but nanofabrication integration is never easy. Nonetheless, these are promising experiments that could be conducted now that the resonator fabrication and packaging has been demonstrated.

CHAPTER 4

MAGNETIC MULTILAYER NANOWIRES AS ELECTRICALLY SWITCHABLE SPIN-CURRENT INJECTORS

4.1 Introduction and Motivation

Since Datta and Das proposed a spin-based transistor[10] in 1990, many researchers have been interested in spintronics, the use of spins for computing. Because of the short decay length of spins in metals, semiconductors are the ideal choice for spintronic circuits. However, generating a spin current in an all-semiconductor circuit is difficult. Ferromagnets are the most natural sources of spin-polarized currents, since a current running through a ferromagnet becomes spin-polarized in the same direction as the ferromagnet. A ferromagnetic semiconductor would be the ideal material for a spintronic source[103], but almost all ferromagnetic semiconductors work below room temperature[7], and reports of 300K ferromagnetism in semiconductors are controversial[104]. So it's more common to use a metal ferromagnet to generate the spin-polarized current and inject that current into a semiconductor. Many groups have created devices that do this[7][105][106][107][8][108][109]. The problem with these devices, from a spintronic point of view, is that they can only inject one orientation of spins—the orientation that aligns with the ferromagnet. The metal ferromagnet can be switched with a magnetic field, but field switching is impractical for any sort of large scale integrated circuit. Ideally, one would like an electrically switchable ferromagnetic injector. The Ralph group has a long history of using spin-torque to make electrically-switchable ferromagnets. Our goal in this project was to demonstrate an electrically switchable ferromagnetic injector for pushing spin currents into semiconductor circuits.

Spin-torque switchable ferromagnets are not hard to make—this is the end

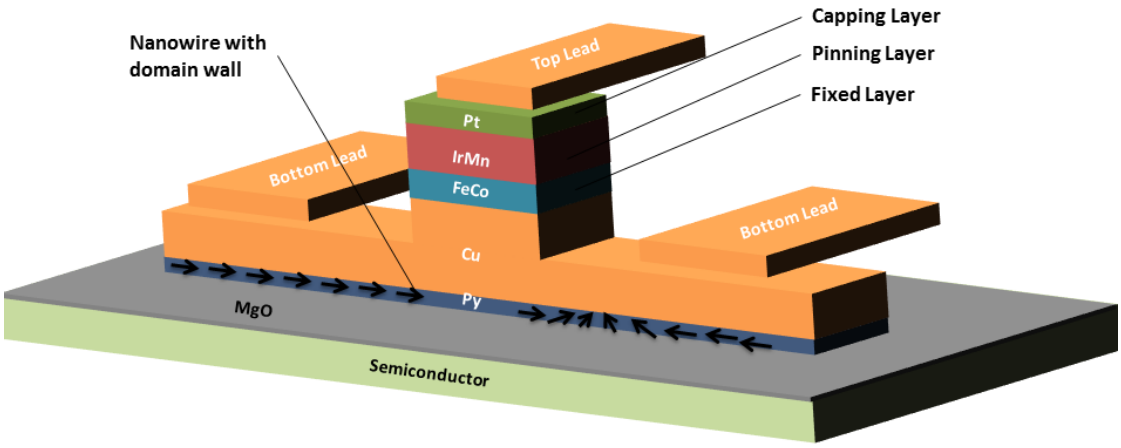

Figure 4.1: A schematic depiction of the device proposed in this chapter.

product of the nanopillar fabrication process described in section 2.6 above. One could simply put such a nanopillar on top of a semiconductor, and call it a switchable spin injector. However, that process creates a magnet with nonmagnetic material on both sides. Spin polarization decreases as a spin current passes through non-magnetic metal, so the polarization of the spin current would be reduced by the time the current reached the semiconductor. Ideally, it would be best to have a switchable nanomagnet that is the bottom layer of a magnetic device, which is not the case with the nanopillar. If such a device were placed directly on top of a semiconductor, this would allow for more efficient spin injection. However, the requirement that the magnetic "free layer" be on the bottom of the stack requires a total reimagining of the device's geometry.

The result of that reimagining is a nanowire device like that shown in figure 4.1. Now the free layer/injection layer is not a round nanomagnet, but a ferromagnetic nanowire (the permalloy layer). The goal is to nucleate a domain wall (DW) in the permalloy nanowire, and then to move that DW around with spin torque. A voltage between the bottom electrode and the substrate will cause spin-polarized current to be injected into the semiconductor, and the position of the domain wall

will determine the percentage of the current that is polarized one way as opposed to the other. (For reference, one would expect no net spin polarization if the DW is in the middle of the device, and 100% spin polarization if the DW moves all the way to either end.)

To move the DW, one applies a voltage between the top and bottom leads as shown in figure 4.1. When current is passed from the top electrode to the bottom electrode, it becomes spin polarized when it passes through the fixed, uniformly-magnetized FeCo layer. The spin-polarized current applies a torque to the ferromagnetic spins in the permalloy and causes more of the spins in the nanowire to align with the fixed layer. (This "increasing alignment" takes the form of the domain wall moving in the appropriate direction.) To move the domain wall in the opposite direction, current is flowed in reverse, so that spins reflected from the fixed layer have the opposite polarization. Note that because of spin accumulation, there is spin-torque on the free layer even though the charge current doesn't flow directly through the free layer[6].

Several groups have constructed similar devices that move domain walls in nanowires with spin-torque[11][110][111][112]. One of the keys to making domain wall motion a viable technology is minimizing the switching current necessary to move the domain walls[11]. A recent paper out of Krivorotov's group is the most promising[110], showing high DW speeds at current densities below 10^7 A/cm^2. Unfortunately, their device had the current flowing perpendicular to the plane of the device (CPP)—which isn't possible with the magnetic free layer on the bottom of the device. Other work has shown domain wall motion with current moving parallel to the plane of the device (CIPT)[111], in geometries similar to ours, at critical currents around 5×10^7 A/cm^2. Both CPP and CIPT geometries seem to have lower critical currents than geometries in which the current passes

directly through the layer with the domain wall[112]. These previous works inspire our own design. Minimizing inadvertent domain wall pinning from impurities is also key to keeping switching current low[11][110], and it seems that annealing may help with this[111].

If one creates a nanowire like the ones shown in figure 4.1 and puts it onto a semiconductor, one would have a very nice 3-terminal device. It's motivating to briefly imagine a few experiments that one might do with such a device, although none of these experiments was performed. The application described in the first paragraph, a switchable source for spintronic circuits, is the most straightforward application, but it's not the only demonstration one could do with such a device. One can connect the worlds of photonics and magnetic memory. In the device shown in figure 4.1, imagine that the semiconductor is a GaAs/AlGaAs quantum well, which will act as an LED when current is injected. If the injected current is spin-polarized, then the photon coming out will have a preferential circular polarization [7][8]. Thus, this mechanism effectively transfers the information in the ferromagnet into a photon. (Experimental details and demonstration can be found in [107]. Basics of this effect are explained by Kittel[54] (p578).) So this device acts as both a non-volatile memory and a switchable source for photonic circuits as well. Perhaps most promisingly, one could replace the semiconductor with some other more exotic material, such as a topological insulator or a multiferroic. Although one could more simply put a fixed ferromagnet on top of these systems to inject a simple spin-polarized current, in our system, by moving the domain wall back and forth quickly, one could inject an AC spin current with frequencies potentially in the GHz regime[110]. That would represent an exciting new way to probe these exotic systems at higher frequency, and thereby examine non-equilibrium dynamics. Given the excitement around topological insulators in the scientific community at

the moment, this might be the most promising scientific application.

With these motivations in mind as future goals, our immediate goal for this project was simply to make a nanowire like the one shown in figure 4.1 on a regular Si/SiO_2 wafer and demonstrate domain wall motion. Even without the semiconductor underneath, we expected to be able to monitor the movement of the domain wall by passing a small current between the top and bottom electrodes and monitoring the change in resistance due to GMR. If necessary, we knew that magnetic force microscopy[11], spin scanning electron microscopy[113], or the magneto-optic Kerr effect[114] could be used to further probe the magnetization. Unfortunately, we never managed to measure domain wall motion, as the fabrication of a high aspect-ratio nanowire of this kind turned out to be unexpectedly difficult. In the sections that follow, I will describe the device I designed, the fabrication recipe that I developed to build it, and the results of our fabrication attempts.

4.2 Design and Fabrication of Nanowire Devices

The design of our nanowire device is based on other similar nanowires found in the literature. The masks used to make our pattern are shown in figure 4.2. We made nanowires of various widths, but the base size was 90 nm, after Boone[110]. The width of the nanowire is crucial. Making the nanowire thinner is advantageous because thinner wires generally have simpler DWs that are easier to move. Parkin[11] reports on the variety and complexity of DWs that can emerge, and the group of Vouille reports that their domain walls changed shape and became stuck after repeated movements[113]. But too thin, and the aspect ratio of the device becomes large, which makes it difficult to fabricate. The elbow in the nanowire seen in the zoomed-out view of figure 4.2 is the nucleation site for the domain wall: a magnetic field pointed in the five o'clock direction will nucleate a domain wall

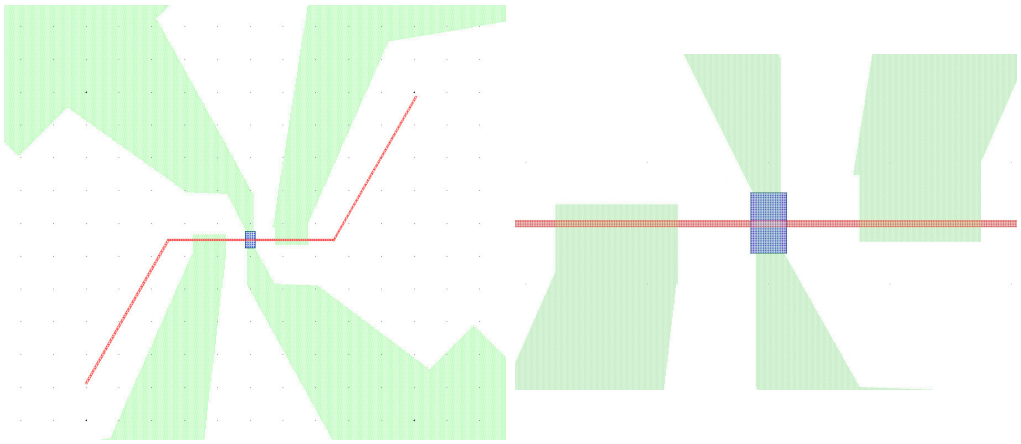

Figure 4.2: Top view of the nanowire device. On the right, a zoomed-out view; on the left, a zoomed-in view of the nanowire itself. These pictures are from the CAD files that were used to generate the masks/e-beam file that defined the device, so they are to scale. The red is the nanowire (L2), the blue is the pillar with the fixed layer (L3), and the green shapes are the pads (L4). The alignment marks (L1), are not shown, as they are far from the device.

at the right hand elbow, which can then be moved into the wire[111]. The size of the fixed layer pillar isn't crucial, nor is the size or location of the electrodes.

The first step was to deposit the metal layers, done with magnetron sputtering in the Lesker sputter system, in exactly the same manner as described in earlier chapters. The starting layer stack is Py(30)/Cu(300)/FeCo(60)/IrMn(150)/Pt(50), where all thicknesses are in angstroms. The permalloy is the free layer/injector layer in which the DW is formed and which will act as a spin filter for any current passing into the (theoretical) semiconductor. A minimum thickness is needed if this layer is to act as a spin filter, and there may be some interdiffusion of copper and permalloy at the interface, which will further decrease the effective thickness[110]. However, the switching current needed to move the domain wall will scale with thickness of this layer. 30 Å is chosen as a compromise between these factors. The copper is a spacer that will carry the switching current out—the thickness of this layer is based on a similar 3-terminal spin torque device made by Jonathan Sun and company at IBM[12]. The FeCo is a polarizer layer. It needs to

be thick enough to ensure maximum polarization; 6 nm is an estimate that value. The other layers in the device are auxiliary: the IrMn is an antiferromagnet and serves to pin the FeCo layer in place, and the platinum cap is to prevent oxidation of the stack. In figure 4.1, there is an MgO layer between the permalloy and the semiconductor. If this insulator is not in place, there will be a large Schottky barrier between the metal and the semiconductor. There is some discussion in the literature that just tunneling through the Schottky barrier might be better for injecting spin-polarized current[108], but many groups have used an insulator as well[107][109] to achieve roughly equal spin-injection efficiency. This discussion remains theoretical, as we never got to the point of fabricating these nanowires on semiconductors. All the work that will be described below is just metal on 100 mm SiO_2(2500)/Si substrates.

In the diagrams that follow, I will describe the most promising fabrication recipe developed to make a spin-torque switchable domain wall in a nanomagnet. The fabrication involves 4 lithography steps: alignment marks (L1), nanowire (L2), spin injection column (L3), and pads (L4). The CAD for the masks used in each of these steps is shown in figure 4.2. The results of this fabrication recipe will be presented concurrently in the next section.

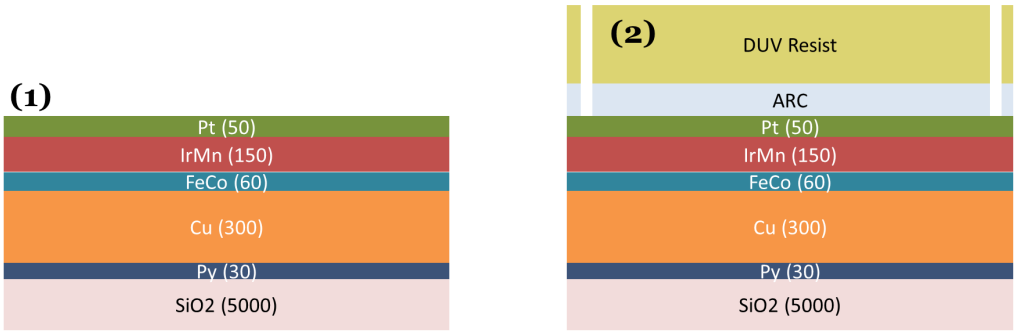

Figure 4.3: **(1) Deposit metal layers.** The stack shown was deposited in the Lesker sputter system, as described in section 2.6 above.
(2) Define L1: alignment marks. To do this, I spun an anti-reflective coating (ARC) (AR3 @ 4K for 60", 4K ramp, 90" 205° bake) and a 193nm resist (UV210-0.6 @ 3K for 30", 4K ramp, 60" 135° bake). I exposed the resist on the CNF's ASML 193nm 4x stepper at 25 mJ/cm^2. After a 135° 90" post exposure bake, I developed the wafer in standard TMAH developer (726 MIF) on an automatic spray developer, double puddle recipe for 60 seconds. Finally, I etched the ARC in a Ar/O_2 plasma (the standard CNF ARC etch recipe is 70", 40W, 42.5 sccm Ar + 7.5 sccm O_2 in the Oxford 81 parallel plate reactive ion etcher). This is the standard ASML resist recipe, and I will refer to it in that way going forward.

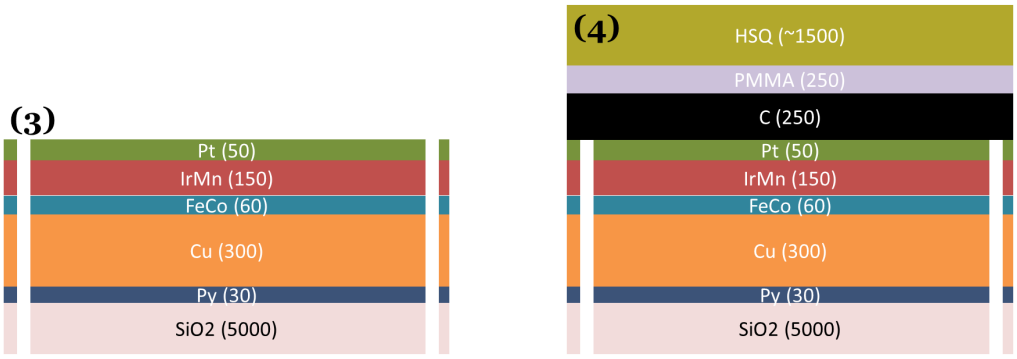

Figure 4.4: **(3) Etch alignment marks.** First, I ion milled away the metal. I used "Praveen's Ion Mill" at 35mA/150V, 10 degrees off normal with the wafer rotating, with a (10" on)/(30" off) duty cycle for 13 minutes of etching (52 minutes total). Second, I etched at least 500 nm into the oxide. I did this with reactive ion etching using CHF_3 (50 sccm)/O_2 (2 sccm) in the Oxford 81, 50 mTorr, 15x[1' on /1' off], 200W. Third, I removed the remaining resist and ARC with an oxygen plasma (YES Asher, 2x [3' @ 80°, 1000W]).
(4) Deposit the nanowire mask. I began by evaporating 25 nm of carbon. In the CNF, I used the "even hour" evaporator, a CVC-made SC4500 bell jar evaporator. Then, I spun a sacrificial PMMA layer (PMMA 2% 495K in anisole @ 3K for 60", 3K ramp, 15' 170° bake) and an HSQ e-beam resist layer (XR1541-06 @ 3K for 60", 3K ramp, 2' 170° bake).

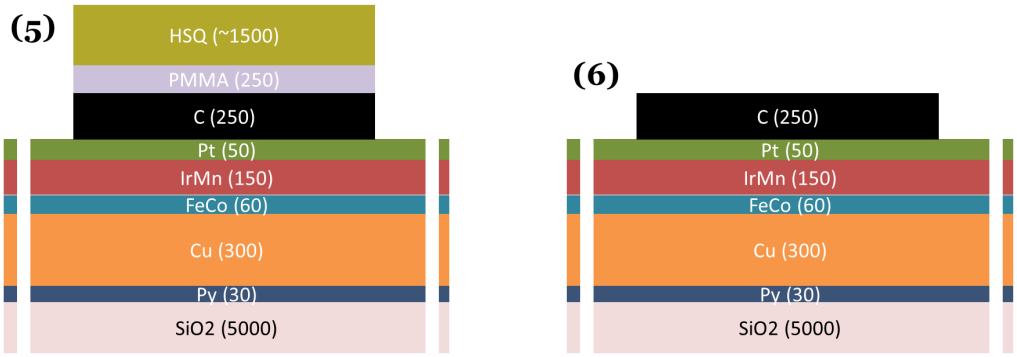

Figure 4.5: **(5) Define L2: nanowire.** I wrote the pattern on an e-beam lithography system, a JEOL6300. I used a 1 nAmp beam with doses in the range of 1000-1500. In general, I would run a dose test to see which dose gave features of the appropriate size. I would then select that dose without biasing the pattern. After writing the pattern, I developed the wafer for 2' in standard 2.38% TMAH (MIF300, double puddle spray develop on a Hamatech autodeveloper). Finally, I transferred the e-beam pattern to the carbon with an oxygen etch. (In the CNF, I used the Oxford 81 for 50", 100 W, 50 sccm O2.)
(6) Lift off HSQ. I soaked the wafer overnight in a 50/50 mixture of methylene chloride and acetone to lift off the PMMA and HSQ lines. The methynele chloride attacks the PMMA very aggressively, and can be used on its own, but it tends to evaporate quickly if there is any gap between the beaker and its cover. The addition of acetone reduces this risk. Acetone and isopropyl alcohol (IPA) are used as a wash after the soak.

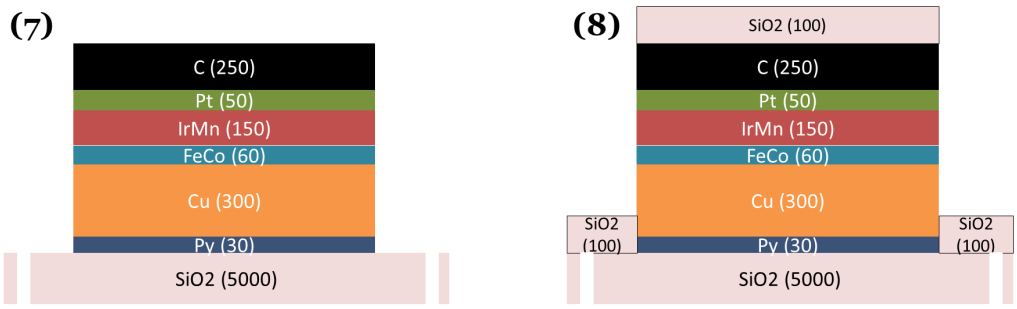

Figure 4.6: **(7) Mill to oxide.** Using "Praveen's Ion Mill" at 50mA, 200V, 30° off normal with the wafer rotating, I milled until the permalloy signal receded in the end point detector, about 12 minutes of continuous etching. Then I rotated the sample and did a 1' of sidewall clean at 65° off normal to remove redeposited material from the sides of the nanowire. After venting the system, I immediately unloaded the wafer into IPA, and left it there until the following step.
(8) Protect nanowire edges. Evaporate 10nm of SiO_2 in the "even-hour" evaporator. The goal is to deposit oxide so as to prevent the permalloy from forming a native oxide which would be antiferromagnetic and might inhibit DW motion.

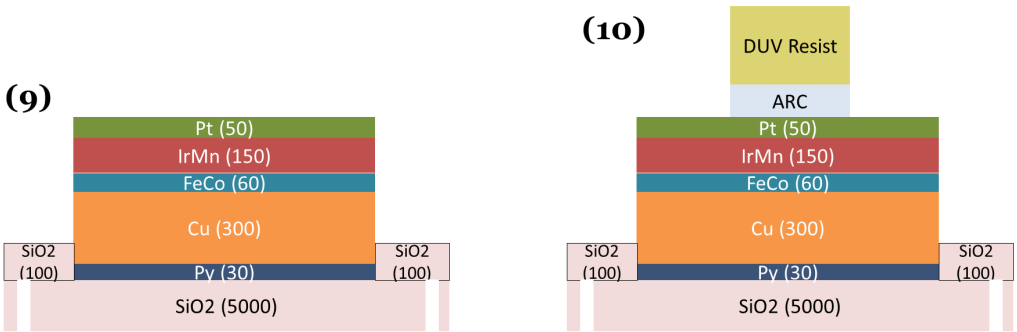

Figure 4.7: **(9) Remove carbon mask.** I removed the carbon mask with an oxygen plasma. (In the CNF, I used the Oxford 81 for 55", 100 W, 50 sccm O2.)
(10) Define L3: fixed layer. I spun on ARC and resist, shot the pattern, and developed according to the standard ASML recipe described above.

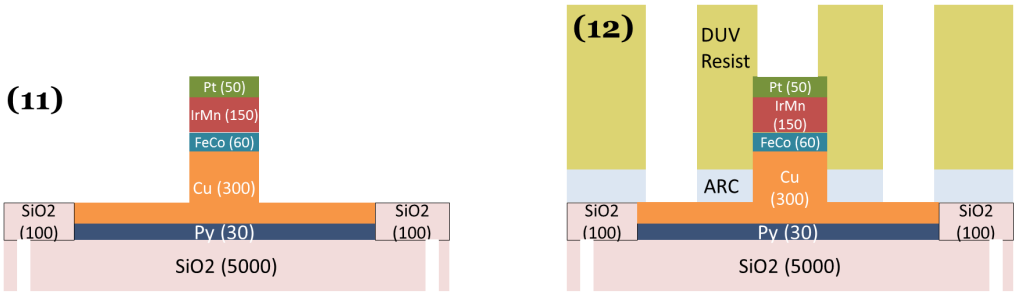

Figure 4.8: **(11) Mill to the beginning of the copper.** Using the first etch as a calibration, choose an etch time that will go through the FeCo and to the top of the copper. Etch in the same fashion as step (7), with a similar sidewall clean. Unlike in step (7), use a 10" on/30" off duty cycle to avoid burning the resist. When finished, strip the etch mask in an oxygen plasma (YES Asher, 2x [3' @ 80°, 1000W]).
(12) Define L4: electrical pads. I spun on ARC and resist, shot the pattern, and developed according to the standard ASML recipe described above.

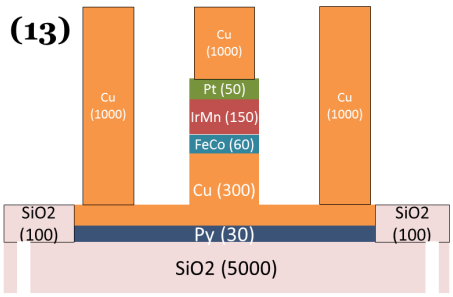

Figure 4.9: **(13) Apply copper pads.** In a deposition system with in situ ion etching capability, clean the oxide off the pads and then deposit 100 nm of copper or gold. (I intended to use the "old IBD", sputter etching the pads for 10 seconds at 20° off normal and then sputtering Cu at about 4nm/min.) Then lift off the mask and the extra copper in acetone overnight.

4.3 Fabrication Results and Challenges

As I never reached the point of a working device in this project, I will present the status and challenges of fabricating a nanowire device as described in the previous section. Many of the layers were demonstrated separately. Layer 1, alignment marks, was demonstrated successfully with the parameters described. The two-part etch (metal then oxide) is necessary because after the L2 etch, any metal marks will be gone, and I intend to use the same marks for L3 and L4 alignment. Initially, I tried milling at 30° off normal, and this caused significant resist peeling at the edges of the marks, especially at the ends of the crosses. The horizontal momentum of the ions appears to have been pulling off the resist. Switching to 170 degrees solved this problem. I also initially had heat issues with the resist– the resist would crack, and I had trouble stripping it. By adding duty cycles to both the ion mill and the RIE steps, I was able to solve this problem. (I didn't prove that both were necessary, so it's possible that this recipe is too careful.) The final marks that I made were 570 nm deep, uniform, clean, and yielded at a rate of $> 90\%$. The e-beam lithography system detected them easily during the L2 exposure.

Layer 2 is the most complicated, the most crucial, and the most difficult step, so let me return to it in a moment. Layer 3, the definition of the fixed layer pillar, was partially demonstrated. I tested the photolithography and showed that this worked, but I did not test the etch. Because the photolithography for this step involves a small, isolated feature surrounded by exposed area, the pillar of resist receives a lot of unintended dose from scattering. I found that I needed to print the pillar on the mask at 710 nm x 540 nm in order to get an actual pillar of resist that was about 500 nm x 300 nm wide, as intended. I did not demonstrate the etch, but I have confidence that the resist will hold up to the etch because it did so in

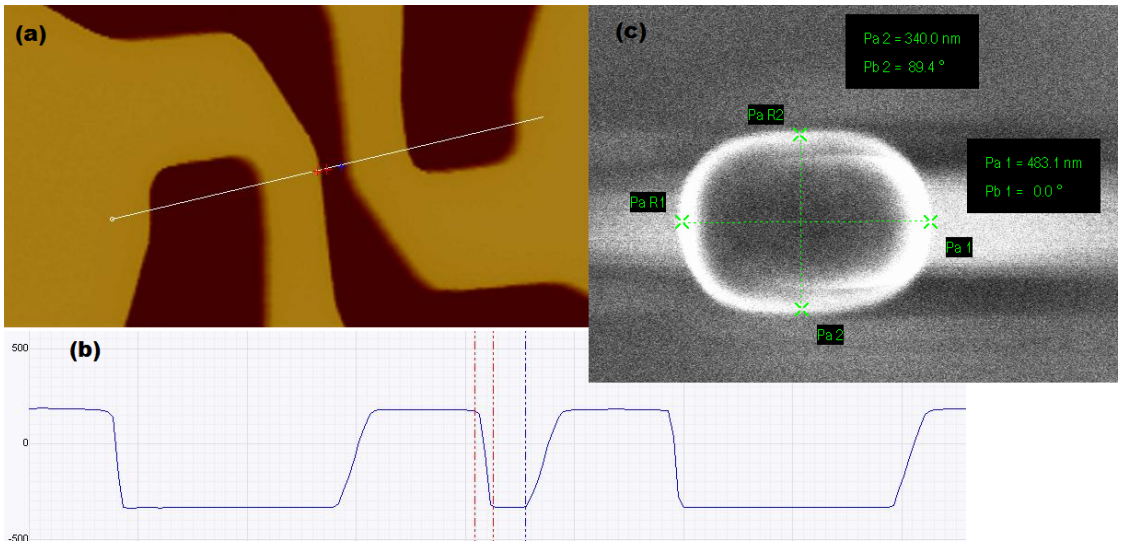

Figure 4.10: (a) A top view image of the L4 photoresist pattern taken with atomic force microscopy (AFM). The yellow and brown regions are different heights; the white line is the line of measure and isn't a physical feature. (b) Side view of the same AFM image, showing the photoresist to be 500nm tall. (c) A scanning electron microscope (SEM) image of the photoresist pillar that will define L3. The streaks on either side of the rectangle are imaging artifacts and not physical.

the tests of layer 1. Layer 4 was similarly demonstrated in photolithography only. The photoresist patterned in the images of L3 and L4 are shown in figure 4.10. Layer 4 should be relatively straightforward, although there could be some trouble making contact between the pad and the nanowire if the oxide formed during the L3 resist strip is very thick. This would need further calibration.

Fabricating layer 2, the nanowire itself, turned out to be the most difficult step. Initially I hoped to use just the e-beam resist, hydrogen silsesquioxane (HSQ), as an etch mask. E-beam resists generally don't have very good ion mill resistance, but HSQ is a flowable oxide, and I hoped it might perform similarly to crystalline SiO_2. The plan was to put HSQ on top of PMMA, etch at 10^o off normal, and then lift off the PMMA in acetone after etching. Initially, this seemed promising. After development, I measured a resist pattern of the appropriate shape that was 130-150 nm high, as expected. But after the ion mill step, I had two interlocking

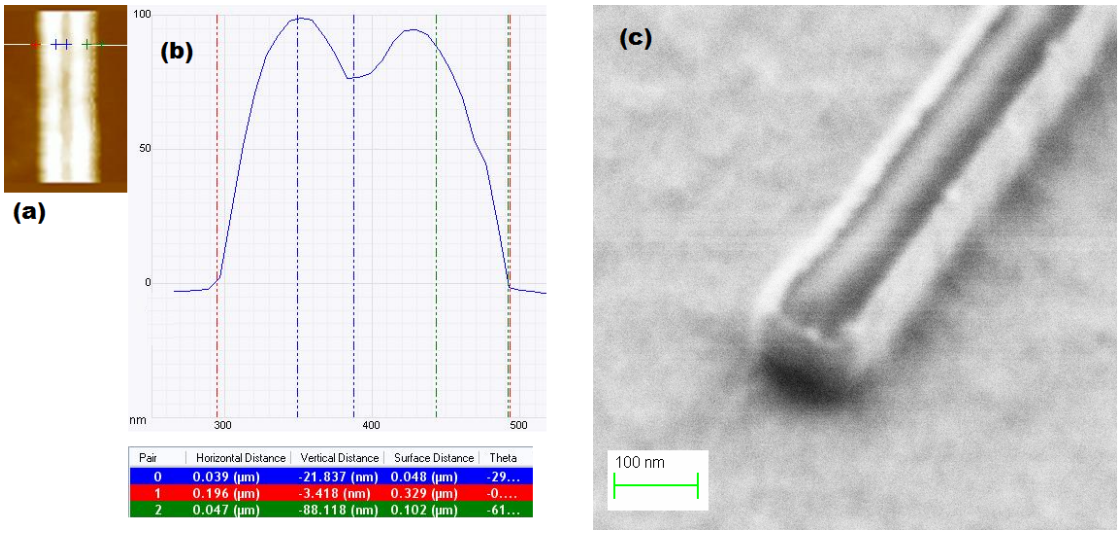

Figure 4.11: (a) A top view image of a typical etched nanowire taken with atomic force microscopy (AFM). The white lines and colored crosses are measurement marks, not physical features. (b) Side view of the same AFM image. The wire is 196 nm wide at the bottom, 180 nm wide in the middle, and has bunny ears that are 20nm tall. (c) A tilted SEM image of a different but similar nanowire. Thanks to Daron Westly for his help with this image.

problems. First, after the etch, there was so much sidewall redeposition that my wire had huge "bunny ears" of accumulated material on either edge of the wire that wouldn't lift off. Microscope images of these "bunny ears" are shown in figure 4.11. These sidewall depositions often prevented liftoff all together. Even when they did not, at 20 nm high, they were significant enough that I wouldn't be able to reliably complete the L3 etch. Recall that the L3 etch requires some precision, as it's necessary to go through the FeCo while preserving the Cu underneath, and the Cu etches twice as quickly as the FeCo. Twenty nanometers variation from the edge of the wire to the center would make this etch quite difficult. Second, there was significant widening of the pattern. The e-beam lithography system itself added an average of 15 nm from overdose. Then the etch added another 55-135 nanometers of widening. At least some widening is expected—when milling slightly off of normal (as is necessary to prevent sidewall redeposition), the bottom

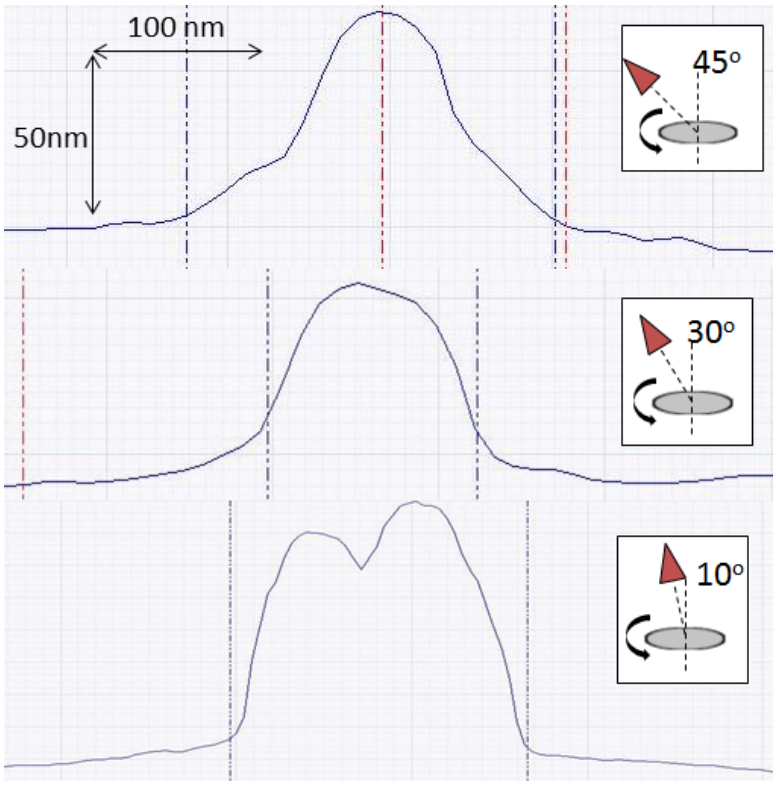

Figure 4.12: Atomic force microscope cross-sectional profiles of three different wires etched at three different angles, as shown. All three traces have been fit to the same scale. The colored dashed lines are just measurement marks and have no physical meaning. These three wafers, like all the wafers in this study, were rotated during milling. The wafer rotated at higher angles away from normal were narrower but showed more "flaring", that is, widening at the base of the wire.

of the pattern is wider than the resist at the top—although the degree of widening that I regularly observed couldn't be explained by this effect alone.

I tried a variety of milling angles, as shown in figure 4.12, and this helped a bit. Higher angles helped solve the "bunny ears" problem. This makes sense if the origin of the "bunny ears" is sidewall redeposition. Further, at higher angles, the top of the structure is more narrow, closer to the drawn size. But the penalty is that the base of the wire flares out and can be quite large, 200 nm or more. Since the permalloy is at the bottom of the stack, and the width of the permalloy is the critical dimension, flaring was especially problematic for my devices. The

obvious solution to the flaring problem is just to etch deeper into the oxide so that the permalloy wire is not in the "flared" base of structure. Unfortunately, I was already worried that I was running out of HSQ during the etch, since the liftoff was not consistently successful from wafer to wafer, and it's not easy to tell from microscope images whether there's resist or not on top of the device. Etching for even more time seemed impossible. I tried baking the HSQ and plasma-hardening it in an oxygen plasma; these measures didn't increase its etch resistance significantly. I shortened the initial metal stack by 20 nm by cutting the IrMn/Pt layer from IrMn(250)/Pt(250) to IrMn(150)/Pt(50). Nonetheless, I always seemed to be on the edge, if not over the precipice, of running out of HSQ.

I decided to switch to a carbon mask, similar to the nanopillar process described in section 2.6. Carbon has much better ion etch resistance than HSQ, at least 3.5x better based on their respective sputtering rates[115], but probably closer to 10x better since HSQ obviously etches much more quickly than thermal SiO_2. This would allow me to etch longer, into the oxide, to make sure that the flaring occurred below the permalloy layer. It would also reduce the width of the etched wire, since there would be less shadowing from a shorter mask. Finally, I hoped that the carbon would lift off in oxygen plasma more reliably than the PMMA/HSQ did in solvent. My reasoning was that the relatively thin PMMA layer (about 50nm) was only accessible from the sides, and the sides could be easily covered by redeposition. But the carbon had nothing covering it, so even if it was covered on the sides, it was still accessible from the top. After calibrating the new carbon process, I only had the chance to test it a few times, and I hadn't yet worked out the kinks. For example, when the PMMA lifts off the carbon, it appears to peel off some of the carbon in the process, leaving a lumpy, thinner layer of carbon. This is not an insurmountable problem, but I didn't get the chance to remedy it.

4.4 Conclusions

In this project, I designed an electrically-switchable three terminal device for injecting spin currents into semiconductors or insulators. I designed a fabrication recipe to make that device, and made significant progress towards fabricating a complete device, including the demonstration of the lithography for all four layers. I made many devices that successfully demonstrated the first two layers, although the quality of the nanowires was mediocre.

The fabrication of this multilayer magnetic nanowire turned out to be unexpectedly difficult. As the nanowire alone wasn't particularly novel, one might ask how similar devices were made in the literature. The answer is that most devices differ from ours in one of several ways. Many are simpler, one magnetic layer in which the spin torque current is generated from the magnetic wire itself[113][116][117][118]. In that case, the total height to be etched is much less. Many are wider[119][112][111], 200-400 nm. Those that are most similar, in that they are narrow and have separate free and fixed layers, have the free layer on top of the fixed layer and electrode layers[110][120]. In this case, it's easy to use angled milling to confine the nanowire size and ignore flaring in the bottom of the wire. What caused fabrication of this device to be difficult was the combination of the relatively high aspect ratio of the wire (59 nm high x 90 nm wide) combined with the requirement that the most important layer, the free layer, be on the bottom of the stack.

Going forward, one could relax some of these requirements. One could accept wider widths, although the difference between 100 nm and 200 nm is probably the difference between transverse and vortex domain walls[11], and vortex domain walls show complicated behavior[117]. One could thin the copper spacer, although then it becomes difficult to stop the L3 etch at the correct point. One could

simply stick with a traditional nanopillar, and accept a slightly lower spin-injection efficiency. Or, one could just tweak the nanowire process described above. Despite the difficulties to date, there are reasons to believe that the nanowire etch is close to working, as it is quite similar to the established nanopillar process. Further, given that the first two layers were already integrated and that the third and fourth layers had been partially demonstrated, a fully integrated device might not be far away. Still, it is not likely that the first generation device will work at all, and undoubtedly significant tuning and tweaking would be needed to reduce switching current, make reliable devices, and integrate them onto a semiconductor or exotic insulator. This project is still in its early stages.

In the introduction, I presented three possible motivations for the switchable current injector that we were trying to make: spintronic source, photonics memory/source, and high frequency spin injection into multiferroics or topological insulators. A simple argument can be made for why each of those applications is exciting, but I have not made the converse arguments about why this nanowire design is not appropriate for these applications—what alternatives are a more natural fit for the application, or the potential drawbacks of using this kind of device for the application. As fabrication of this device has proved to be difficult thus far, a more careful analysis of these questions might be appropriate moving forward.

The value of this project, if all four layers of the nanowire device were integrated onto a semiconductor, is as a demonstration technology. Most of the scientific questions one might ask could be more simply answered with simpler devices. But demonstration devices are useful stepping stones to new technologies. With more perseverance, this particular device could demonstrate an elegant way to bring together magnetics and photonics, serve as a switchable spintronic source, or probe exotic materials.

APPENDIX A

NOTATION FOR SWITCHING CURRENT

In equation 2.2, I assert that the switching current for an MRAM bit is

$$I_c = \frac{2e}{\hbar}\frac{\alpha}{\eta}(E_u + E_\perp) \tag{A.1}$$

where E_u is the energy difference between magnetization along the easy-axis and the in-plane hard axis, and $E_\perp$ is the energy difference between magnetization along the easy-axis and the out-of-plane hard axis. This assertion is based on Jonathan Sun's work in [18], although the notation used in that work is differen. This notational difference has led to confusion about a factor of two in other parts of the literature.

After setting up his own coordinate system and energy equations, Sun calculates that the switching condition is given by:

$$I_c = \frac{2e}{\hbar}\frac{\alpha V}{\eta}\left(M_S H + 2K + K_p\right) \tag{A.2}$$

In his notation, H is the external field, K is the energy density of the uniaxial anisotropy, and K_p is the energy density of the planar anisotropy.[1] (Note that I wrote equation A.1 to describe the case in which $H = 0$, which explains why my equation does not contain this term.) Comparing equations A.1 and A.2, one notices the factor of two difference between the two energy terms in Sun's formulation which is not present in mine.

The factor of two discrepancy is explained by the way Sun defines his terms. Sun is not trying to describe shape anisotropy, so he defines the easy plane and the uniaxial anisotropy in an additive way. The energy density of the out of plane configuration, using his notation, is actually $K + K_p$. As I have defined $E_\perp$ to be

[1] Starting from Sun's equation (17), I made some substitutions based on his definitions. Note that I have made the assumption that $M = M_S$, which Sun doesn't make initially, but which seems appropriate in this case.

the energy difference between out-of-plane magnetization and in-plane easy axis magnetization, the appropriate relationship between the two notations is

$$E_\perp = V(K + K_p) \tag{A.3}$$

$$E_u = VK \tag{A.4}$$

(Multiplying by the volume, V, is necessary to go from an energy density to an energy, but it is incidental. The point is the addition.) These equations resolve the apparent contradiction between the two forms of I_c.

Note that in Sun's original paper, he specifically says that he's not trying to describe shape anisotropy, and in that context, he's free to define his energy terms in whatever way makes sense to him. However, he then makes the approximation that $K_p = 2\pi M M_S$, presumably thinking of the shape anistropy energy of a thin film magnet. To describe shape anisotropy, it would be more correct to write $K + K_p = 2\pi M M_S$, since using his energy equations, the energy of the perpendicularly magnetized state is $K + K_p$. In the limit that he's considering, $K_p >> K$, this an unimportant mistake. But this mistake has propogated through numerous papers in which the easy-plane anisotropy comes from the shape of the magnet, including a paper on which I am an author[56].

Note that it is most correct to write shape anisotropies in terms of the geometric demagnetization factors, **N**, of the device under consideration. In this case (assuming an elliptical thin film magnet in the x-y plane with the longer axis in x), $E_\perp = \frac{1}{2}(N_z - N_x)\mu_0 M_S^2 V$ and $E_u = \frac{1}{2}(N_y - N_x)\mu_0 M_S^2 V$. Written in this way, one sees the symmetry between the two terms, and concludes that they must be treated symmetrically in the critical current equation. For reference, the definitions of all the energy terms and magnetic fields I will define in chapter 2 are summarized in table A.1.

	Definition	In terms of other expressions
H_d	Amount of field needed to saturate the magnetization in the out-of-plane hard-axis direction	$= \frac{E_\perp}{\frac{1}{2}\mu_0 M_S V} \quad = (N_z - N_x)M_S$
$E_\perp$	Energy difference between magnetization along the easy-axis and the out-of-plane hard axis	$= \frac{1}{2}\mu_0 M_S V H_d \quad = \frac{1}{2}(N_z - N_x)\mu_0 M_S^2 V$
H_{c0}	Amount of field needed to saturate the magnetization in the in-plane hard-axis direction	$= \frac{E_u}{\frac{1}{2}\mu_0 M_S V} \quad = (N_y - N_x)M_S$
E_u	Energy difference between magnetization along the easy-axis and the in-plane hard axis	$= \frac{1}{2}\mu_0 M_S V H_{c0} \quad = \frac{1}{2}(N_y - N_x)\mu_0 M_S^2 V$
I_c	Switching current	$= \frac{2e}{\hbar}\frac{\alpha}{\eta}(E_u + E_\perp) = \frac{2e}{\hbar}\frac{\alpha}{\eta}\frac{\mu_0 M_S V}{2}(H_d + H_{c0})$

Table A.1: The demagnetization fields, anisotropy energies, and critical current as defined in this paper. M_S is the saturation magnetization of the material and V is the volume, and N_x, N_y, and N_z are the geometric demagnetization factors. The notation assumes an elliptical thin film magnet in the x-y plane with the longer axis in x. All forms of magnetoanisotropy other than shape anisotropy are ignored here, and can be added back in as necessary. Note that for a (220 nm)x(70 nm)x(3.5 nm) elliptical prism, $\mathbf{N} = (.01, .04, .95)$[16].

BIBLIOGRAPHY

[1] M. N. Baibich, J. M. Broto, A. Fert, F. Nguyen Van Dau, F. Petroff, P. Etienne, G. Creuzet, A. Friederich, and J. Chazelas. Giant magnetoresistance of (001)Fe/(001)Cr magnetic superlattices. *Physical Review Letters*, 61:2472–2475, Nov. 1988.

[2] G. Binasch, P. Grünberg, F. Saurenbach, and W. Zinn. Enhanced magnetoresistance in layered magnetic structures with antiferromagnetic interlayer exchange. *Physical Review B*, 39:4828–4830, Mar. 1989.

[3] J.C. Slonczewski. Current-driven excitation of magnetic multilayers. *Journal of Magnetism and Magnetic Materials*, 159(12):L1 – L7, 1996.

[4] J. S. Moodera, Lisa R. Kinder, Terrilyn M. Wong, and R. Meservey. Large magnetoresistance at room temperature in ferromagnetic thin film tunnel junctions. *Phys. Rev. Lett.*, 74:3273–3276, Apr 1995.

[5] P. P. Freitas and L. Berger. Observation of s-d exchange force between domain walls and electric current in very thin permalloy films. *Journal of Applied Physics*, 57(4):1266–1269, 1985.

[6] Tao Yang, Takashi Kimura, and Yoshichika Otani. Giant spin-accumulation signal and pure spin-current-induced reversible magnetization switching. *Nature Physics*, 4:851–854, 2008.

[7] R. Fiederling, M. Keim, G. Reuscher, W. Ossau, G. Schmidt, A. Waag, and L. W. Molenkamp. Injection and detection of a spin-polarized current in a light-emitting diode. *Nature*, 402:787–790, 1999.

[8] Y. Ohno, D. K. Young, B. Beschoten, F. Matsukura, H. Ohno, and D. D. Awschalom. Electrical spin injection in a ferromagnetic semiconductor heterostructure. *Nature*, 402:790–792, 1999.

[9] Luqiao Liu, Chi-Feng Pai, Y. Li, H. W. Tseng, D. C. Ralph, and R. A. Buhrman. Spin-torque switching with the giant spin hall effect of tantalum. *Science*, 336(6081):555–558, 2012.

[10] Supriyo Datta and Biswajit Das. Electronic analog of the electro-optic modulator. *Applied Physics Letters*, 56:665, 1990.

[11] Stuart S. P. Parkin, Masamitsu Hayashi, and Luc Thomas. Magnetic domain-wall racetrack memory. *Science*, 320(5873):190–194, 2008.

[12] J. Z. Sun, M. C. Gaidis, E. J. OSullivan, E. A. Joseph, G. Hu, D. W. Abraham, J. J. Nowak, P. L. Trouilloud, Yu Lu, S. L. Brown, D. C. Worledge, and W. J. Gallagher. A three-terminal spin-torque-driven magnetic switch. *Applied Physics Letters*, 95:083506, 2009.

[13] J. A. Katine, F. J. Albert, R. A. Buhrman, E. B. Myers, and D. C. Ralph. Current-driven magnetization reversal and spin-wave excitations in Co/Cu/Co pillars. *Physical Review Letters*, 84:3149–3152, Apr. 2000.

[14] D.C. Ralph and M.D. Stiles. Spin transfer torques. *Journal of Magnetism and Magnetic Materials*, 320(7):1190 – 1216, 2008.

[15] Chen Wang, Cui Yong-Tao, Jordan A. Katine, Robert A. Buhrman, and Daniel C. Ralph. Time-resolved measurement of spin-transfer-driven ferromagnetic resonance and spin torque in magnetic tunnel junctions. *Nature Physics*, 7:496–501, June 2011.

[16] M. Beleggia, M. De Graef, Y. T. Millev, D. A. Goode, and G. Rowlands. Demagnetization factors for elliptic cylinders. *Journal of Physics D: Applied Physics*, 38(18):3333, 2005.

[17] S. Ikeda, J. Hayakawa, Young Min Lee, F. Matsukura, Yuzo Ohno, T. Hanyu, and H. Ohno. Magnetic tunnel junctions for spintronic memories and beyond. *IEEE Transactions on Electron Devices*, 54(5):991–1002, 2007.

[18] J. Z. Sun. Spin-current interaction with a monodomain magnetic body: A model study. *Phys. Rev. B*, 62:570–578, Jul 2000.

[19] Jonathan Z Sun. Personal Conversation, 2009.

[20] Tom Ambrose. Spin transport effects in heusler alloys. Presentation given at Cornell University, Sep. 2009.

[21] Robert O'Handley. *Modern Magnetic Materials: Principles and Applications*. John Wiley and Sons, New York, 2000.

[22] D. Houssameddine, U. Ebels, B. Delaet, B. Rodmacq, I. Firastrau, F. Ponthenier, M. Brunet, C. Thirion, J. P. Michel, L. Prejbeanu-Buda, M. C. Cyrille, O. Redon, and B. Dieny. Spin-torque oscillator using a perpendicular polarizer and a planar free layer. *Nature Materials*, 6:447–453, June 2007.

[23] Luqiao Liu, Takahiro Moriyama, D. C. Ralph, and R. A. Buhrman. Reduction of the spin-torque critical current by partially canceling the free layer demagnetization field. *Applied Physics Letters*, 94(12):122508, 2009.

[24] S. Mangin, D. Ravelosona, J. A. Katine, M. J. Carey, B. D. Terris, and Eric E. Fullerton. Current-induced magnetization reversal in nanopillars with perpendicular anisotropy. *Nature Materials*, 5:210–215, Mar. 2006.

[25] S. Mangin, Y. Henry, D. Ravelosona, J. A. Katine, and Eric E. Fullerton. Reducing the critical current for spin-transfer switching of perpendicularly magnetized nanomagnets. *Applied Physics Letters*, 94(1):012502, 2009.

[26] Masahiko Nakayama, Tadashi Kai, Naoharu Shimomura, Minoru Amano, Eiji Kitagawa, Toshihiko Nagase, Masatoshi Yoshikawa, Tatsuya Kishi, Sumio Ikegawa, and Hiroaki Yoda. Spin transfer switching in TbCoFe/CoFeB/MgO/CoFeB/TbCoFe magnetic tunnel junctions with perpendicular magnetic anisotropy. *Journal of Applied Physics*, 103(7):07A710, 2008.

[27] Stuart S. P. Parkin, Christian Kaiser, Alex Panchula, Philip M. Rice, Brian Hughes, Mahesh Samant, and See-Hun Yang. Giant tunnelling magnetoresistance at room temperature with MgO (100) tunnel barriers. *Nature Materials*, 3:862–867, Dec. 2004.

[28] Shinji Yuasa, Taro Nagahama, Akio Fukushima, Yoshishige Suzuki, and Koji Ando. Giant room-temperature magnetoresistance in single-crystal Fe/MgO/Fe magnetic tunnel junctions. *Nature Materials*, 3:868–871, Dec. 2004.

[29] S. Ikeda, J. Hayakawa, Y. Ashizawa, Y. M. Lee, K. Miura, H. Hasegawa, M. Tsunoda, F. Matsukura, and H. Ohno. Tunnel magnetoresistance of 604% at 300 K by suppression of Ta diffusion in CoFeB/MgO/CoFeB pseudo-spin-valves annealed at high temperature. *Applied Physics Letters*, 93(8):082508, 2008.

[30] Néel, Louis. Anisotropie magnétique superficielle et surstructures d'orientation. *Journal Physical Radium*, 15(4):225–239, 1954.

[31] J. G. Gay and Roy Richter. Spin anisotropy of ferromagnetic films. *Physical Review Letters*, 56:2728–2731, June 1986.

[32] G. H. O. Daalderop, P. J. Kelly, and F. J. A. den Broeder. Prediction

and confirmation of perpendicular magnetic anisotropy in Co/Ni multilayers. *Physical Review Letters*, 68:682–685, Feb. 1992.

[33] P. J. H. Bloemen, W. J. M. de Jonge, and F. J. A. den Broeder. Magnetic anisotropies in Co/Ni(111) multilayers. *Journal of Applied Physics*, 72(10):4840–4844, 1992.

[34] Y.B. Zhang, P. He, John A. Woollam, J.X. Shen, Roger D. Kirby, and David J. Sellmyer. Magnetic and magneto-optic properties of sputtered Co/Ni multilayers. *Journal of Applied Physics*, 75(10):6495–6497, 1994.

[35] W. Chen, J.-M.L. Beaujour, G. De Loubens, A.D. Kent, and J.Z. Sun. Spin-torque driven ferromagnetic resonance of Co/Ni synthetic layers in spin valves. *Applied Physics Letters*, 92:012507, 2008.

[36] S. Girod, M. Gottwald, S. Andrieu, S. Mangin, J. McCord, Eric E. Fullerton, J.-M.L. Beaujour, B.J. Krishnatreya, and A.D. Kent. Strong perpendicular magnetic anisotropy in Ni/Co (111) single crystal superlattices. *Applied Physics Letters*, 94(26):262504–262504, 2009.

[37] P. F. Carcia, A. D. Meinhaldt, and A. Suna. Perpendicular magnetic anisotropy in Pd/Co thin film layered structures. *Applied Physics Letters*, 47(2):178–180, 1985.

[38] P. F. Carcia. Perpendicular magnetic anisotropy in Pd/Co and Pt/Co thin-film layered structures. *Journal of Applied Physics*, 63(10):5066–5073, 1988.

[39] F. J. A. den Broeder, D. Kuiper, A. P. van de Mosselaer, and W. Hoving. Perpendicular magnetic anisotropy of Co-Au multilayers induced by interface sharpening. *Physical Review Letters*, 60:2769–2772, Jun 1988.

[40] F. J. A. den Broeder, W. Hoving, and P. J. H. Bloemen. Magnetic anisotropy of multilayers. *Journal of Magnetism and Magnetic Materials*, 93(0):562 – 570, 1991.

[41] S. Mizukami, E. P. Sajitha, D. Watanabe, F. Wu, T. Miyazaki, H. Naganuma, M. Oogane, and Y. Ando. Gilbert damping in perpendicularly magnetized Pt/Co/Pt films investigated by all-optical pump-probe technique. *Applied Physics Letters*, 96(15):152502, 2010.

[42] J.-M.L. Beaujour, W. Chen, K. Krycka, C.-C. Kao, J. Z. Sun, and A. D. Kent. Ferromagnetic resonance study of sputtered Co—Ni multilayers. *The*

European Physical Journal B - Condensed Matter and Complex Systems, 59:475–483, 2007.

[43] David E. Laughlin, Kumar Srinivasan, Mihaela Tanase, and Lisha Wang. Crystallographic aspects of L10 magnetic materials. *Scripta Materialia*, 53(4):383 – 388, 2005.

[44] Wupeng Cai, Ji Shi, Yoshio Nakamura, Wei Liu, and Ronghai Yu. Roles of $L1_0$ ordering in controlling the magnetic anisotropy and coercivity of (111)-oriented CoPt ultrathin continuous layers in CoPt/AlN multilayer films. *Journal of Applied Physics*, 110(7):073907, 2011.

[45] Osamu Yabuhara, Mitsuru Ohtake, Kouske Tobari, Tsutomu Nishiyama, Fumiyoshi Kirino, and Masaaki Futamoto. Structural and magnetic properties of FePd and CoPd alloy epitaxial thin films grown on MgO single-crystal substrates with different orientations. *Thin Solid Films*, 519(23):8359 – 8362, 2011. First International Conference of the Asian Union of Magnetics Societies (ICAUMS 2010).

[46] A. Kashyap, R. Skomski, A. K. Solanki, Y. F. Xu, and D. J. Sellmyer. Magnetism of $L1_0$ compounds with the composition MT (M = Rh, Pd, Pt, Ir and T = Mn, Fe, Co, Ni). *Journal of Applied Physics*, 95(11):7480–7482, 2004.

[47] M. Hagiuda, S. Mitani, T. Seki, K. Yakushiji, T. Shima, and K. Takanashi. Epitaxial growth of $L1_0$-FePt/MgO/$L1_0$-FePt trilayer structures. *Journal of Magnetism and Magnetic Materials*, 310(2, Part 3):1905 – 1907, 2007. Proceedings of the 17th International Conference on Magnetism.

[48] Angie Sarkis and Earl Callen. Magnetic anisotropy of rare-earth transition-metal compounds. *Physical Review B*, 26:3870–3877, Oct. 1982.

[49] S. G. Reidy, L. Cheng, and W. E. Bailey. Dopants for independent control of precessional frequency and damping in $Ni_{81}Fe_{19}$ (50 nm) thin films. *Applied Physics Letters*, 82(8):1254–1256, 2003.

[50] Charles Kittel. On the theory of ferromagnetic resonance absorption. *Physical Review*, 73:155–161, Jan. 1948.

[51] J. C. Sankey, P. M. Braganca, A. G. F. Garcia, I. N. Krivorotov, R. A. Buhrman, and D. C. Ralph. Spin-transfer-driven ferromagnetic resonance of individual nanomagnets. *Physical Review Letters*, 96:227601, June 2006.

[52] Sangita S. Kalarickal, Pavol Krivosik, Mingzhong Wu, Carl E. Patton, Michael L. Schneider, Pavel Kabos, T. J. Silva, and John P. Nibarger. Ferromagnetic resonance linewidth in metallic thin films: Comparison of measurement methods. *Journal of Applied Physics*, 99(9):093909, 2006.

[53] Douglas L. Mills and Sergio M. Rezende. Spin damping in ultrathin magnetic films. In Burkard Hillebrands and Kamel Ounadjela, editors, *Spin Dynamics in Confined Magnetic Structures II*, volume 87 of *Topics in Applied Physics*, pages 27–59. Springer Berlin Heidelberg, 2003.

[54] Charles Kittel. *Introduction to Solid State Physics*. John Wiley and Sons Inc., New York, 7th edition, 1996.

[55] B. Heinrich, J. F. Cochran, and R. Hasegawa. FMR linebroadening in metals due to two-magnon scattering. *Journal of Applied Physics*, 57(8):3690–3692, 1985.

[56] Takahiro Moriyama, Theodore J. Gudmundsen, Pinshane Y. Huang, Luqiao Liu, David A. Muller, Daniel C. Ralph, and Robert A. Buhrman. Tunnel magnetoresistance and spin torque switching in MgO-based magnetic tunnel junctions with a Co/Ni multilayer electrode. *Applied Physics Letters*, 97(7):072513, 2010.

[57] R.N. Simons. *Coplanar Waveguide Circuits, Components, and Systems*. Wiley Series in Microwave and Optical Engineering. John Wiley & Sons, 2004.

[58] John C. Read. *Magnesium Boron Oxide Tunnel Barriers*. PhD thesis, Cornell University, 2009.

[59] W. G. Wang, C. Ni, A. Rumaiz, Y. Wang, X. Fan, T. Moriyama, R. Cao, Q. Y. Wen, H. W. Zhang, and John Q. Xiao. Real-time evolution of tunneling magnetoresistance during annealing in CoFeB/MgO/CoFeB magnetic tunnel junctions. *Applied Physics Letters*, 92(15):152501, 2008.

[60] J.Z. Sun and D.C. Ralph. Magnetoresistance and spin-transfer torque in magnetic tunnel junctions. *Journal of Magnetism and Magnetic Materials*, 320(7):1227 – 1237, 2008.

[61] J. Mathon and A. Umerski. Theory of tunneling magnetoresistance of an epitaxial Fe/MgO/Fe(001) junction. *Physical Review B*, 63:220403, May 2001.

[62] W. H. Butler, X.-G. Zhang, T. C. Schulthess, and J. M. MacLaren. Spin-dependent tunneling conductance of Fe|MgO|Fe sandwiches. *Physical Review B*, 63:054416, Jan. 2001.

[63] Christian Heiliger, Martin Gradhand, Peter Zahn, and Ingrid Mertig. Tunneling magnetoresistance on the subnanometer scale. *Physical Review Letters*, 99(6):066804, 2007.

[64] D. A. Muller, L. Fitting Kourkoutis, M. Murfitt, J. H. Song, H. Y. Hwang, J. Silcox, N. Dellby, and O. L. Krivanek. Atomic-scale chemical imaging of composition and bonding by aberration-corrected microscopy. *Science*, 319(5866):1073–1076, 2008.

[65] C. H. Lee, Hui He, F. Lamelas, W. Vavra, C. Uher, and Roy Clarke. Epitaxial Co-Au superlattices. *Physical Review Letters*, 62:653–656, Feb. 1989.

[66] S. Ikeda, K. Miura, H. Yamamoto, K. Mizunuma, H. D. Gan, M. Endo, S. Kanai, J. Hayakawa, F. Matsukura, and H. Ohno. A perpendicular-anisotropy CoFeB-MgO magnetic tunnel junction. *Nature Materials*, 9:721–724, Sep. 2010.

[67] S. W. Sun and R. C. O'Handley. Surface magnetoelastic coupling. *Physical Review Letters*, 66:2798–2801, May 1991.

[68] Nathan C. Emley. *Magnetic Multilayer Nanopillars for the Study of Current-Induced Reversal of a Thin Magnetic Layer*. PhD thesis, Cornell University, 2005.

[69] Frank Joseph Albert. *The Fabrication and Measurment of Current Perpendicular to the Plane Magnetic Nanostructures for the Study of the Spin Transfer Effect*. PhD thesis, Cornell University, 2003.

[70] E. B. Myers, F. J. Albert, J. C. Sankey, E. Bonet, R. A. Buhrman, and D. C. Ralph. Thermally activated magnetic reversal induced by a spin-polarized current. *Physical Review Letters*, 89:196801, Oct 2002.

[71] Z. Li and S. Zhang. Thermally assisted magnetization reversal in the presence of a spin-transfer torque. *Physical Review B*, 69:134416, Apr 2004.

[72] D. M. Apalkov and P. B. Visscher. Spin-torque switching: Fokker-Planck rate calculation. *Physical Review B*, 72:180405, Nov 2005.

[73] R. H. Koch, J. A. Katine, and J. Z. Sun. Time-resolved reversal of spin-transfer switching in a nanomagnet. *Physical Review Letters*, 92:088302, Feb. 2004.

[74] M. P. Sharrock. Time dependence of switching fields in magnetic recording media. *Journal of Applied Physics*, 76(10):6413–6418, 1994.

[75] D. G. Porter M. J. Donahue. OOMMF users guide, version 1.0,. Technical Report NISTIR 6376, National Institute of Standards and Technology, Gaithersburg, Maryland, February 2000.

[76] Mark D. Stiles and J Miltat. Spin transfer torque and dynamics. In Burkard Hillebrands and Andre Thiaville, editors, *Spin Dynamics in Confined Magnetic Structures III*, volume 101 of *Topics in Applied Physics*, pages 225–308. Springer Berlin Heidelberg, November 2006.

[77] D. Ravelosona, S. Mangin, Y. Lemaho, J. A. Katine, B. D. Terris, and Eric E. Fullerton. Domain wall creation in nanostructures driven by a spin-polarized current. *Physical Review Letters*, 96:186604, May 2006.

[78] L. San Emeterio Alvarez, K.-Y. Wang, S. Lepadatu, S. Landi, S. J. Bending, and C. H. Marrows. Spin-transfer-torque-assisted domain-wall creep in a Co/Pt multilayer wire. *Physical Review Letters*, 104:137205, Apr. 2010.

[79] Alexandre Blais, Ren-Shou Huang, Andreas Wallraff, S. M. Girvin, and R. J. Schoelkopf. Cavity quantum electrodynamics for superconducting electrical circuits: An architecture for quantum computation. *Physical Review A*, 69:062320, 2004.

[80] S. V. Vonsovskii. *Ferromagnetic resonance*. Pergamon Press, Oxford, New York, 1966.

[81] M. Goppl, A. Fragner, M. Baur, R. Bianchetti, S. Filipp, J. M. Fink, P. J. Leek, G. Puebla, L. Steffen, and A. Wallraff. Coplanar waveguide resonators for circuit quantum electrodynamics. *Journal of Applied Physics*, 104(11):113904, 2008.

[82] A. Megrant, C. Neill, R. Barends, B. Chiaro, Yu Chen, L. Feigl, J. Kelly, Erik Lucero, Matteo Mariantoni, P. J. J. O'Malley, D. Sank, A. Vainsencher, J. Wenner, T. C. White, Y. Yin, J. Zhao, C. J. Palmstrom, John M. Martinis, and A. N. Cleland. Planar superconducting resonators with internal quality factors above one million. *Applied Physics Letters*, 100(11):113510, 2012.

[83] Aaron D. O'Connell, M. Ansmann, R. C. Bialczak, M. Hofheinz, N. Katz, Erik Lucero, C. McKenney, M. Neeley, H. Wang, E. M. Weig, A. N. Cleland, and J. M. Martinis. Microwave dielectric loss at single photon energies and millikelvin temperatures. *Applied Physics Letters*, 92(11):112903, 2008.

[84] C. A. Regal, J. D. Teufel, and K. W. Lehnert. Measuring nanomechanical motion with a microwave cavity interferometer. *Nature Physics*, 4:555–560, 2008.

[85] M. J. Woolley, A. C. Doherty, G. J. Milburn, and K. C. Schwab. Nanomechanical squeezing with detection via a microwave cavity. *Physical Review A*, 78:062303, 2008.

[86] A. A. Houck, D. I. Schuster, J. M. Gambetta, J. A. Schreier, B. R. Johnson, J. M. Chow, L. Frunzio, J. Majer, M. H. Devoret, S. M. Girvin, and R. J. Schoelkopf. Generating single microwave photons in a circuit. *Nature*, 449:328–331, 2007.

[87] J. Majer, J. M. Chow, J. M. Gambetta, Jens Koch, B. R. Johnson, J. A. Schreier, L. Frunzio, D. I. Schuster, A. A. Houck, A. Wallraff, A. Blais, M. H. Devoret, S. M. Girvin, and R. J. Schoelkopf. Coupling superconducting qubits via a cavity bus. *Nature*, 449:443–447, 2007.

[88] N. Bergeal, F. Schackert, M. Metcalfe, R. Vijay, V. E. Manucharyan, L. Frunzio, D. E. Prober, R. J. Schoelkopf, S. M. Girvin, and M. H. Devoret. Phase-preserving amplification near the quantum limit with a Josephson ring modulator. *Nature*, 465:64 – 68, 2010.

[89] S. I. Kiselev, J. C. Sankey, I. N. Krivorotov, N. C. Emley, R. J. Schoelkopf, R. A. Buhrman, and D. C. Ralph. Microwave oscillations of a nanomagnet driven by a spin-polarized current. *Nature*, 425:380–383, 2003.

[90] D. I. Schuster, A. P. Sears, E. Ginossar, L. DiCarlo, L. Frunzio, J. J. L. Morton, H. Wu, G. A. D. Briggs, B. B. Buckley, D. D. Awschalom, and R. J. Schoelkopf. High-cooperativity coupling of electron-spin ensembles to superconducting cavities. *Physical Review Letters*, 105:140501, Sep. 2010.

[91] Y. Kubo, C. Grezes, A. Dewes, T. Umeda, J. Isoya, H. Sumiya, N. Morishita, H. Abe, S. Onoda, T. Ohshima, V. Jacques, A. Dréau, J.-F. Roch, I. Diniz, A. Auffeves, D. Vion, D. Esteve, and P. Bertet. Hybrid quantum circuit with a superconducting qubit coupled to a spin ensemble. *Physical Review Letters*, 107:220501, Nov. 2011.

[92] O. O. Soykal and M. E. Flatté. Strong field interactions between a nanomagnet and a photonic cavity. *Physical Review Letters*, 104:077202, Feb 2010.

[93] R. H. Dicke. Coherence in spontaneous radiation processes. *Physical Review*, 93(1):99, 1954.

[94] Hans Huebl, Christoph Zollitsch, Johannes Lotze, Fredrik Hocke, Moritz Greifenstein, Achim Marx, Rudolf Gross, and Sebastian T. B. Goennenwein. High cooperativity in coupled microwave resonator ferrimagnetic insulator hybrids. *arXiv:1207.6039 [quant-ph]*, 2012.

[95] David Issac Schuster. *Circuit Quantum Electrodynamics*. PhD thesis, Yale University, 2007.

[96] John M. Martinis, K. B. Cooper, R. McDermott, Matthias Steffen, Markus Ansmann, K. D. Osborn, K. Cicak, Seongshik Oh, D. P. Pappas, R. W. Simmonds, and Clare C. Yu. Decoherence in josephson qubits from dielectric loss. *Physical Review Letters*, 95:210503, Nov. 2005.

[97] Alexander Shnirman, Gerd Schön, Ivar Martin, and Yuriy Makhlin. Low- and high-frequency noise from coherent two-level systems. *Physical Review Letters*, 94:127002, Apr. 2005.

[98] Jared Hertzberg. *Back-action Evading Measurements of Nanomechanical Motion Approaching Quantum Limits*. PhD thesis, Univ. of Maryland, College Park, 2009.

[99] A. A. Houck, J. A. Schreier, B. R. Johnson, J. M. Chow, Jens Koch, J. M. Gambetta, D. I. Schuster, L. Frunzio, M. H. Devoret, S. M. Girvin, and R. J. Schoelkopf. Controlling the spontaneous emission of a superconducting transmon qubit. *Physical Review Letters*, 101:080502, Aug. 2008.

[100] Andreas Wallraff, D.I. Schuster, Alexander Blais, L. Frunzio, R.-S. Huang, J. Majer, S. Kumar, S.M. Girvin, and R.J. Schoelkopf. Strong coupling of a single photon to a superconducting qubit using circuit quantum electrodynamics. *Nature*, 431(7005):162–167, 2004.

[101] T. T. Foxe, B.D. Hunt, C. Rogers, A.W. Kleinsasser, and R.A. Buhrman. Reactive ion etching of niobium. *Journal of Vacuum Science and Technology*, 19(4):1394–1397, 1981.

[102] S. K. Tolpygo, D. Amparo, R. T. Hunt, J. A. Vivalda, and D. T. Yohannes. Diffusion stop-layers for superconducting integrated circuits and qubits with Nb-based josephson junctions. *Applied Superconductivity, IEEE Transactions on*, 21(3):119–125, 6 2011.

[103] A. H. MacDonald, P. Schiffer, and N. Samarth. Ferromagnetic semiconductors: moving beyond (Ga,Mn)As. *Nature Materials*, 4:195–202, 2005.

[104] M. J. Calderón and S. Das Sarma. Theory of carrier mediated ferromagnetism in dilute magnetic oxides. *Annals of Physics*, 322:2618–2634, 2007.

[105] S Gardelis, CG Smith, CHW Barnes, EH Linfield, and DA Ritchie. Spin-valve effects in a semiconductor field-effect transistor: A spintronic device. *Physical Review B*, 60(11):7764, 1999.

[106] P. R. Hammar, B. R. Bennett, M. J. Yang, and Mark Johnson. Observation of spin injection at a ferromagnet-semiconductor interface. *Phys. Rev. Lett.*, 83:203–206, Jul 1999.

[107] X. Jiang, R. Wang, R. M. Shelby, R. M. Macfarlane, S. R. Bank, J. S. Harris, and S. S. Parkin. Highly spin-polarized room-temperature tunnel injector for semiconductor spintronics using MgO(100). *Physical Review Letters*, 94:056601, 2005.

[108] O. M. J. van 't Erve, G. Kioseoglou, A. T. Hanbicki, C. H. Li, B. T. Jonker, R. Mallory, M. Yasar, and A. Petrou. Comparison of Fe/Schottky and Fe/Al_2O_3 tunnel barrier contacts for electrical spin injection into GaAs. *Applied Physics Letters*, 84:4334–4336, 2004.

[109] Asawin Sinsarp, Takashi Manago, Fumiyoshi Takano, and Hiro Akinaga. Electrical spin injection from out-of-plane magnetized FePt/MgO tunneling junction into GaAs at room temperature. *Japanese Journal of Applied Physics*, 46:4, 2007.

[110] C. T. Boone, J. A. Katine, M. Carey, J. R. Childress, X. Cheng, and I. N. Krivorotov. Rapid domain wall motion in permalloy nanowires excited by a spin-polarized current applied perpendicular to the nanowire. *Physical Review Letters*, 104:097203, 2010.

[111] Stefania Pizzini, Vojte Uhlr, Jan Vogel, Nicolas Rougemaille, Sana Laribi, Vincent Cros, Erika Jiménez, Julio Camarero, Carsten Tieg, Edgar Bonet, Marlio Bonfim, Richard Mattana, Cyrile Deranlot, Frdric Petroff, Christian

Ulysse, Giancarlo Faini, and Albert Fert. High domain wall velocity at zero magnetic field induced by low current densities in spin valve nanostripes. *Applied Physics Express*, 2:023003, 2009.

[112] Masamitsu Hayashi, Luc Thomas, Charles Rettner, Rai Moriya, Yaroslaw B. Bazaliy, and Stuart S. Parkin. Current driven domain wall velocities exceeding the spin angular momentum transfer rate in permalloy nanowires. *Physical Review Letters*, 98:037204, 2007.

[113] M. Klaui, P. O. Jubert, R. Allenspach, A. Bischof, J. A. Bland, G. Faini, U. R udiger, C. A. Vaz, L. Vila, and C. Vouille. Direct observation of domain-wall configurations transformed by spin currents. *Physical Review Letters*, 95:026601, 2005.

[114] John Kerr. On rotation of the plane of the polarization by reflection from the pole of a magnet. *Philosophical Magazine*, 3(321), 1877.

[115] Sputtering yields reference article. Technical Report 8, Angstrom Sciences, Inc., May 2009.

[116] Eiji Saitoh, Hideki Miyajima, Takehiro Yamaoka, and Gen Tatara. Current-induced resonance and mass determination of a single magnetic domain wall. *Nature*, 432(7014):203–206, Nov 2004.

[117] Luc Thomas, Masamitsu Hayashi, Xin Jiang, Rai Moriya, Charles Rettner, and Stuart S. P. Parkin. Oscillatory dependence of current-driven magnetic domain wall motion on current pulse length. *Nature*, 443(7108):197–200, Sep 2006.

[118] A. Yamaguchi, T. Ono, S. Nasu, K. Miyake, K. Mibu, and T. Shinjo. Real-space observation of current-driven domain wall motion in submicron magnetic wires. *Phys. Rev. Lett.*, 92:077205, Feb 2004.

[119] J. Grollier, P. Boulenc, V. Cros, A. Hamzic, A. Vaures, A. Fert, and G. Faini. Switching a spin valve back and forth by current-induced domain wall motion. *Applied Physics Letters*, 83(3):509–511, 2003.

[120] D. Ravelosona, D. Lacour, J. A. Katine, B. D. Terris, and C. Chappert. Nanometer scale observation of high efficiency thermally assisted current-driven domain wall depinning. *Phys. Rev. Lett.*, 95:117203, Sep 2005.